

# Estimating particle size and coercivity distributions of pigmentary hematite in red chert with thermal fluctuation tomography

Pengxiang Hu<sup>1</sup>, Xiang Zhao<sup>1</sup>, David Heslop<sup>2</sup>, Hirokuni Oda<sup>3</sup>, and Andrew P. Roberts<sup>1</sup>

<sup>1</sup>Australian National University

<sup>2</sup>Research School of Earth Sciences

<sup>3</sup>Geological Survey of Japan, AIST

December 15, 2022

## Abstract

Pigmentary hematite carries important signals in paleomagnetic and paleoenvironmental studies. However, weak magnetism and the assumption that it has high magnetic coercivity prevents routine identification of the size distribution of pigmentary hematite, especially for fine particle sizes. We present a strategy for estimating joint hematite particle volume and microcoercivity ( $f(V, H_k0)$ ) distributions from low-temperature demagnetization curves and thermal fluctuation tomography (TFT) of pigmentary hematite in bulk samples of Triassic-Jurassic Inuyama red chert, Japan. The coercivity of the pigmentary hematite increases exponentially with decreasing temperature, following a modified Kneller's law, where microcoercivity has a wide but approximately symmetric distribution in logarithmic space from  $\sim 1$  tesla to tens of tesla. All of the red chert samples contain stable single domain (SSD) hematite with 35 - 160 nm diameter; a significant superparamagnetic (SP) hematite population with sizes down to several nanometers also occurs in Jurassic samples. The SP/SSD threshold size is estimated to be 8 - 18 nm in these samples. The fine particle size of the pigmentary hematite is evident in its low median unblocking temperature (194 °C to 529 °C) and, thus, this hematite may contribute to all four paleomagnetic components identified in published thermal magnetization studies of the Inuyama red chert. In this work, uniaxial anisotropy and magnetization switching via coherent rotation are assumed. Uniaxial anisotropy is often dominant in fine-grained hematite, although the dominant anisotropy type should be evaluated before using TFT. This approach is applicable to studies that require knowledge of coercivity and size distributions of hematite pigments.

1 **Estimating particle size and coercivity distributions of pigmentary hematite in red**  
2 **chert with thermal fluctuation tomography**

3 **Pengxiang Hu<sup>1,2</sup>, Xiang Zhao<sup>1,2</sup>, David Heslop<sup>1,2</sup>, Hirokuni Oda<sup>2</sup>, Andrew P. Roberts<sup>1,2</sup>**  
4

5 <sup>1</sup> *Research School of Earth Sciences, Australian National University, Canberra, ACT 2601,*  
6 *Australia*

7 <sup>2</sup> *Research Institute of Geology and Geoinformation, Geological Survey of Japan, National*  
8 *Institute of Advanced Industrial Science and Technology (AIST), AIST Tsukuba Central 7, 1-1-*  
9 *1 Higashi, Tsukuba, Ibaraki, 305-8567, Japan*

10  
11 *Corresponding author: Pengxiang Hu ([pengxiang.hu@anu.edu.au](mailto:pengxiang.hu@anu.edu.au))*

12  
13 **Key Points:**

- 14 • Thermal fluctuation tomography is applied to red cherts to estimate grain size and  
15 microcoercivity distributions of pigmentary hematite
- 16 • Fine hematite particles (35 - 160 nm) occur in all samples including superparamagnetic  
17 hematite down to a few nanometers
- 18 • Temperature-dependent coercivity variations in pigmentary hematite follow Kneller's law  
19

20 **Plain language Summary**

21 Pigmentary hematite widely presents in rocks and sediment and is crucial for paleomagnetic and  
22 paleoenvironmental studies because they can record ancient earth magnetic field and past climate  
23 signals. As the most important properties in paleomagnetic and paleoenvironmental applications,  
24 the coercivity and grain size distribution of natural pigmentary hematite is poorly constrained  
25 due to the weak magnetism of hematite and the small size. In this study, we provide a strategy  
26 using low-temperature demagnetization curves for estimating joint particle volume and  
27 microcoercivity distribution of pigmentary hematite in Inuyama red chert samples. The hematite  
28 coercivity increases exponentially with decreasing temperature. Hematite microcoercivity  
29 without thermal fluctuation has a wide but approximately symmetric distribution in logarithmic

30 space from ~1 tesla to tens of tesla. The grain size of hematite varies from several nanometers to  
31 about 160 nm. The fine particle size of these hematite results in low unblocking temperature,  
32 which makes them suitable to record remagnetization in geological time.

33

## 34 **Abstract**

35 Pigmentary hematite carries important signals in paleomagnetic and paleoenvironmental studies.  
36 However, weak magnetism and the assumption that it has high magnetic coercivity prevents  
37 routine identification of the size distribution of pigmentary hematite, especially for fine particle  
38 sizes. We present a strategy for estimating joint hematite particle volume and microcoercivity ( $f$   
39 ( $V$ ,  $H_{k0}$ )) distributions from low-temperature demagnetization curves and thermal fluctuation  
40 tomography (TFT) of pigmentary hematite in bulk samples of Triassic-Jurassic Inuyama red chert,  
41 Japan. The coercivity of the pigmentary hematite increases exponentially with decreasing  
42 temperature, following a modified Kneller's law, where microcoercivity has a wide but  
43 approximately symmetric distribution in logarithmic space from ~1 tesla to tens of tesla. All of the  
44 red chert samples contain stable single domain (SSD) hematite with 35 - 160 nm diameter; a  
45 significant superparamagnetic (SP) hematite population with sizes down to several nanometers  
46 also occurs in Jurassic samples. The SP/SSD threshold size is estimated to be 8 - 18 nm in these  
47 samples. The fine particle size of the pigmentary hematite is evident in its low median unblocking  
48 temperature (194 °C to 529 °C) and, thus, this hematite may contribute to all four paleomagnetic  
49 components identified in published thermal magnetization studies of the Inuyama red chert. In this  
50 work, uniaxial anisotropy and magnetization switching via coherent rotation are assumed. Uniaxial  
51 anisotropy is often dominant in fine-grained hematite, although the dominant anisotropy type  
52 should be evaluated before using TFT. This approach is applicable to studies that require  
53 knowledge of coercivity and size distributions of hematite pigments.

54

## 55 **1. Introduction**

56 Hematite is abundant in sedimentary rocks, especially red beds. It occurs commonly as a fine-  
57 grained chemically precipitated pigment and as coarser detrital or specular hematite (Cornell and  
58 Schwertmann, 2003; Lepre and Olsen, 2021; Jiang et al., 2022; Swanson-Hysell et al., 2019; Tauxe

59 et al., 1980). Poorly crystalline pigmentary hematite can be the dominant iron oxide in many red  
60 soils and sediments and is responsible for their characteristic red color. Both specular and  
61 pigmentary hematite can carry magnetic remanence. Specular hematite carries a detrital remanent  
62 magnetization (DRM), which is often assumed to be a primary or near-primary magnetization.  
63 Widely observed red bed remagnetizations tend to be associated with late diagenetic pigmentary  
64 hematite formation. Debate about whether red beds record a primary DRM or a secondary  
65 chemical remanent magnetization (CRM) led to the “red bed controversy” (Beck et al., 2003;  
66 Butler, 1992; Van Der Voo & Torsvik, 2012). Identification of CRM acquisition in pigmentary  
67 hematite can enable more accurate paleomagnetic interpretations in regional tectonic studies  
68 (Abrajevitch et al., 2018; Jiang et al., 2017; Swanson-Hysell et al., 2019). As the most abundant  
69 surficial iron oxide on Earth resulting from near-surface processes, hematite is also an excellent  
70 recorder of paleoenvironmental signals. Its formation via authigenic chemical processes means  
71 that pigmentary hematite is used as an indicator of hydration conditions, acidity of aqueous  
72 environments, and monsoon evolution (e.g., Larrasoña et al., 2003; Abrajevitch et al., 2013; Lepre  
73 and Olsen, 2021). Despite the usefulness of pigmentary hematite as a paleoclimatic indicator or as  
74 a carrier of paleomagnetic records, it is often described vaguely as a “fine hematite population”,  
75 with poorly constrained coercivity and grain size distributions.

76  
77 Characterizing the grain size and coercivity of pigmentary hematite is challenging because it is  
78 necessary to overcome the combined difficulty of detecting weakly magnetic hematite when it co-  
79 occurs with other magnetic minerals and characterizing poorly crystalline nanoparticles. Magnetite  
80 has a spontaneous magnetization that is more than 200 times stronger than hematite, so even small  
81 amounts of magnetite can overwhelm the magnetic contribution of hematite (Dekkers, 1990; Frank  
82 and Nowaczyk, 2008; Roberts et al., 2020). In practice, hematite detection in natural samples often  
83 relies on its high coercivity and distinctive color (Roberts et al., 2020; Jiang et al., 2022 and  
84 references therein). However, the small size and often poorly crystalline nature of hematite  
85 nanoparticles means that hematite concentrations can be difficult to determine with many  
86 spectroscopic approaches. Such particles will also be responsible for a substantial low-coercivity  
87 distribution that is not usually attributed to hematite in mineral magnetic studies, especially when  
88 using magnetic parameters with cut-off fields of 300 mT (Roberts et al., 2020). Isothermal  
89 remanent magnetization (IRM) component analysis appears to be the most suitable magnetic

90 method for detecting hematite because it enables estimation of continuous, non-truncated  
91 coercivity distributions (Hu et al., 2021; Roberts et al., 2020). However, superparamagnetic (SP)  
92 pigmentary hematite, which is abundant in natural environments (Collinson, 1969; Schwertmann,  
93 1991), will not be evident in room temperature IRM results. Color and diffuse reflectance methods  
94 also have limitations for detecting or quantifying hematite because they depend strongly on grain  
95 size and crystallinity. Decreasing grain size tends to reduce the reflectance wavelength and  
96 changes the color from purple-red to yellow-red (Cornell and Schwertmann, 2003; Jiang et al.,  
97 2022). Evaluating grain size distributions for pigmentary hematite is, therefore, difficult because  
98 grain size influences most proxies used to estimate hematite properties.

99

100 Microscopy observations reveal the existence of nano-sized hematite with sizes from ~20 nm to a  
101 few hundred nanometers in soils and banded iron formations (Eggseder et al., 2018; Hyodo et al.,  
102 2020; Sun et al., 2015). A more systematic relationship between hematite grain size and  
103 unblocking temperature has been established by Swanson-Hysell et al. (2011, 2019) using Néel  
104 (1949) relaxation theory. The grain size range of remanence-carrying hematite can be inferred  
105 using unblocking temperatures from thermal demagnetization experiments, although this approach  
106 cannot be used to estimate SP particles because they do not carry a stable remanence at room  
107 temperature.

108

109 Grain volume is a key variable in Néel (1949) theory. Dunlop (1965) pointed out that it is possible  
110 to combine field- and temperature-dependent measurements to determine the joint grain volume  
111 ( $V$ ) and microcoercivity at absolute zero ( $H_{k0}$ ) distribution;  $f(V, H_{k0})$ . Jackson et al. (2006)  
112 developed a procedure to estimate  $f(V, H_{k0})$  for particle assemblages that contain both SP and  
113 stable single domain (SSD) magnetite based on backfield remanence curves measured over a range  
114 of temperatures, which they called “thermal fluctuation tomography” (TFT). This method was  
115 used to reconstruct the grain size distribution of magnetite in both synthetic and natural tuff and  
116 paleosol samples. Theoretically, TFT can also be used for weakly magnetic minerals like hematite  
117 that have a wider size range for SSD behaviour (Banerjee, 1971; Kletetschka and Wasilewski,  
118 2002; Özdemir and Dunlop, 2014). Here, we present a TFT procedure to estimate the grain size  
119 and microcoercivity distribution for pigmentary hematite in natural red chert samples based on the  
120 approach of Jackson et al. (2006). Multiple low-temperature magnetic measurements are integrated

121 to constrain the magnetic mineralogy of natural hematite-magnetite-bearing samples. Our results  
122 also provide new insights into the nature of pigmentary hematite in red sedimentary rocks.

123

## 124 **2. Materials and Methods**

### 125 ***2.1. Inuyama red chert***

126 Red chert is a distinctive hematite-rich biosiliceous sedimentary rock, which was a common  
127 pelagic marine sediment type from the Ordovician to the early Late Cretaceous (Jones and  
128 Murchey, 1986). The Inuyama red chert crops out along the Kiso River about 30 km north of  
129 Nagoya, Japan. Red chert, gray chert, and siliceous claystone were deposited alternately over  
130 thicknesses of several hundred meters in the middle Triassic to early Jurassic (Oda and Suzuki,  
131 2000). Hematite occurs as a finely dispersed pigment of chemical origin in red cherts (Jones and  
132 Murchey, 1986; Matsuo et al., 2003). The Inuyama red chert contains variable mixtures of  
133 magnetite and pigmentary hematite (Oda and Suzuki, 2000; Abrajevitch et al., 2011; Hu et al.,  
134 2021). Four representative samples were selected from three red bedded chert sites (KA1, KA6,  
135 UN2) in the Inuyama area. Biostratigraphic, paleomagnetic, and rock magnetic results for the same  
136 sample set have been published by Oda and Suzuki (2000) and Hu et al. (2021). Radiolarian fossils  
137 indicate that the KA1 and UN2 samples have middle (Anisian) and late Triassic (Norian) ages  
138 while two KA6 samples are of early Jurassic age (Oda and Suzuki, 2000).

139

### 140 ***2.2. Low temperature magnetic measurements***

141 Samples were cut into 4 mm × 4 mm × 3 mm pieces and were measured with a Quantum Design  
142 Magnetic Properties Measurement System (MPMS) at the Black Mountain Paleomagnetism  
143 Laboratory, Australian National University. First, an isothermal remanent magnetization (IRM)  
144 was imparted at 10 K in a 5 T field (LTSIRM) after cooling in zero field (ZFC) and then  
145 demagnetized by ramping the superconducting magnet down in oscillation mode from 100 to 0  
146 mT to simulate an alternating field (AF) demagnetization at 10 K (Lagroix and Guyodo, 2017).  
147 The resulting magnetization was then measured from 10 K to 300 K to obtain LTIRM<sub>@AF100</sub>  
148 warming curves. Following the same protocol, LTIRM<sub>@AF300</sub> warming curves were also measured  
149 for the same sample by ramping the magnet down from 300 to 0 mT after imparting a LTSIRM.

150 In this way, magnetizations carried over different coercivity ranges (>300 mT, 100-300 mT, and  
 151 <100 mT) were separated to identify their low temperature characteristics. In this study,  
 152  $LTIRM_{>300 \text{ mT}}$  is represented by  $LTIRM_{@AF300}$ ,  $LTIRM_{100-300 \text{ mT}}$  is given by  $LTIRM_{@AF100} -$   
 153  $LTIRM_{@AF300}$ , and  $LTIRM_{<100 \text{ mT}}$  is calculated as  $LTSIRM - LTIRM_{@AF100}$ . Second, a 5 T field  
 154 was imparted again at 10 K after ZFC and IRM was measured in zero field during warming to 300  
 155 K to obtain ZFC-LTSIRM curves. Samples were then field-cooled (FC) to 10 K in a 5 T field and  
 156 measured during warming back to 300 K after removing the field (FC-LTSIRM). Third, backfield  
 157 demagnetization curves were measured for the same four samples at 50 logarithmically spaced  
 158 steps from 0.001 T to 5 T after being saturated with an initial 5 T field at eight temperatures: 300  
 159 K, 250 K, 200 K, 150 K, 100 K, 80 K, 50 K, and 10 K. These curves were later decomposed into  
 160 skew-normal coercivity components using the fitting software MAX UnMix (Maxbauer et al.,  
 161 2016). Finally, to test for goethite contributions that will be fully demagnetized at 400 K, samples  
 162 were given a room temperature IRM (RTSIRM) in a 5 T field and were demagnetized by ramping  
 163 the magnet from 300 to 0 mT in oscillation mode. The remaining remanence  $RTSIRM_{@AF300}$  was  
 164 measured in zero field during cooling to 150 K and then during warming to 400 K and then during  
 165 cooling back to 150 K.

166

### 167 **3. Thermal fluctuation tomography theory for hematite**

168 We adapted the tomographic imaging method of Jackson et al. (2006) to estimate  $f(V, H_{k0})$   
 169 distributions for SP and SDD hematite grains. The procedure is described briefly below, with focus  
 170 on modifications made for hematite. For a detailed explanation and derivation of TFT theory, see  
 171 Jackson et al. (2006) and Dunlop (1965).

172

173 The TFT approach involves using backfield remanence data to estimate the blocking field ( $H_B$ ).  
 174 For hematite at a given temperature, we evaluate  $H_B = H_{cr} - H_q$ , where  $H_{cr}$  is the coercivity of  
 175 remanence, and  $H_q$  is the thermal fluctuation field. For a randomly oriented population of  
 176 identical grains,  $H_q$  is expressed as (equation 8 of Jackson et al. (2006)):

$$177 \quad H_q = 0.801 \left( \frac{kT\sqrt{H_k(T)}}{\mu_0 VM_S(T)} \right)^{\frac{2}{3}} \ln^{\frac{2}{3}} \left[ \frac{\tau_{exp}}{\tau_0 \mu_0 \Delta H_{DC} \sqrt{\mu_0 H_k(T)}} \times \left( \frac{kT}{VM_S(T)} \right)^{\frac{2}{3}} \right], \quad (1)$$

178 where  $M_s$  (T) and  $H_k$  (T) are the saturation magnetization and microcoercivity as a function of  
 179 absolute temperature, T, respectively,  $\mu_0$  is the permeability of free space ( $4\pi \times 10^{-7}$  H/m),  $k$  is  
 180 Boltzmann's constant ( $1.38 \times 10^{-23}$  J/K),  $V$  is the hematite particle volume, and  $\tau_0$  is a characteristic  
 181 time related to the natural frequency of gyromagnetic precession. For nanosized hematite,  $\tau_0$  is  
 182 found to be  $10^{-12}$  -  $10^{-11}$  s (Henrik, 2014 and references therein). We here assume  $\tau_0$   $10^{-12}$  s. The  
 183 exposure time  $\tau_{exp}$  for the backfield treatments is assigned as 300 s, and  $\Delta H_{DC}$  is the applied field  
 184 difference between successive backfields. We assume here that the saturation magnetization at  
 185 absolute zero ( $M_{S0}$ ) is 2500 A/m for hematite (Dunlop and Özdemir, 1997), then  $M_S(T)$  can be  
 186 represented using Bloch's 3/2 law (Bloch, 1930):

$$187 \quad M_S(T) = M_{S0} \times \left(1 - B \times T^{\frac{3}{2}}\right), \quad (2)$$

188 where B is the Bloch constant. B is determined by the spin-wave stiffness constant; we adopt  $B =$   
 189  $10^{-5}$  for hematite nanoparticles (Martínez et al., 1996).

190

191 The next step is to describe microcoercivity ( $H_k$ ) as the function of temperature. Two analytic  
 192 models have been used previously to describe the temperature dependence of the coercive force.

193 1. By taking  $\frac{H_k(T)}{H_{k0}} = \left(\frac{M_S(T)}{M_{S0}}\right)^n$  (Dunlop and Özdemir, 2000; Jackson et al., 2006; Menyeh  
 194 and O'Reilly, 1995), where n depends on the dominant anisotropy, we can calculate  
 195  $H_k(T)$  based on Bloch's 3/2 law:

$$196 \quad H_k(T) = H_{k0} \left(1 - B \times T^{\frac{3}{2}}\right)^n, \quad (3)$$

197 However, hematite anisotropy can be complex and published n values for fine-grained  
 198 hematite below room temperature are rare. Study of synthetic nano-sized hematite  
 199 reveals that temperature has a minimal impact on  $M_S(T)$  while coercivity increases  
 200 significantly at low temperature due to frozen canted spins (Satheesh et al., 2017).  
 201 Therefore, n should be large because of the significant  $H_k(T)$  change compared to  
 202 minimal  $M_S(T)$  change. Satheesh et al. (2017) reported  $M_s$  and  $H_c$  for a 64 nm hematite  
 203 sample at both 5 K and 300 K, to give a calculated n value of ~10.

204 2. The temperature dependence of coercivity,  $H_c$  (T), can also be expressed by Kneller's  
 205 law (Kneller and Luborsky, 1963):

$$H_c(T) = H_{c0} \left( 1 - \left( \frac{T}{T_B} \right)^\alpha \right), \quad (4)$$

206 where  $T_B$  is the blocking temperature for SP particles,  $\alpha$  is Kneller's exponent and  $H_{c0}$  is  
 207 the coercivity at absolute zero. For non-interacting single domain nanoparticles with  
 208 uniaxial anisotropy,  $\alpha$  usually takes a value of 0.5 (Kuncser et al., 2020; Maaz et al., 2010;  
 209 Osman and Moyo, 2015). However,  $\alpha$  can deviate from 0.5 due to finite size effects at the  
 210 nanoscale as well as due to variations in volume distribution, randomness of anisotropy  
 211 axes, and interparticle interactions (Nayek et al., 2017). Similar to the  $n$  value in equation  
 212 (3),  $\alpha$  for hematite nanoparticles is poorly constrained.  
 213

214  
 215 To establish a thermally dependent coercivity model for pigmentary hematite in Inuyama red chert,  
 216 we compare the hematite median  $H_{cr}$  values obtained from backfield curve decomposition using  
 217 both models. First, we need to clarify the relationship among different coercivity forms,  $H_c$ ,  $H_{cr}$   
 218 and  $H_k$ . Experimental  $H_{cr}/H_c$  ratios for SSD hematite are almost constant at  $\sim 1.5$  (Martin-  
 219 Hernandez and Guerrero-Suarez, 2012; Peters and Dekkers, 2003; Özdemir and Dunlop, 2014;  
 220 Roberts et al., 2021). The relationship between  $H_{cr}$  and  $H_k$  depends largely on the dominant  
 221 anisotropy type. For randomly oriented identical particles with uniaxial anisotropy, Stoner and  
 222 Wohlfarth (1948) theory gives  $H_{cr}/H_k = 0.524$ . Multiaxial anisotropy, such as cubic or hexagonal  
 223 anisotropy, can increase  $H_{cr}$  (Harrison et al., 2019) and therefore raise this ratio close to 1. The  
 224 high magnetostriction of hematite and weak  $M_s$  suggests a high sensitivity to magnetostrictive  
 225 strain in hematite (Banerjee, 1963); this strain-related anisotropy is taken to be uniaxial. FORC  
 226 diagrams for the studied red chert samples have “ridge-type” distributions for hematite up to 1.2  
 227 T (Hu et al., 2021), which is typical of uniaxial SSD particle assemblages (Egli et al., 2010).  
 228 Therefore, by assuming a dominant uniaxial anisotropy and relatively constant  $H_{cr}/H_c$  ratios for  
 229 SP/SSD hematite in the Inuyama red chert, we adopt linear relationships among  $H_c$ ,  $H_{cr}$  and  $H_k$ .  
 230 Then, for model 1, we fit the hematite median  $H_{cr}$  data using equation (3). Under the assumption  
 231 of a common  $n$  value for all samples, we estimate both  $H_{cr0}$  and  $n$  using Bayesian regression.  
 232 Similarly, by assuming a common  $\alpha$  value, we fit the hematite  $H_{cr}$  data using equation (4) and  
 233 obtain median posterior estimates of  $H_{cr0}$ ,  $T_B$ , and  $\alpha$  via Bayesian regression for model 2 (see  
 234 section 4.3 for details). By selecting an appropriate model based on our experimental data (section

235 4.3) and assigning  $H_{cr0} = 0.524H_{k0}$ , we can estimate  $H_k(T)$ . Then  $H_B(T)$  is obtained by substituting  
 236  $H_B = 0.524H_k - H_q$  into equation (1).

237  
 238 After constructing field blocking contours for hematite, we describe each hematite grain using two  
 239 essential attributes,  $V$  and  $H_{k0}$ . A saturating field applied and removed isothermally at temperature  
 240  $T_1$  magnetizes the entire thermally stable population at that temperature (Figure 1, blue shaded  
 241 region), which corresponds to grains with  $(V, H_{k0})$  that plot above and to the right of the zero-field  
 242 blocking contour for  $T_1$  (Figure 1). Subsequent application and removal of a reverse DC field,  $H_1$ ,  
 243 flips the magnetic moments of grains with  $(V, H_{k0})$  that plot below and to the left of the blocking  
 244 contour for  $(T_1, H_1)$  (Figure 1, hatched area). Each backfield reverses the moments of grains that  
 245 plot in a region on the Néel diagram (Dunlop, 1965; Néel, 1949) bounded by two blocking field  
 246 contours for a specified temperature. The change in remanence  $\Delta M_R$  produced by each DC  
 247 backfield treatment can, therefore, be expressed as (equation 11 of Jackson et al. (2006)):

$$248 \quad \Delta M_R = \int f(V, H_{k0}) d\Omega, \text{ and}$$

$$249 \quad \Omega = \left\{ V, H_{k0} \mid H_{i-1} \leq H_B \leq H_i \right\} \quad (5)$$

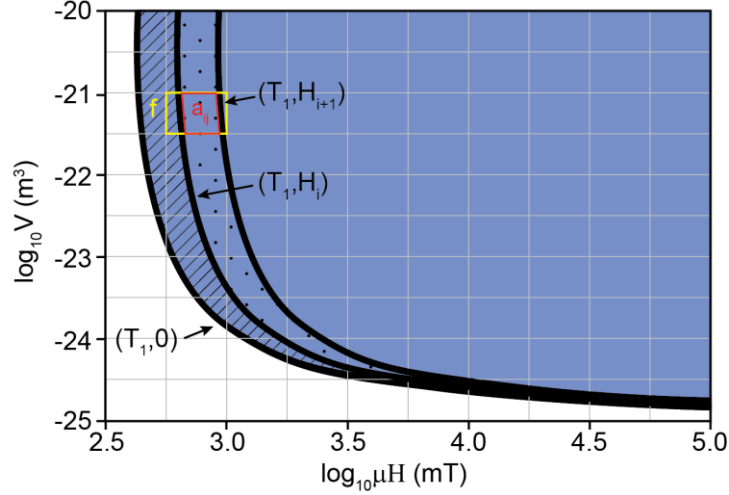
250 where  $\Omega$  represents the region bounded by two blocking field contours and  $H_i$  represents a reverse  
 251 DC field treatment. Therefore, the procedure is essentially an inverse problem involving  $f(V, H_{k0})$   
 252 estimation from a series of DC backfield remanence curves for hematite. Details of procedures  
 253 used to obtain hematite backfield remanence curves are explained in section 4.2.

254  
 255 To estimate  $f(V, H_{k0})$ , we divided the Néel diagram into a rectilinear grid of cells in which  $f$  is  
 256 uniform in each cell (Figure 1, yellow cell). The discrete equivalent of equation (5) is:

$$257 \quad \Delta M_{Ri} = \sum_{j=1}^{n_{\text{cells}}} f_j a_{ij}, \quad (6)$$

258 Where  $a_{ij}$  is the area of cell  $j$  within the area bounded by the blocking contours for a given  
 259 temperature and applied field used when measuring  $\Delta M_{Ri}$  (Figure 1, red region). Each temperature  
 260 and applied field,  $H_{app}$ , pair  $(T, H_{app})$  corresponds to a unique blocking contour, defined as the  
 261 locus of  $(V, H_{k0})$  for which  $H_B(T, V, H_{k0}) = H_{app}$ , so we can calculate intersection points of the

262 contours with the grid lines by piecewise linear interpolation between nodes and approximate the  
 263 contours by straight-line segments between these intersection points to estimate the areas  $a_{ij}$ .



264

265 **Figure 1** Schematic illustration of the TFT technique, modified from Jackson et al. (2006). A  
 266 strong field IRM imparted at temperature  $T_1$  is carried by the entire thermally stable population  
 267 (blue shaded area); a backfield,  $H_1$ , applied and removed at temperature  $T_1$ , reverses the moments  
 268 of grains in the hatched area; a larger backfield,  $H_2$ , further reverses the moments of grains in the  
 269 dotted area.  $a_{ij}$  (red area) represents the area bounded by the blocking contours for  $T_1$  and applied  
 270 fields  $H_{i+1}$  and  $H_i$  when measuring  $\Delta M_{Ri}$ . The yellow rectangle represents the  $j^{\text{th}}$  cell,  $f_j$  is the value  
 271 of  $f(V, H_{k0})$  for the  $j^{\text{th}}$  cell.

272

273 We employ an initialization of  $f = 0$  at all points to generate a forward model based on equation  
 274 (6). Residuals are then calculated as the difference between the measured and model remanence  
 275 data:

$$276 \quad R_i = \Delta M_{Ri, \text{measured}} - \Delta M_{Ri, \text{model}} \quad (7)$$

277 The model is then adjusted by “back-projecting” the residuals:

278

$$279 \quad {}^s \Delta f_{ij} = \frac{R_i a_{ij}}{\sum_{k=1}^{n_{\text{cells}}} a_{ik}^2}. \quad (8)$$

280 The adjustment for cell  $j$  is proportional to  $R_i$  and the area  $a_{ij}$  bounded by the blocking contours.  
 281  $n_{\text{cells}}$  represents the number of cells and  $s$  represents the current simulation. Stepwise updates are  
 282 applied after all calculations for each iteration:

283

$$f_j^{s+1} = f_j^s + \frac{C}{n_{\text{measurements}}} \sum_{i=1}^{n_{\text{measurements}}} \Delta f_{ij} \quad (j = 1 \dots n_{\text{cells}}). \quad (9)$$

C is a dimensionless constant used to control the rate of convergence, where higher values cause more rapid convergence, but excessive values can cause the process to become unstable and diverge. Our aim is to reduce the fitting error to ~10% within 100 iterations; after multiple attempts, we found that a C value of 50 generally meets our requirement.

## 4. Results

### 4.1. Unblocking of pigmentary hematite

LTSIRM variations of different coercivity fractions for both Triassic and Jurassic red chert samples are shown in Figure 2. The Verwey transition for magnetite is clearly evident at ~120 K for particles with coercivity < 300 mT, which disappears or becomes less noticeable in  $LTIRM_{>300}$  curves for the high coercivity component (Figure 2a, 2b), and demonstrating that the coercivity of magnetite is mostly less than 300 mT. For Jurassic specimens,  $LTIRM_{>300}$  warming curves decay steeply compared to the relatively flat  $LTIRM_{<100}$  curves (Figure 2b), which indicates a wide unblocking temperature distribution of a SP hematite content. A concave shape around 200 K is present in  $LTIRM_{>300}$  curves, but not in the low coercivity component, which indicates a likely Morin transition that was not completely smeared out by progressive unblocking of fine hematite (Figure 2b). The  $LTIRM_{100-300}$  warming curve contains both a Verwey transition and marked low temperature unblocking, which suggests a mixture of magnetite and finer hematite in this coercivity range. Hematite unblocking is less significant for Triassic samples, which indicates a smaller SP hematite contribution (Figure 2a). However,  $LTIRM_{>300}$  curves for both Triassic and Jurassic samples have comparable magnetizations despite the fact that magnetite has a much stronger magnetization, which indicates that hematite dominates the red chert magnetism by mass.

A Verwey transition is clearly present in both ZFC-LTSIRM and FC-LTSIRM curves, while a Morin transition is likely smeared by progressive unblocking of SP hematite (Figure 2c, 2d). ZFC-LTSIRM and FC-LTSIRM curves are not widely separated, which contrasts with the behavior of

312 goethite-rich samples (Guyodo et al., 2003; Liu et al., 2006; Huang et al., 2019). Given that the  
313 curves almost overlap (Figure 2c, 2d) it is inferred that any goethite contribution is insignificant.

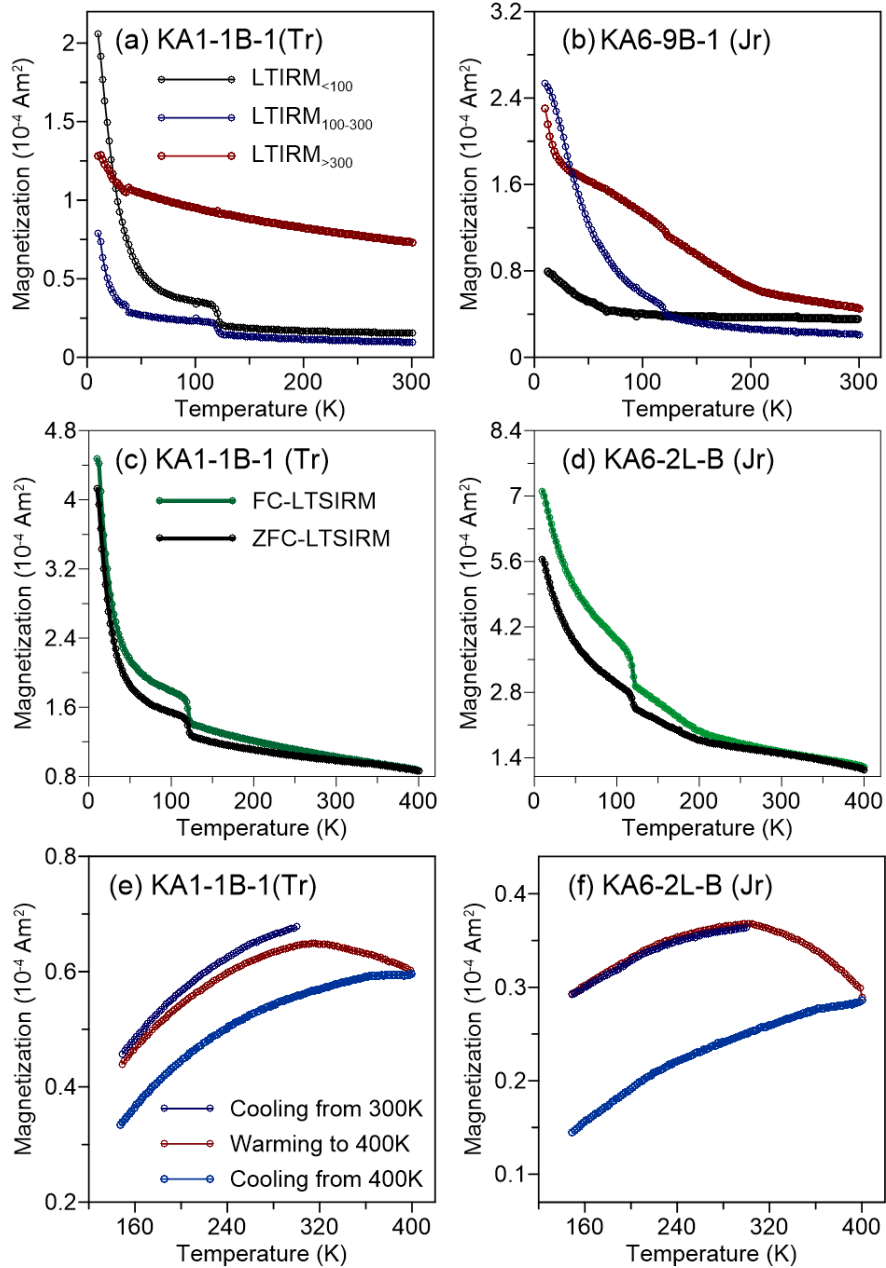
314

315 After removing the low coercivity contribution by applying a 300 mT AF,  $RTSIRM_{@AF300}$   
316 warming curves decrease gradually from 300 K to 400 K with a net remanence loss during re-  
317 cooling (Figure 2e, 2f). No sharp drop is seen at the Néel temperature for goethite. The gradual  
318 decrease in warming curves above 300 K is likely due to unblocking of slightly larger hematite  
319 particles near the SP/SSD size threshold at room temperature.

320

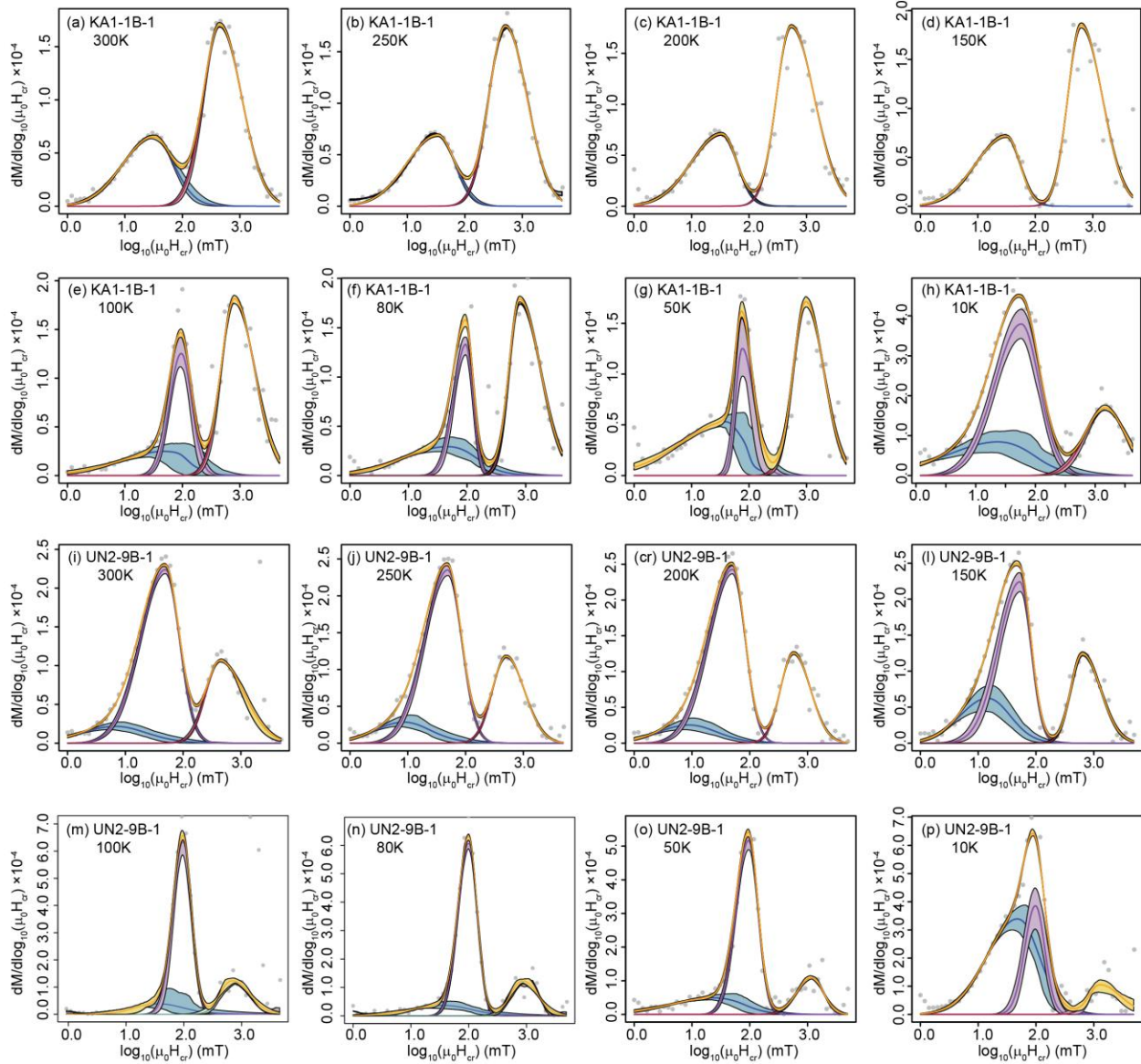
#### 321 ***4.2. Coercivity distributions for pigmentary hematite***

322 The results shown in Figure 2 indicate that goethite is not magnetically important in the Inuyama  
323 red chert and that magnetite is mostly confined to the low coercivity component ( $< 300$  mT). We  
324 further examine coercivity spectra at eight temperatures from 10 K to 300 K. At room temperature,  
325 most Triassic and Jurassic specimens are well fitted with two skew-normal distributions (Figures  
326 3a, 4a, 4i). One distribution has a 19-35 mT median coercivity and extends from 0 to  $\sim 500$  mT  
327 (based on  $\pm 3$  standard deviations from the median coercivity). The other distribution has a higher  
328 median coercivity of 413-598 mT and extends from  $\sim 60$  mT to  $\sim 6$  T, which is likely to be due to  
329 SSD hematite. Triassic sample UN2-9B-1 has an additional lowest-coercivity contribution with a  
330 broad distribution that extends to  $\sim 200$  mT (Figure 3i). At room temperature there is only a small  
331 overlap between the low- and high-coercivity components. With decreasing temperature, the  
332 overlap is reduced and finally disappears or becomes insignificant below 100 K. This behavior is  
333 consistent with hematite coercivity increasing with decreasing temperature (equations (3) and (4)),  
334 while magnetite has a much less dramatic coercivity change with temperature (Özdemir et al.,  
335 2002). The low-temperature dividing point of the low-coercivity component appears at  $\sim 250$  mT,  
336 which is consistent with the Verwey transition being significant in the  $IRM_{<300}$  component (Figure  
337 2a, 2b). Therefore, for both Triassic and Jurassic specimens, the hematite population can be well  
338 separated from magnetite based on their coercivity distributions.



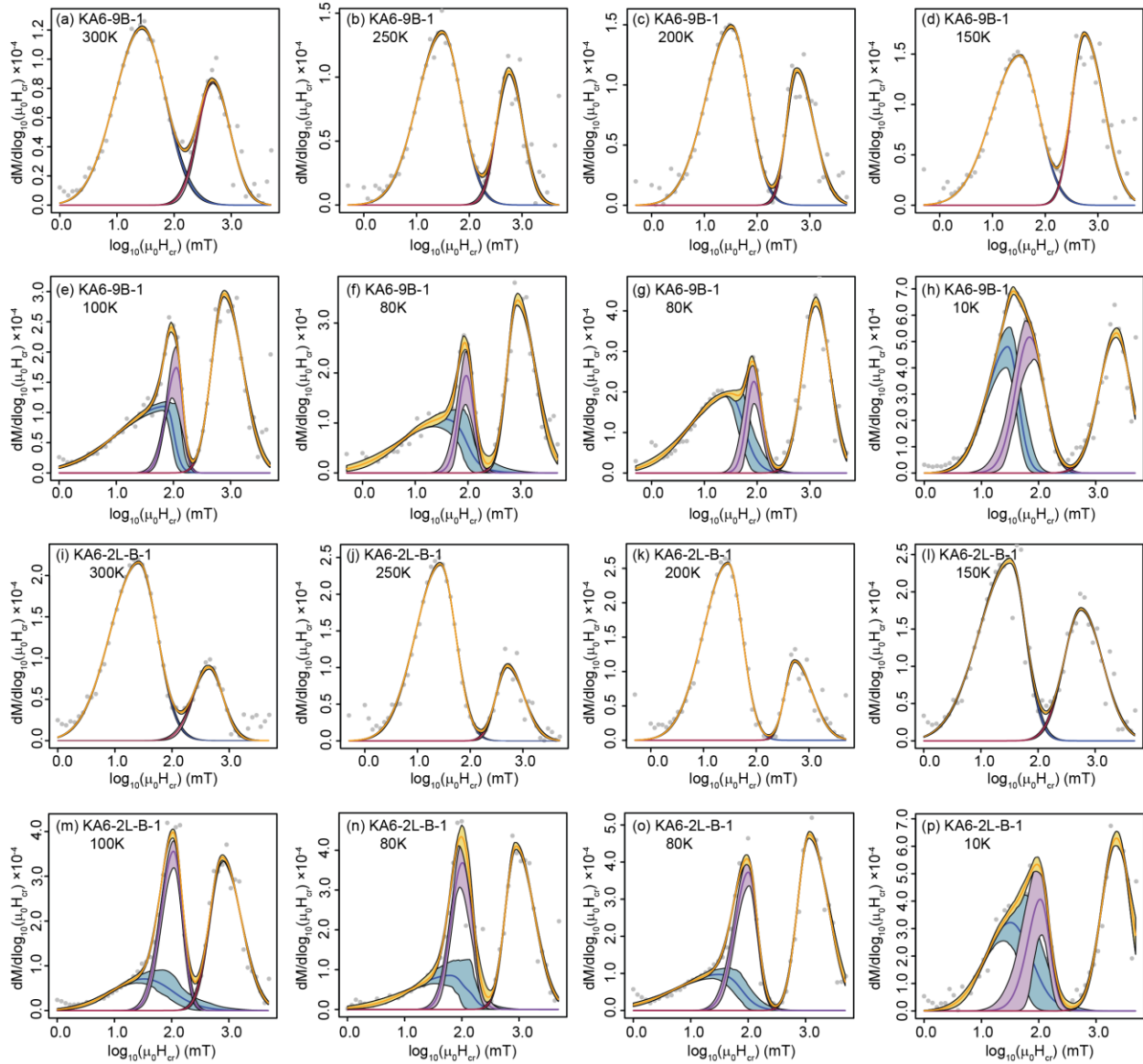
339

340 **Figure 2** LTSIRM variations versus temperature. (a, b) Samples were given a SIRM in a 5 T field  
 341 at 10 K and then AF demagnetized in peak fields of 100 and 300 mT, respectively. Then the  
 342 LTSIRM was measured during warming for components with coercivity ranges of  $< 100$  mT  
 343 (black), between 100 and 300 mT (blue line), and  $> 300$  mT (red). (c, d) ZFC (black) and FC  
 344 (green) LTSIRM curves. (e, f) Samples were saturated in a 5 T field at 300 K and then AF  
 345 demagnetized in a 300 mT peak field. The  $RTSIRM_{@AF300}$  was then measured during cooling to  
 346 150 K (dark blue), warming to 400 K (red), and then cooling back to 150 K (light blue). Tr =  
 347 Triassic; Jr = Jurassic.



348

349 **Figure 3** Coercivity spectra from backfield SIRM demagnetization curves for two Triassic  
 350 specimens (KA1-1B-1, Anisian; UN2-9B-1, upper Norian). The data were fitted using skew-  
 351 normal distributions with the Max Unmix software (Maxbauer et al., 2016). We fitted data with a  
 352 minimum number of components. At eight temperatures, the data can be fitted with 2-3  
 353 components: the lowest coercivity component is shown in blue, the intermediate coercivity  
 354 distribution in purple, and the highest coercivity distribution in red. Yellow lines represent the sum  
 355 of all components, while grey dots represent the data. Shaded areas are 95% confidence intervals  
 356 for each component.

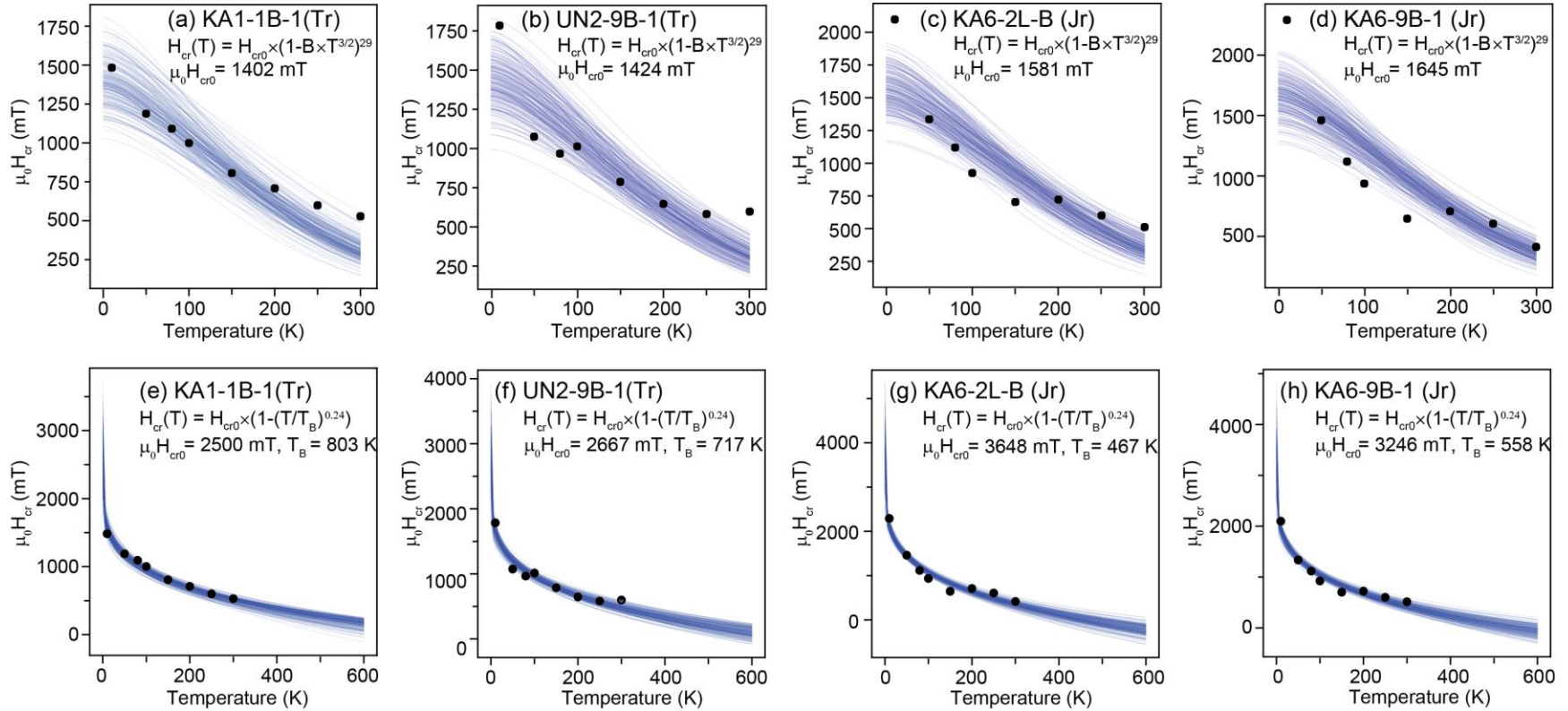


357

358 **Figure 4** Coercivity spectra from backfield SIRM demagnetization curves for two Jurassic  
 359 specimens (KA6-9B-1; KA6-2L-B-1 from early Jurassic). Formatting is the same as Figure 3.

360

361



362

363

364

365

366

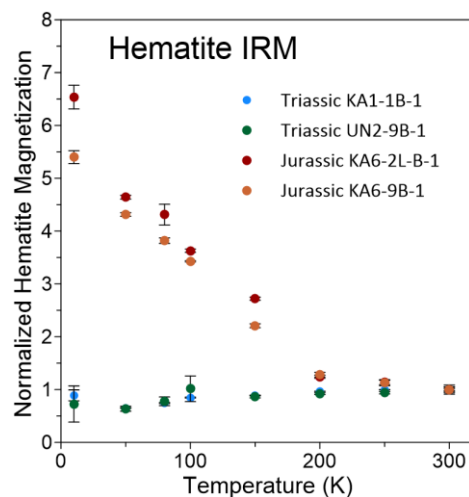
367

368

369

**Figure 5** Hematite median remanent coercivity variation with temperature. (a-d) Bayesian posterior distribution of fitted curves based on equation (3) given the priors listed in Appendix A and assuming a common  $n$  value for all samples. (e-h) Bayesian posterior distribution of fitted curves based on equation (4) given the Bayesian priors listed in Appendix A and assuming a common value of Kneller's  $\alpha$  exponent for all samples. The  $n$  and  $\alpha$  parameters,  $T_B$  shown in the equations are the median values from the parameter posterior distributions. Standard deviations and other posterior distribution statistics are provided in Appendix A.

370 Increases in the coercivity of hematite with decreasing temperature are illustrated in Figure 5.  
 371 Below  $\sim 150$  K, the increase is steeper; it triples for Triassic specimens and increases five-fold for  
 372 Jurassic specimens at 10 K compared to room temperature. The coercivity-temperature fits in  
 373 Figures 5a-5d and 5e-5h were made using equations (3) and (4), respectively, using Bayesian  
 374 regression (Appendix A). In this study, we assume that the exponent parameter  $n$  or  $\alpha$  is constant  
 375 for pigmentary hematite in Triassic/Jurassic Inuyama red chert. Under this assumption, we  
 376 combine all 32 data points from four specimens at eight temperatures to estimate a common  $n$  and  
 377  $\alpha$  posterior distribution and individual posterior distributions of  $H_{cr0}$  and  $T_B$  for each specimen by  
 378 Bayesian regression (see Appendix A for details). As expected, large  $n$  values of 22 - 36 (97%  
 379 high density interval) are obtained, which demonstrates that the hematite coercivity increases more  
 380 strongly than  $M_s$ . However, these fits are less satisfying at low- and room-temperature. The fits  
 381 tend to underestimate  $H_{cr0}$  and the coercivity close to room temperature due to the flatness of the  
 382 fitted curves, which largely comes from the  $3/2$  exponent. Fits based on equation (4) achieve better  
 383 results (Figure 5e-5h). The posterior  $\alpha$  ranges from 0.151 to 0.339 (97% high density interval) with  
 384 median value of 0.24. Triassic red chert samples have lower  $H_{cr0}$  and higher  $T_B$  than Jurassic red  
 385 cherts. Low  $T_B$  values of  $\sim 194$  °C and  $\sim 285$  °C are predicted for hematite in Jurassic red cherts,  
 386 which suggests they have a fine grain size.



387  
 388 **Figure 6** Hematite IRM variation with temperature. Data are normalized by hematite IRM at 300  
 389 K for each sample. Error bars represent fitting errors for the hematite component.

390

391 Distinctively IRM intensity changes for hematite with temperature are shown for Triassic and  
392 Jurassic samples, respectively, in Figure 6. The hematite remanence remains relatively constant  
393 for the Triassic specimens (blue and green dots), which indicates that almost all of the hematite is  
394 in the SSD state at room temperature. In contrast, hematite remanence increases exponentially with  
395 decreasing temperature for the Jurassic samples (brown and red dots), which indicates a significant  
396 SP contribution with a wide blocking temperature range.

397

#### 398 ***4.4. Tomographic Analysis***

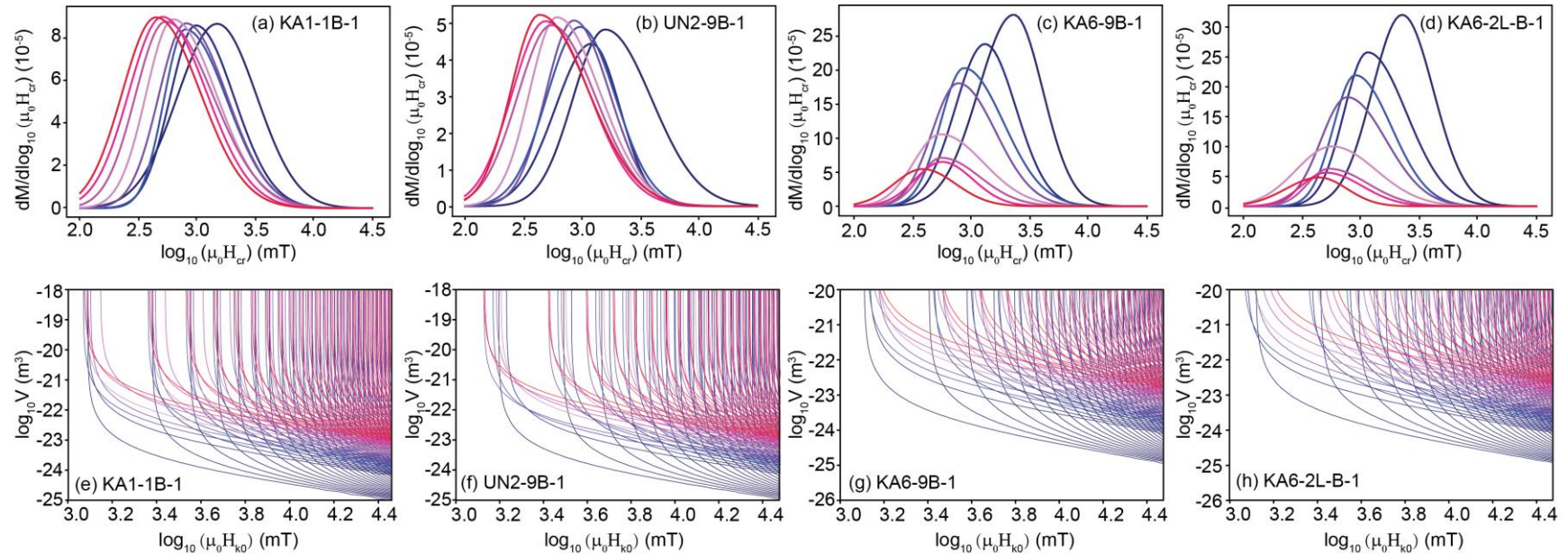
399 Based on the above results, for our tomographic analysis we adopted Kneller's law as a coercivity-  
400 temperature relationship with  $\alpha = 0.24$  and  $H_{cr} = 0.524H_k$ . The median  $T_B$  values shown in Figure  
401 5e-5f are used for each specimen to calculate hematite blocking contours. Hematite coercivity  
402 distributions extracted from the high-coercivity component fitting in Figures 3 and 4 are shown in  
403 Figure 7a-7d. Each dataset contains 808 backfield remanence data points (101 field steps at each  
404 of eight temperatures). These data are combined with equations (1) and (4) and are mapped into  
405 blocking contours (Figure 7e-7h).

406

407 Upon cooling to 10 K, all backfield derivative curves shift progressively to higher coercivities as  
408 expected. Peak heights are roughly constant for Triassic samples but increase significantly upon  
409 cooling for Jurassic samples (Figure 7). This indicates a greater SP hematite content that blocks  
410 gradually with cooling in Jurassic red chert, while the Triassic red chert is dominated by coarser  
411 SSD hematite. The blocking contour density is nonuniform, so poor resolution is expected for  
412 particles smaller than  $\sim 10$  nm with microcoercivities less than  $\sim 1$  T.

413

414 After determining the blocking contours, we start the iterative process to calculate the joint grain  
415 size and microcoercivity distribution of hematite particles. Best-fit backfield derivative curves  
416 reproduce large-scale features of the measured spectra, while still containing higher frequency  
417 deviations (Figures A2-A5). Fitting errors are below 15% for all samples.



418

419 **Figure 7** Hematite backfield remanence data and blocking contours for Triassic and Jurassic red cherts. (a-d) Hematite coercivity  
 420 distributions extracted from backfield LTSIRM decomposition at eight temperatures from 10 K to 300 K. (e-h) Blocking contours for  
 421 the fields and temperatures in the corresponding datasets above. The equations in Figure 5e-5h are used for each respective specimen.  
 422 Color variations indicate temperature changes from 10 K (blue) to 300 K (red).

423

424

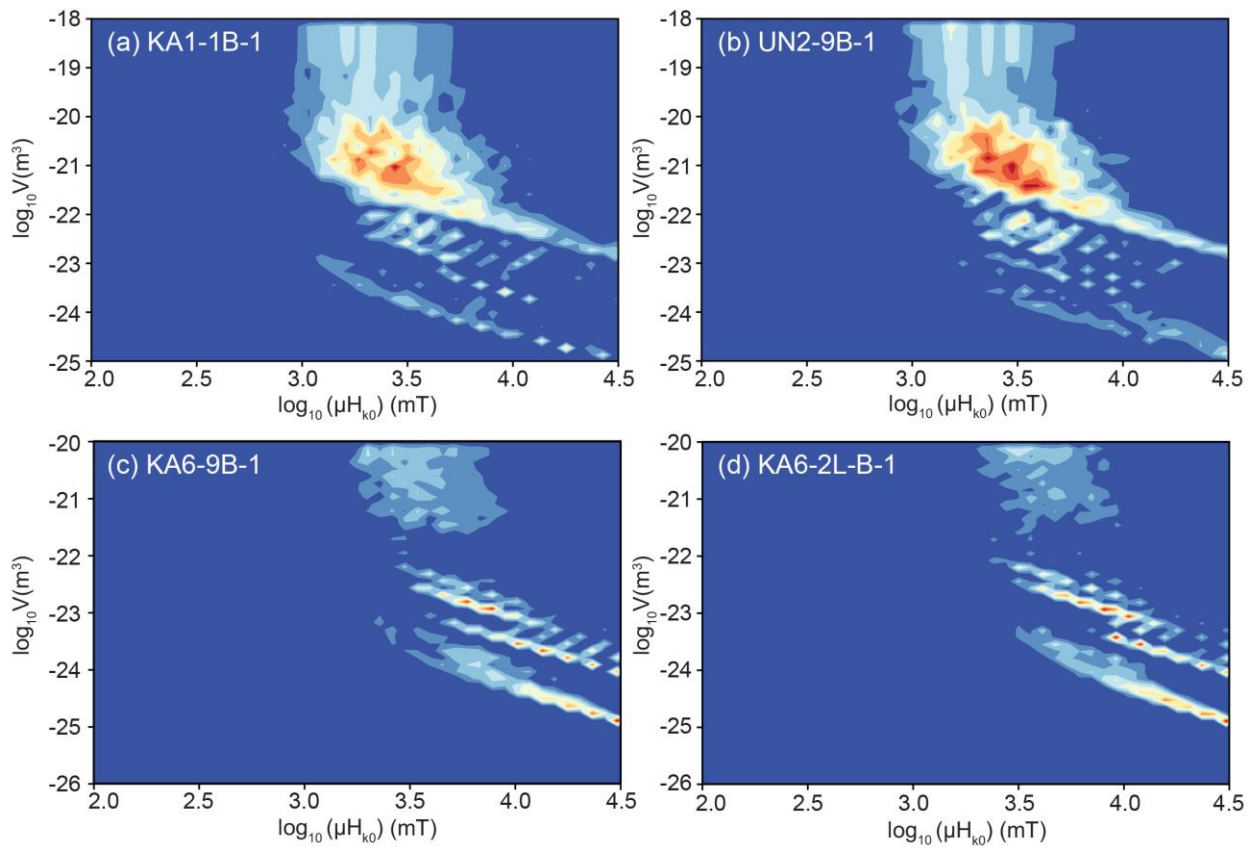
425

426

427

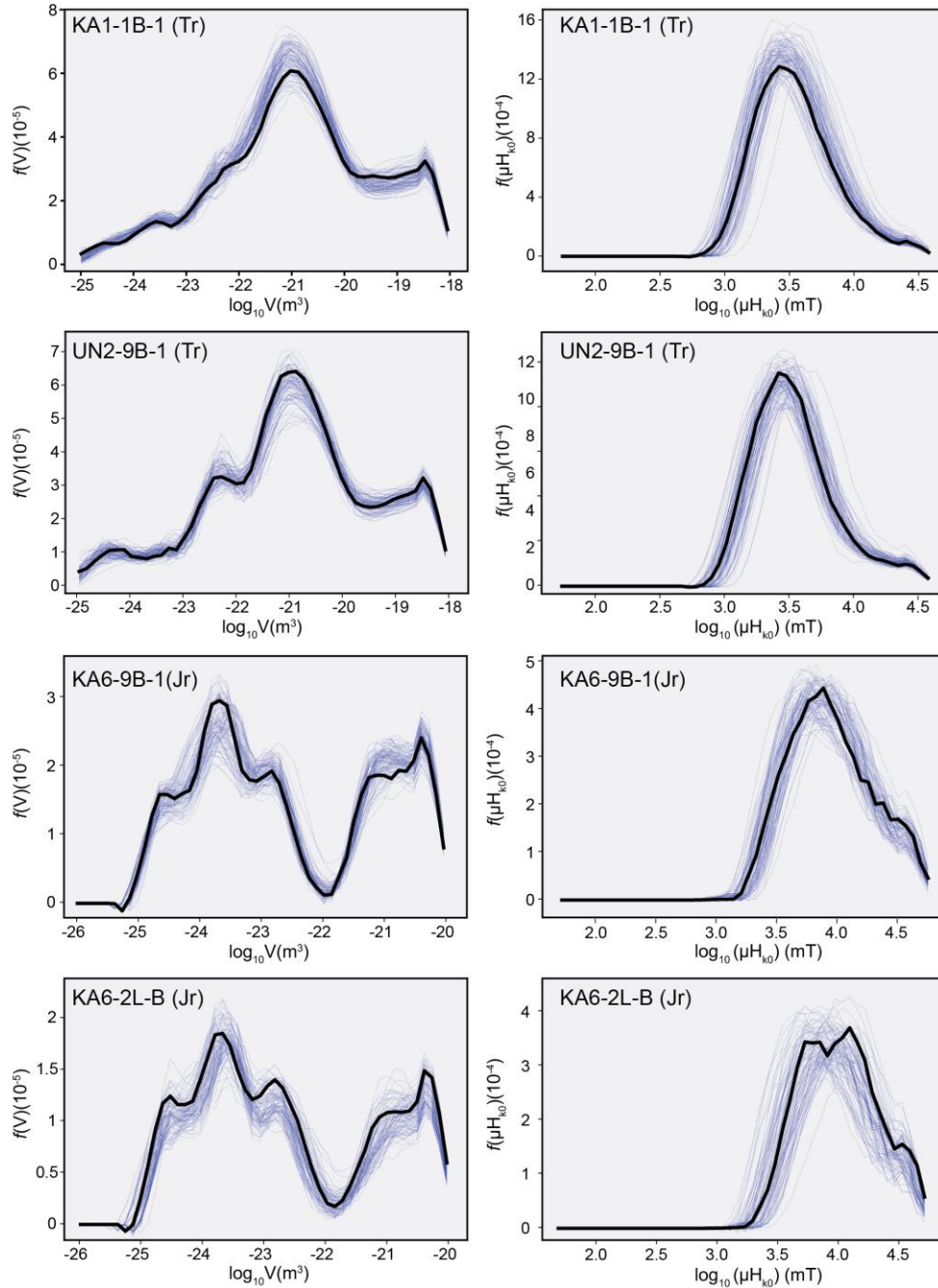
428

429 Estimated  $f(V, H_{k0})$  distributions for Triassic samples have a continuous feature centering at  
 430 volumes around  $1 \times 10^{-21} \text{ m}^3$  and microcoercivities between 1 T and 10 T (Figure 8a, 8b). The  
 431 central volumes are equivalent to spherical hematite particles with  $\sim 75 \text{ nm}$  diameters. In Jurassic  
 432 samples, the hematite particles are smaller but magnetically harder (Figure 8c, 8d), with more  
 433 discrete distributions centered around volumes of  $\sim 1 \times 10^{-25} \text{ m}^3$ ,  $\sim 1 \times 10^{-23.5} \text{ m}^3$ ,  $\sim 1 \times 10^{-22.5} \text{ m}^3$ , and  
 434  $> 1 \times 10^{-22} \text{ m}^3$ , which correspond to diameters of  $\sim 3 \text{ nm}$ ,  $\sim 11 \text{ nm}$ ,  $\sim 24 \text{ nm}$ , and  $> 35 \text{ nm}$  for  
 435 spherical hematite. The microcoercivity of Jurassic hematite ranges from 3 T to  $> 30 \text{ T}$ . There is  
 436 clear elongation of the distribution toward the lower right, along with the dominant blocking  
 437 contour orientation, which may be an artifact of the inversion process (Jackson et al., 2006).  
 438



439  
 440  
 441 **Figure 8** Estimated  $f(V, H_{k0})$  for (a, b) Triassic and (c, d) Jurassic red chert samples from the  
 442 data in Figure 6a-d. Contour interval =  $f_{\text{max}}/30$ .

443  
 444



445

446 **Figure 9** Volume and microcoercivity distributions obtained by summing the rows and columns  
 447 of the 2D model. The data were smoothed with a Savitzky-Golay filter with window length of 5  
 448 in ‘nearest’ mode using the Python Scipy.signal package. Thick black lines represent the median  
 449 value; light blue lines represent calculations based on 100 randomly drawn  $T_B$  and  $\alpha$  values from  
 450 the Bayesian posterior distribution in Figure A1, which are used to indicate the uncertainty on  
 451 the calculation of the volume and microcoercivity distribution.

452 Bayesian modeling was used to calculate the volume and microcoercivity distributions shown in  
453 Figure 9. Thick black lines represent the median volume and microcoercivity distribution for each  
454 sample based on median  $T_B$  and  $\alpha$  values. The light blue lines represent calculations based on 100  
455 randomly drawn  $T_B$  and  $\alpha$  values from their Bayesian posterior distribution in Figure A1, which  
456 indicates the uncertainty on the volume and microcoercivity distribution calculation. The  
457 marginalized microcoercivities are nearly lognormally distributed. Additional high  
458 microcoercivity contributions ( $> 10$  T) are more evident in the Jurassic hematite than Triassic  
459 hematite. By contrast, volume distributions are asymmetrical and more complex. Triassic hematite  
460 populations have a small peak at  $1 \times 10^{-23}$  to  $1 \times 10^{-22}$   $m^3$  and then gradually increase to a major peak  
461 at  $\sim 1 \times 10^{-21}$   $m^3$  (Figure 9a). Additional coarse particles with volume larger than  $1 \times 10^{-20}$   $m^3$  are also  
462 present. The Jurassic hematite population has a roughly bimodal distribution separated at around  
463  $1 \times 10^{-22}$   $m^3$ . The larger particle population has a broad peak from  $1 \times 10^{-22}$   $m^3$  to  $1 \times 10^{-20}$   $m^3$ . The  
464 smaller particle population has a major peak at  $\sim 1 \times 10^{-24}$   $m^3$  with two smaller peaks at  $1 \times 10^{-24.6}$   $m^3$   
465 and  $1 \times 10^{-23}$   $m^3$ , which correspond to their discrete components in Figure 8c, 8d. The discrete  
466 nature of the distribution is most likely due to the limited numbers of temperatures used here  
467 because the distributions are all elongated along the unblocking contours. Nevertheless, two grain  
468 size populations are evident in Jurassic samples; the finer fraction ranges from a few nanometers  
469 to  $\sim 35$  nm in diameter while the coarser fraction is from  $\sim 35$  nm to  $\sim 160$  nm in diameter and is  
470 comparable with Triassic samples.

471

## 472 **5. Discussion**

### 473 ***5.1. Coercivity of pigmentary hematite in red chert***

474 Early studies of the Inuyama red chert reported large saturating fields of up to several tesla for  
475 pigmentary hematite from IRM acquisition curves (Oda and Suzuki, 2000; Shibuya and Sasajima,  
476 1986). In our results, room temperature  $\mu_0 H_{cr}$  ranges from  $\sim 60$  mT to  $\sim 6$  T in Triassic red chert  
477 and from  $\sim 70$  mT to  $\sim 3$  T in Jurassic red chert (Figures 3 and 4), which is comparable to recent  
478 studies (Abrajevitch et al., 2013; Hu et al., 2021). Published data for pigmentary hematite in red  
479 beds have a similarly wide range of  $\mu_0 H_{cr}$  values. In the Deer Lake Group red beds of western  
480 Newfoundland, hematite remanent coercivity ranges from  $\sim 60$  mT to 3 T (Bilardello and Kodama,  
481 2010a), and for red beds from the Maritime provinces of Canada, it varies from  $\sim 40$  mT to 5 T and

482 beyond (Bilardello and Kodama, 2010b). Hematite in Triassic red beds from South China has  
483 remanent coercivity values from ~60 mT to 3 T (Jiang et al., 2017). For zebra rock in Western  
484 Australia, strong fields up to 3 T are needed to saturate hematite (Abrajevitch et al., 2018). North  
485 American red siltstone intraclasts have remanent coercivity of ~100 mT to 1.8 T and beyond  
486 (Swanson-Hysell et al., 2019). Thus,  $\mu_0 H_{cr}$  values of ~60 mT to ~3 T are typical of natural  
487 pigmentary hematite in red beds, although values up to even ~6 T are sometimes observed. This  
488  $\mu_0 H_{cr}$  range gives an idea of the remanent coercivity distribution of natural SSD pigmentary  
489 hematite.

490

491 We further illustrate remanent coercivity variations with temperature for pigmentary hematite.  $H_{cr}$   
492 increases exponentially with decreasing temperature, following the  $T^\alpha$  law, where  $\alpha = 0.24$  is the  
493 median posterior value for red chert samples in this study (Figure 5e, 5f, 5g, 5h). This behavior  
494 can be understood by considering thermal fluctuation effects of blocked moments across an  
495 anisotropy barrier (Maaz et al., 2010). For natural pigmentary hematite, this simple thermal  
496 activation model appears to be applicable from 10 K to 300 K. The significant  $H_{cr}$  increase at low  
497 temperatures also provides a way to separate a hematite component from magnetite. Based on  
498 results in Figures 2 and 3, there is almost no overlap between magnetite and hematite components  
499 below 100 K.

500

501 Quintupled hematite  $M_{rs}$  values at 10 K compared to room temperature confirms the presence of a  
502 large SP hematite population in the Jurassic red chert (Figure 6). The steep  $M_{rs}$  rise below 200 K  
503 indicates that the blocking temperature of most SP hematite is below 200 K. Our results  
504 demonstrate that decomposition of low temperature backfield curves reveals and potentially  
505 enables quantification of entire pigmentary hematite populations, especially SP particles. Although  
506 SP signatures are detected in remanent FORC diagrams (Hu et al., 2021), these signals tend to be  
507 dominated by magnetite because FORC diagrams reflect bulk signals and the magnetization of  
508 hematite is more than two hundred times lower than magnetite (Dunlop and Özdemir, 1997).

509

510 Compared to room-temperature  $H_{cr}$ , which only represents SSD populations,  $H_{k0}$  provides a  
511 measure of the entire hematite population, including SP particles. In the calculations of Jackson et  
512 al. (2006),  $\mu_0 H_{k0}$  values for magnetite in a Tiva Canyon Tuff sample can extend to 300 mT, which

513 is the upper limit for prolate spheroids with magnetite-like magnetizations. According to our  
514 calculations,  $\mu_0 H_{k0}$  for the pigmentary hematite can be much higher, and varies from 1 T to  $\sim 10$  T  
515 in Triassic red chert and from  $\sim 1.5$  T to  $> 30$  T in Jurassic red chert (Figure 9). As is the case for  
516 magnetite, microcoercivity distributions for hematite are nearly symmetric in logarithmic space  
517 (Figure 9).

518

519 The high coercivity of pigmentary hematite cannot be explained by shape anisotropy (Banerjee,  
520 1971). Özdemir and Dunlop (2014) concluded by studying MD hematite that both magnetoelastic  
521 and magnetocrystalline effects contribute to coercivity. However, magnetocrystalline anisotropy  
522 causes a gradual coercivity decrease during cooling below room temperature (Liu et al., 2010;  
523 Özdemir et al., 2002), which is opposite to the temperature dependence of coercivity observed  
524 here. The increasing coercivity trend with cooling in pigmentary hematite is interpreted to be due  
525 to magnetoelastic anisotropy, which arises from crystal defects, dislocations, or internal strain  
526 (Sunagawa and Flanders, 1965; Sunagawa, 1960; Liu et al., 2010).

527

## 528 ***5.2. Grain size distribution and unblocking temperature of pigmentary hematite in red chert***

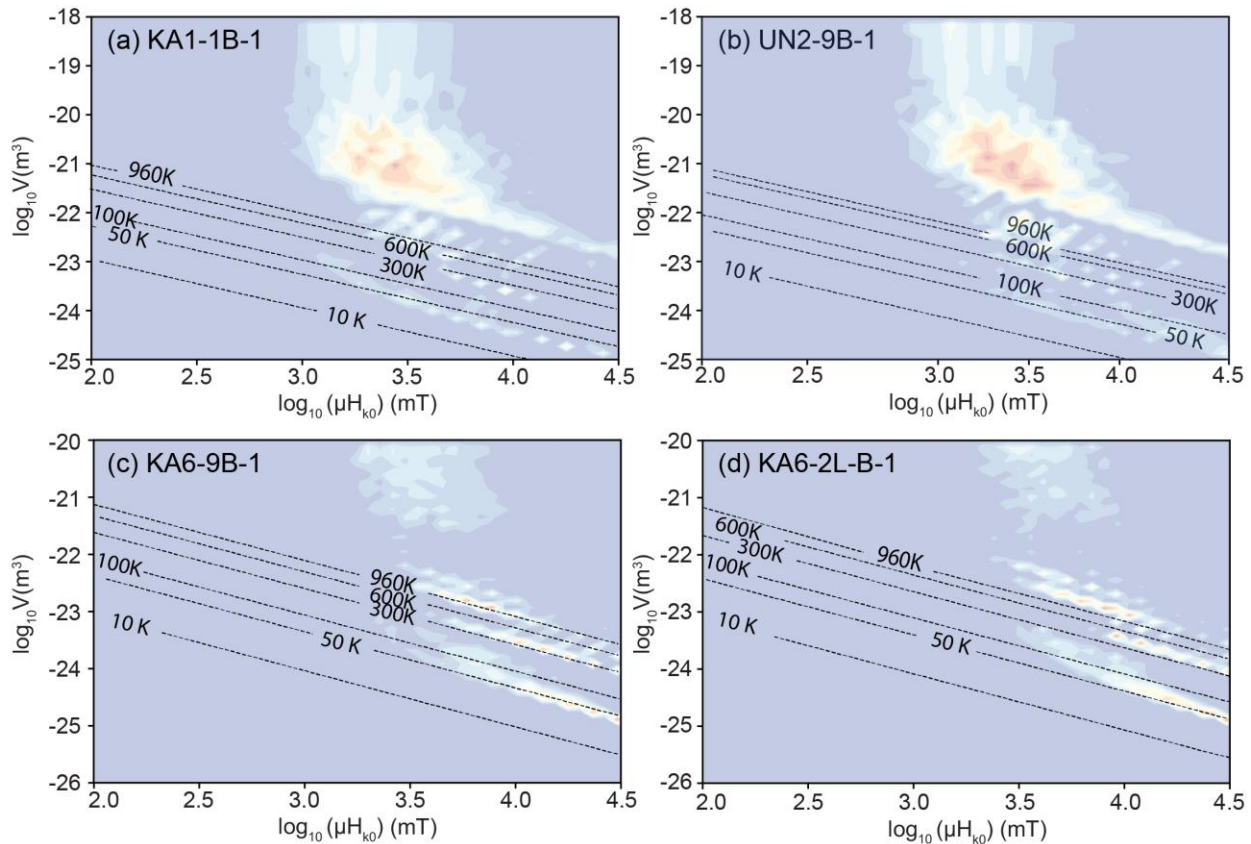
529 Our analysis reveals that both Triassic and Jurassic red chert samples have hematite population  
530 with median size of  $\sim 75$  nm. Additional large amounts of finer hematite  $< \sim 35$  nm occurs in the  
531 Jurassic red chert (Figure 9). The median  $T_B$  for each red chert sample is  $529$  °C (KA1-1B-1),  
532  $438$  °C (UN2-9B-1),  $194$  °C (KA6-2L-B-1), and  $285$  °C (KA6-9B-1). The low unblocking  
533 temperatures are also consistent with the small particle size of pigmentary hematite. According to  
534 the unblocking temperature and grain size model of Swanson-Hysell et al. (2011, 2019), the  
535 median unblocking temperatures in red chert correspond to grain sizes of 100-160 nm, which is  
536 within the range of our calculated grain size distributions. The broad unblocking temperature  
537 distribution reflects the wide size distribution of natural pigmentary hematite.

538

539 We further calculated  $T_B$  contours based on the volume and microcoercivity distributions obtained  
540 here (Figure 10). Almost the entire pigmentary hematite population in the Triassic red cherts is in  
541 the SSD state at room temperature, with unblocking temperatures generally above 300 K (Figure  
542 10a, b). For the Jurassic red cherts, a significant part of the hematite is in the SP state with

543 unblocking temperatures extending below 100 K. The SP/SSD threshold size for stoner-wohlfarth  
 544 hematite has been estimated at 25-30 nm (Banerjee, 1971; Özdemir & Dunlop, 2014) and at 17  
 545 nm for Al-hematite (Jiang et al., 2014). From our  $T_B$  calculations, the SP/SSD threshold size for  
 546 stoichiometric hematite in the Jurassic red cherts is 7-18 nm, which is close to estimates for Al-  
 547 hematites.

548



549

550 **Figure 10** Calculated blocking temperature contours from 10 K to 960 K with  $f(V, H_{k0})$

551 distributions for (a, b) Triassic and (c, d) Jurassic samples.

552

553 Detailed paleomagnetic studies have been conducted on the Inuyama red chert, with four  
 554 remanence components identified from stepwise thermal demagnetization (Oda and Suzuki, 2000;  
 555 Shibuya and Sasajima, 1986). The four components are labeled A (70-200 °C), B (200-350 °C), C  
 556 (350-530 °C), and D (530-680 °C). Components B and C were thought to be Late Cretaceous  
 557 remagnetizations, although the remagnetization mechanism has been debated. Partial thermal  
 558 demagnetization (ThD) after alternating field (AF) demagnetization at 80 mT reveals the same

559 four components (Oda and Suzuki, 2000), which indicates that hematite was at least partly  
560 responsible for all four components. This is consistent with the wide unblocking temperature range  
561 for hematite in our calculations. Paleomagnetic studies of the Inuyama red chert have all suggested  
562 that magnetite is the dominant remanence carrier for components A, B, and C and, thus, magnetite  
563 carries the remagnetizations. However, pigmentary hematite should also contribute to the  
564 remagnetizations due to its low unblocking temperature, especially for Component B. We suggest  
565 this because the unblocking temperature range of component B (200-350 °C) and C (350-530 °C)  
566 spans the median hematite unblocking temperature range. Meanwhile, little magnetization for  
567 component B was lost between 200 and 350 °C in the original ThD experiment (Figure 6a from  
568 Oda and Suzuki (2000)), but the magnetization drops significantly after AF demagnetization of 80  
569 mT (Figure 6c in Oda and Suzuki (2000)). According to our analysis on the magnetite remanent  
570 coercivity distribution of the Inuyama red chert at room temperature (Figure 3 and Figure 4), an  
571 alternating field of 80 mT will demagnetize most of the magnetite, which suggests that the more  
572 significant unblocking feature of component B after AF demagnetization is likely due to  
573 pigmentary hematite.

### 574 ***5.3. Limitations of the TFT method for reconstructing hematite grain size distributions***

575 There are two main limitations of the TFT technique for hematite. First, it has the same limitation  
576 for hematite as it does for magnetite (Jackson et al., 2006). Reconstructed size distributions are  
577 elongated toward the upper left and lower right-hand sides of the Néel diagram, along the blocking  
578 contour orientation. This elongation can be due to artifacts in the inversion method, the physical  
579 model, and the assumption made, as shown by Jackson et al. (2006) and Dunlop (1965). Resolution  
580 limits also remain for inversion due to the restricted orientation distribution of integration paths.  
581 Areas of marginal resolution are sampled sparsely by subparallel contours, such as within the small  
582  $V$ , high  $H_{k0}$  region that is stable only at the lowest temperatures. At the same time, given the small  
583 numbers of temperatures employed, the resolution of our results is imperfect, and stripes are  
584 evident in the  $f(V, H_{k0})$  distribution rather than a smooth continuous distribution (Figure 8c, d).  
585 Increasing the number of temperature steps will improve the resolution, but will also be time and  
586 helium expensive, especially for multiple specimens.

587

588 Second, compared to magnetite, an additional challenge when modeling hematite is the complexity  
589 of its anisotropy. An important assumption in our calculation is that we assign  $H_{cr} = 0.524H_K$ ,  
590 which is based on Stoner and Wohlfarth (1948) theory for identical randomly oriented uniaxial  
591 particles. Harrison et al. (2019) simulated remanence FORC diagrams for particles with uniaxial,  
592 cubic, and hexagonal anisotropy. Among these anisotropy types, randomly oriented, non-  
593 interacting particles with uniaxial anisotropy have the lowest  $H_{cr}$  values, while  $H_{cr}$  for cubic and  
594 hexagonal anisotropy is approximately 1.05 and 1.8 times larger, respectively. Therefore,  
595 multiaxial anisotropy will produce  $0.5 < H_{cr}/H_K < 1$ . Magnetic minerals with uniaxial, cubic, and  
596 hexagonal anisotropy produce distinctive FORC diagram types (e.g., Egli, 2021; Roberts et al.,  
597 2021), which provides a useful way to evaluate the dominant anisotropy type before undertaking  
598 TFT analyses. Conventional and remanence FORC diagrams for the Inuyama red chert all have a  
599 central ridge up to 1.2 T. Although magnetite dominates the FORC signatures, hematite is  
600 responsible for central ridges with coercivities  $> 300$  mT. Ridge-type signatures for conventional  
601 and remanence FORC diagrams are explained as a manifestation of uniaxial SD magnetic behavior  
602 based on simulations (Harrison et al., 2019). However, instead of being shape dominated, as is the  
603 case for magnetite, ridge-type FORC signals for hematite nanoparticles reflect stress-induced  
604 uniaxial anisotropy that dominates the intrinsic magnetocrystalline anisotropy (Roberts et al.,  
605 2021). This magnetostrictive anisotropy associated with uniaxial internal stress controls the  
606 coercivity of hematite, which is consistent with the rapid  $H_{cr}$  increase at low temperatures (Figure  
607 5) that is usually enhanced in nanoparticles (Muench et al., 1985; Bruzzone and Ingalls, 1983).  
608 Therefore, considering the ridge-type signals observed in both conventional and remanence FORC  
609 diagrams for the red chert (see Figure 2 and 3 in Hu et al. (2021)) and  $H_{cr}$  variation with  
610 temperature, we predict that uniaxial anisotropy dominates pigmentary hematite in red chert and  
611 adopt  $H_{cr}/H_K = 0.524$ . Increased  $H_{cr}/H_K$  will result in decreased microcoercivity, increased  $T_B$   
612 estimates, and slightly decreased grain size estimates. Thus, when considering variations in the  
613 dominant anisotropy type, our calculations at least provide an upper limit of microcoercivity and  
614 grain size and a lower  $T_B$  limit.

615

## 616 **6. Conclusions**

617 Reconstructions of particle microcoercivity and volume distributions were performed with the  
618 method of Jackson et al. (2006) for SP/SSD hematite assemblages assuming a dominant uniaxial

619 anisotropy. The median temperature variation of  $H_{cr}$  for pigmentary hematite in Triassic/Jurassic  
620 red chert over eight temperatures from 300 K to 10 K follows a modified Kneller's law;  
621  $H_{cr}(T) = H_{cr0} \left( 1 - \left( \frac{T}{T_B} \right)^{0.24} \right)$ . The coercivity of hematite increases more rapidly than for  
622 magnetite with decreasing temperature, and coercivity distribution overlap between the two  
623 minerals starts to disappear below 100 K. Microcoercivity distributions that are nearly symmetric  
624 in logarithmic space vary from 1 T to ~10 T in Triassic red chert and from ~3 T to 30 T in  
625 Jurassic red chert. Both Triassic and Jurassic red chert have wide hematite grain size  
626 distributions. Most of the Triassic hematite ranges between ~35 nm to ~160 nm in diameter  
627 while the Jurassic red chert has a coarser hematite particles fraction similar to the Triassic  
628 hematite and a finer hematite fraction with grain size from a few nanometers to ~35 nm in  
629 diameter. Calculated median  $T_B$  varies from ~194 °C to 529 °C for red chert samples and  $T_B$   
630 contours indicate that most of the Triassic hematite is in the SSD state with a significant SP  
631 particle content with  $T_B < 300$  K. The SP/SSD threshold size for pigmentary hematite in Jurassic  
632 red chert is estimated to be 8-18 nm. Considering the low and broad  $T_B$  distribution in the  
633 Inuyama red chert, we propose that pigmentary hematite has a significant contribution to a  
634 secondary early Cenozoic thermoviscous magnetization rather than magnetite (Component B  
635 defined by Oda and Suzuki (2000)).

636

637 Our work demonstrates that the main features of SP/SSD hematite  $f(V, H_{k0})$  distributions can be  
638 recovered using the TFT technique, although details should be interpreted judiciously. Smearing  
639 of results due to low measurement resolution, artifacts, and variations in dominant anisotropy of  
640 hematite should be considered on a case-by-case basis. Ridge-like FORC signatures for red chert  
641 are interpreted here to indicate a dominant uniaxial anisotropy. If multiaxial anisotropy is instead  
642 dominant in hematite samples (e.g., Roberts et al., 2021), this would increase  $T_B$  estimates and  
643 decrease microcoercivity and grain size estimates.

644

#### 645 **Data Availability Statement**

646 All low-temperature magnetic data used here will be uploaded to the Magnetic Information  
647 Consortium rock magnetic portal (MagIC; [www.earthref.org](http://www.earthref.org)).

648

649

650 **Acknowledgments**

651 We thank Mike Jackson for providing the original TFT code. This work was supported by the  
 652 National Institute of Advanced Industrial Science and Technology, Ministry of Economy, Trade  
 653 and Industry, Japan, and the Australian Research Council through grants DP160100805 and  
 654 DP200100765.

655

656

657 **Appendix A**

658 Bayesian regression was performed using the PyMC3 Python package (Salvatier et al., 2016).

659 The parameterizations of the Bayesian prior distributions for  $H_{cr0}$ ,  $T_B$ ,  $\alpha$  and fitting error  $\sigma$  are  
 660 provided below.

661 **1.  $H_{cr0}$**

662 The prior for  $\mu_0 H_{cr0}$  follows a log normal distribution with median value of 0 and variance of  
 663 1. Thus, the probability density function can be expressed as:

664

$$665 \quad p(\mu_0 H_{cr0}) = \frac{1}{\mu_0 H_{cr0} \sqrt{2\pi}} \exp\left(-\frac{\ln(\mu_0 H_{cr0})^2}{2}\right) \quad (A1)$$

666

667

668

669 **2.  $T_B$**

670 Theoretically,  $T_B$  can vary between 0 and 960 K for hematite. For better calculation efficiency,  
 671 we set all variable values between 0 and 1 in the Bayesian regression. Therefore, instead of  $T_B$ , we  
 672 use  $T_B/1000$  to follow a Beta distribution with  $\alpha = 2$  and  $\beta = 2$ , the probability density function can  
 673 be expressed as:

$$674 \quad p\left(\frac{T_B}{1000}\right) = \frac{\frac{T_B}{1000} \times \left(1 - \frac{T_B}{1000}\right)}{B(2,2)}; \text{ and} \quad (A2)$$

675

676

$$677 \quad B(2,2) = \frac{\Gamma(2)\Gamma(2)}{\Gamma(4)} \quad (A3)$$

678

679 Where  $\Gamma$  is the Gamma function.

680

681 **3.  $\alpha$  and  $n$**

682  $\alpha$  and  $n$  follow a Beta distribution with  $\alpha = 8$  and  $\beta = 8$ , the probability density function can be  
 683 expressed as:

$$684 \quad p(\alpha) = \frac{\alpha^7 \times (1 - \alpha)^7}{B(8,8)} \text{ or } p\left(\frac{n}{50}\right) = \frac{\left(\frac{n}{50}\right)^7 \times \left(1 - \left(\frac{n}{50}\right)\right)^7}{B(8,8)}, \text{ with} \quad (A4, A5)$$

685  
 686

$$687 \quad B(8,8) = \frac{\Gamma(8)\Gamma(8)}{\Gamma(16)} \quad (A6)$$

688

689 Based on previous studies,  $n$  rarely exceeds the value of 50. Therefore, we normalized  $n$  by 50  
 690 for it to vary from 0 to 1.  $\Gamma$  in equation (A6) is the Gamma function.

691

#### 692 **4. Fitting error $\sigma$**

693  $\sigma$  follows a half-Cauchy distribution with location parameter of 0 and scale parameter of 1.  
 694 The probability density function can be expressed as:

$$695 \quad f(\sigma, 1) = \frac{2}{\pi(1 + \sigma)} \quad (A7)$$

696  
 697

698 The, no U-Turn Sampler (NUTS) from the Python Pymc3 package was used for sampling, in  
 699 where we set both the sampling number and iteration number to 4000.

700

701 Statistical results of Bayesian regression using equation (3) and equation (4), respectively are  
 702 listed. Two hundreds regression curves for each sample are shown in Figure 5. In the following  
 703 tables, hdi\_3% and hdi\_97% are the lower and upper bounds of the 97% high density interval.  
 704  $R_{\hat{}}$  is the Gelman-Rubin convergence statistic, where a value of 1 indicates that the chains have  
 705 converged.

706

707

708

709

710

711

712

713

714 Table A1 Posterior statistics of Bayesian regression of equation (3)

715

	Median	Standard deviation	hdi_3% <sup>1</sup>	hdi_97% <sup>2</sup>	R_hat <sup>3</sup>
n	28.650	3.700	21.650	35.600	1
$\mu_0 H_{cr0}$ (T) (KA1-1B-1)	1.402	0.137	1.133	1.649	1
$\mu_0 H_{cr0}$ (T) (UN2-9B-1)	1.424	0.139	1.166	1.682	1
$\mu_0 H_{cr0}$ (T) (KA6-9B-1)	1.581	0.145	1.308	1.853	1
$\mu_0 H_{cr0}$ (T) (KA6-2L-B-1)	1.645	0.145	1.371	1.916	1
$\sigma$	0.253	0.037	0.189	0.321	1

716

717 Table A2 Posterior statistics of Bayesian regression of equation (4)

718

719

720

721

722

723

724

725

726

727

728

729

730

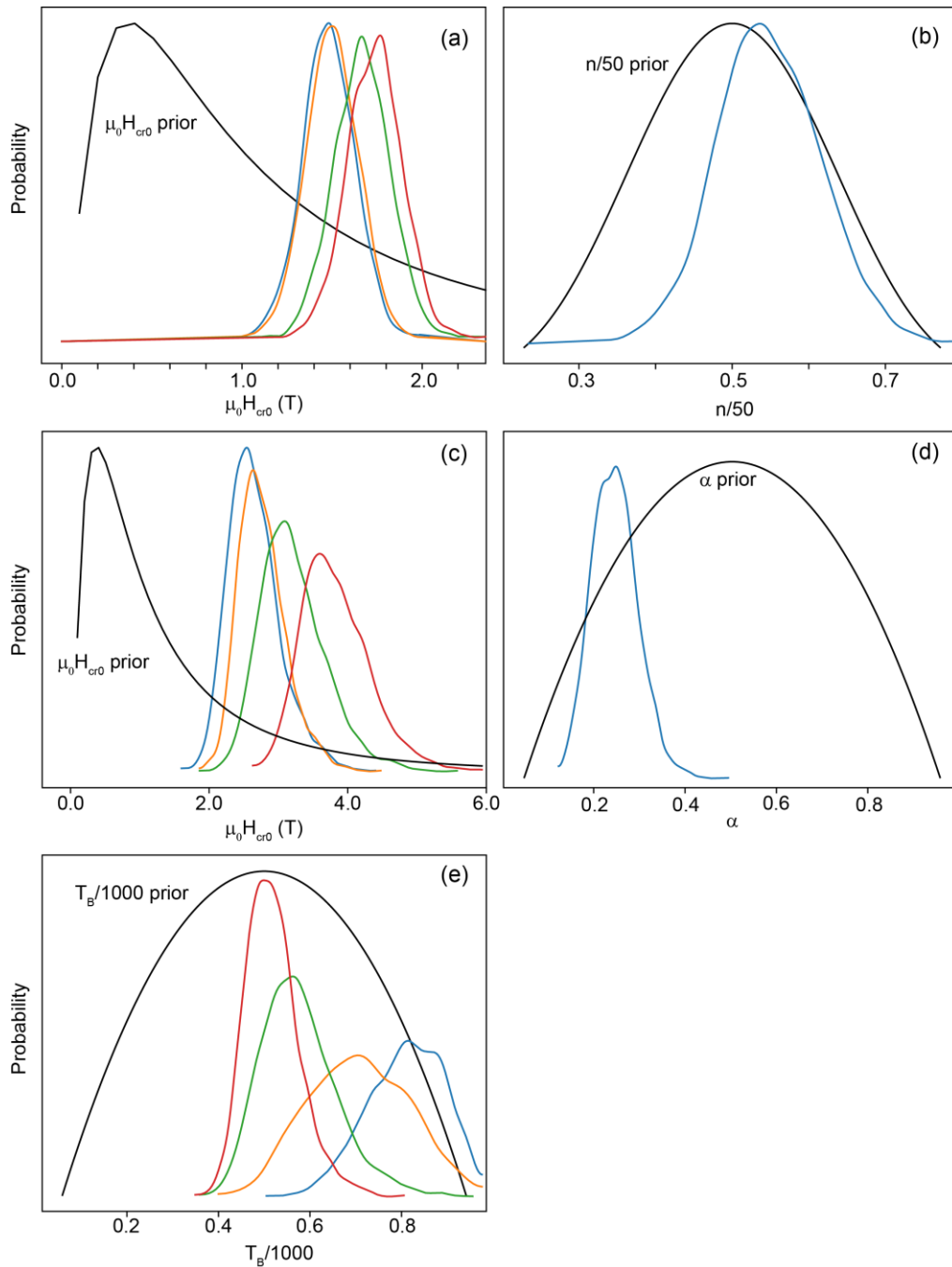
731

732

	mean	Standard deviation	hdi_3% <sup>1</sup>	hdi_97% <sup>2</sup>	R_hat <sup>3</sup>
$\alpha$	0.240	0.052	0.151	0.339	1
$\mu_0 H_{cr0}$ (T) (KA1-1B-1)	2.500	0.383	1.829	3.211	1
$\mu_0 H_{cr0}$ (T) (UN2-9B-1)	2.667	0.405	1.947	3.446	1
$\mu_0 H_{cr0}$ (T) (KA6-9B-1)	3.246	0.494	2.335	4.164	1
$\mu_0 H_{cr0}$ (T) (KA6-2L-B-1)	3.648	0.561	2.627	4.664	1
$T_B/100$ (K) (KA1-1B-1)	0.803	0.099	0.621	0.972	1
$T_B/1000$ (K) (UN2-9B-1)	0.717	0.103	0.534	0.919	1
$T_B/1000$ (K) (KA6-9B-1)	0.558	0.076	0.425	0.701	1
$T_B/1000$ (K) (KA6-2L-B-1)	0.467	0.054	0.370	0.567	1
$\sigma$	0.111	0.019	0.078	0.148	1

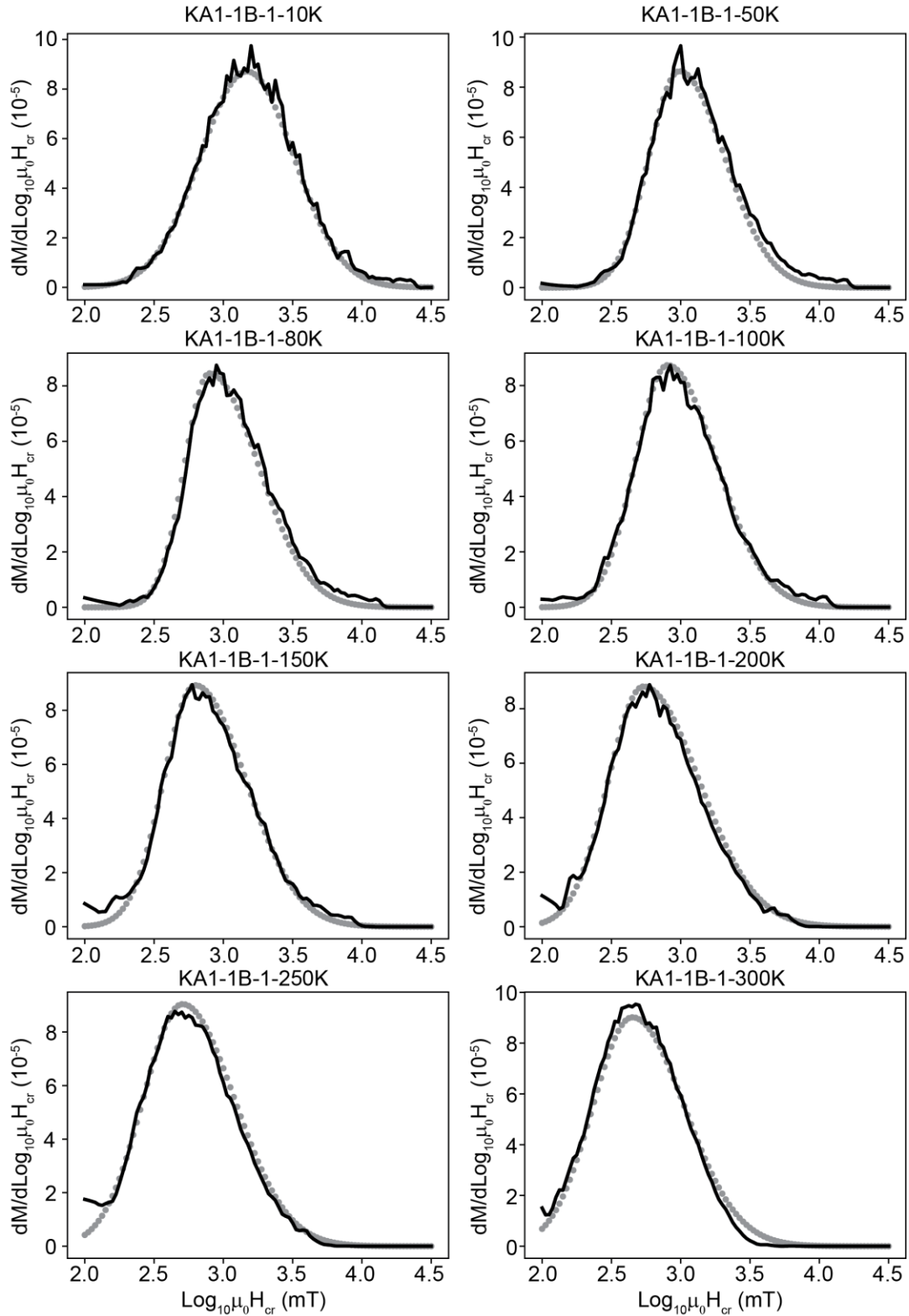
<sup>1</sup> hdi\_3% represents the lower bounds of the 97% high density interval of the corresponding posterior distribution.<sup>2</sup> hdi\_97% represents the upper bounds of the 97% high density interval of the corresponding posterior distribution<sup>3</sup> R\_hat is the Gelman-Rubin convergence statistic, which estimates the degree of convergence of a random Markov Chain. Values close to one indicate convergence to the underlying distribution.

733



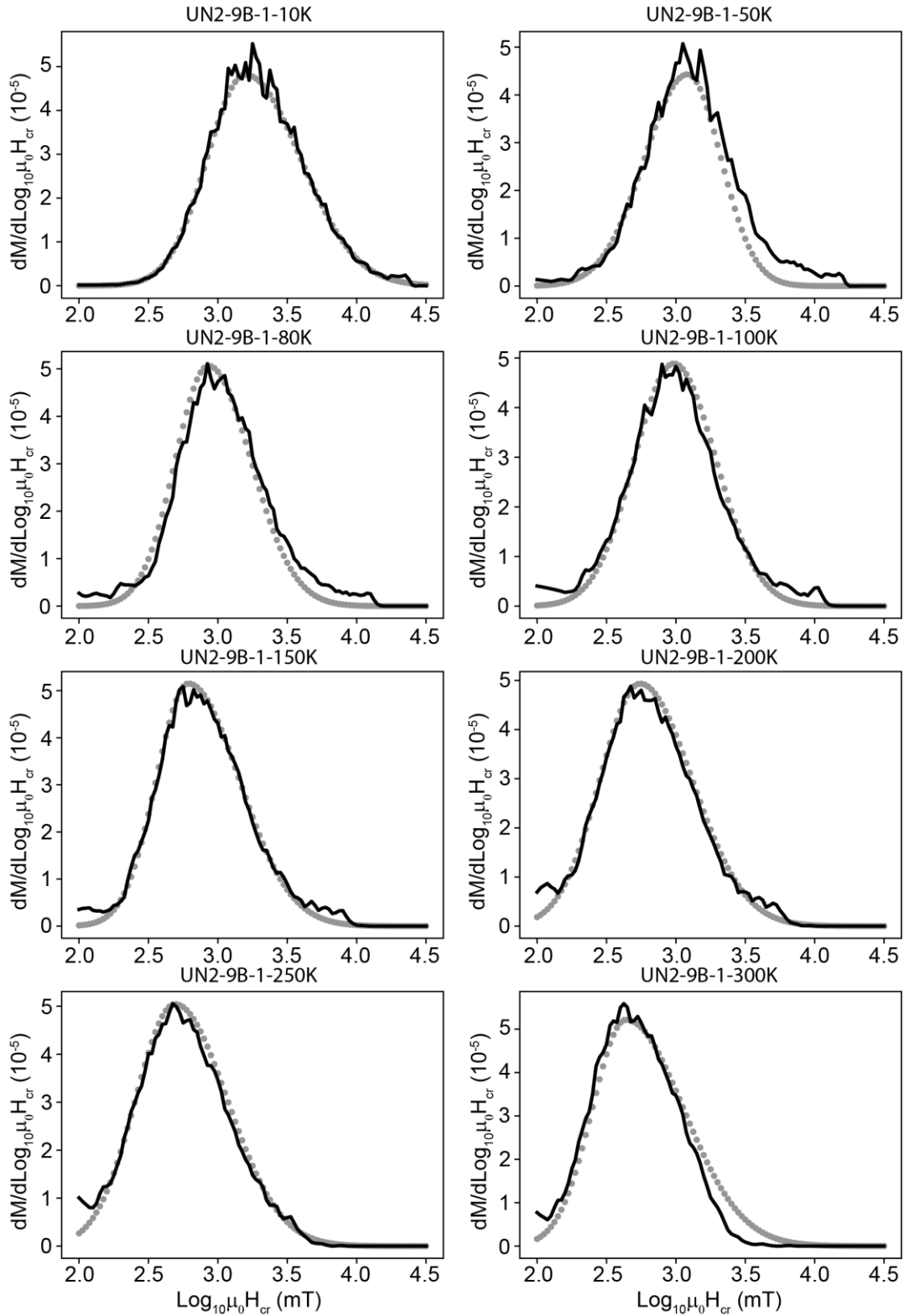
734

735 **Figure A1** The prior distribution (black lines) and posterior distribution (colored lines) of  
 736 parameters in the Bayesian model for (a-b) equation (3) and (c-e) equation (4). Blue, orange, green,  
 737 and red lines represent corresponding parameters for sample KA1-1B-1, UN2-9B-1, KA6-9B-1  
 738 and KA6-2L-B-1, respectively.



739

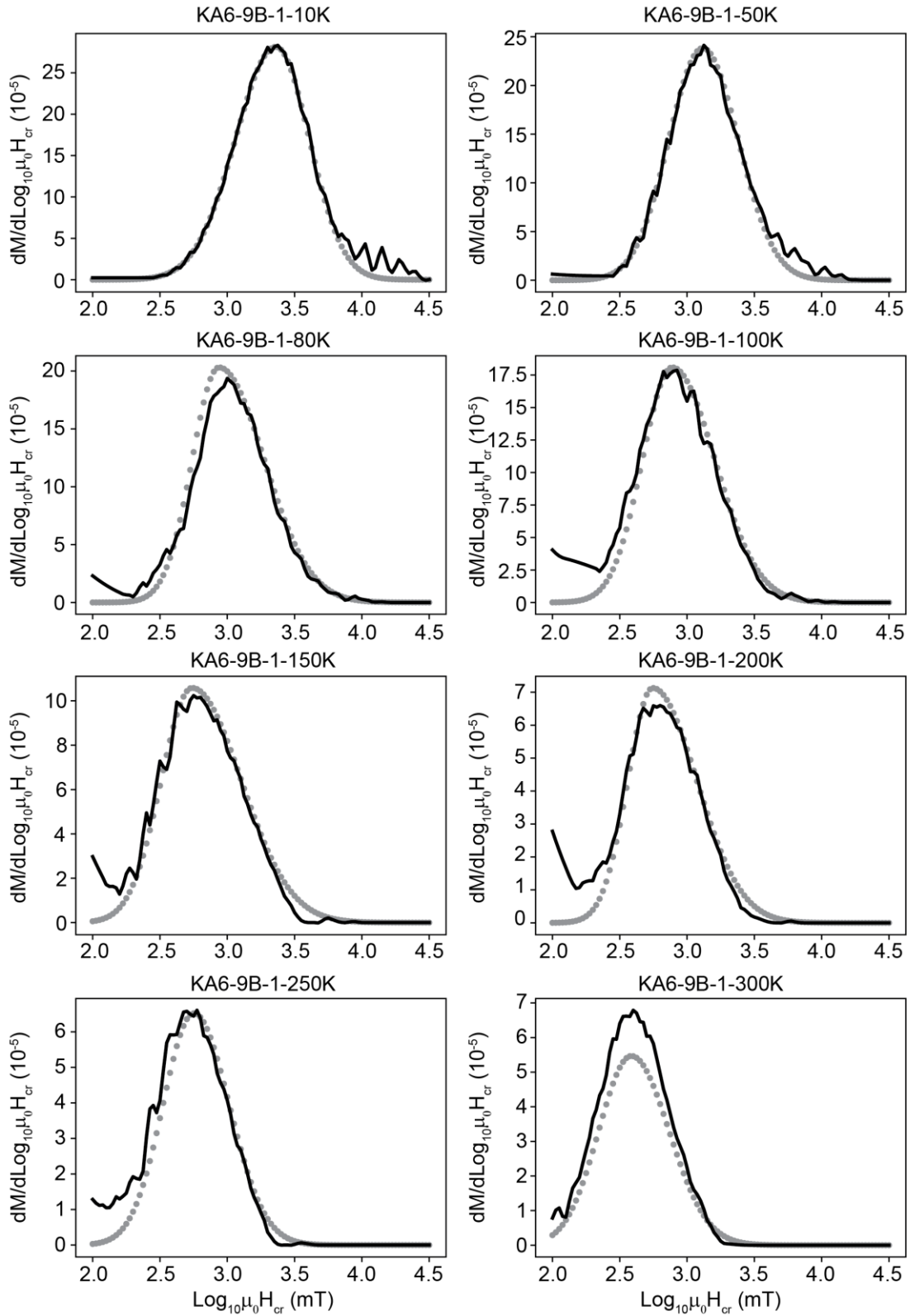
740 **Figure A2** Reconstructed (black solid lines) and measured backfield remanence curve derivatives  
 741 (gray dots) for Triassic sample KA1-1B-1.



742

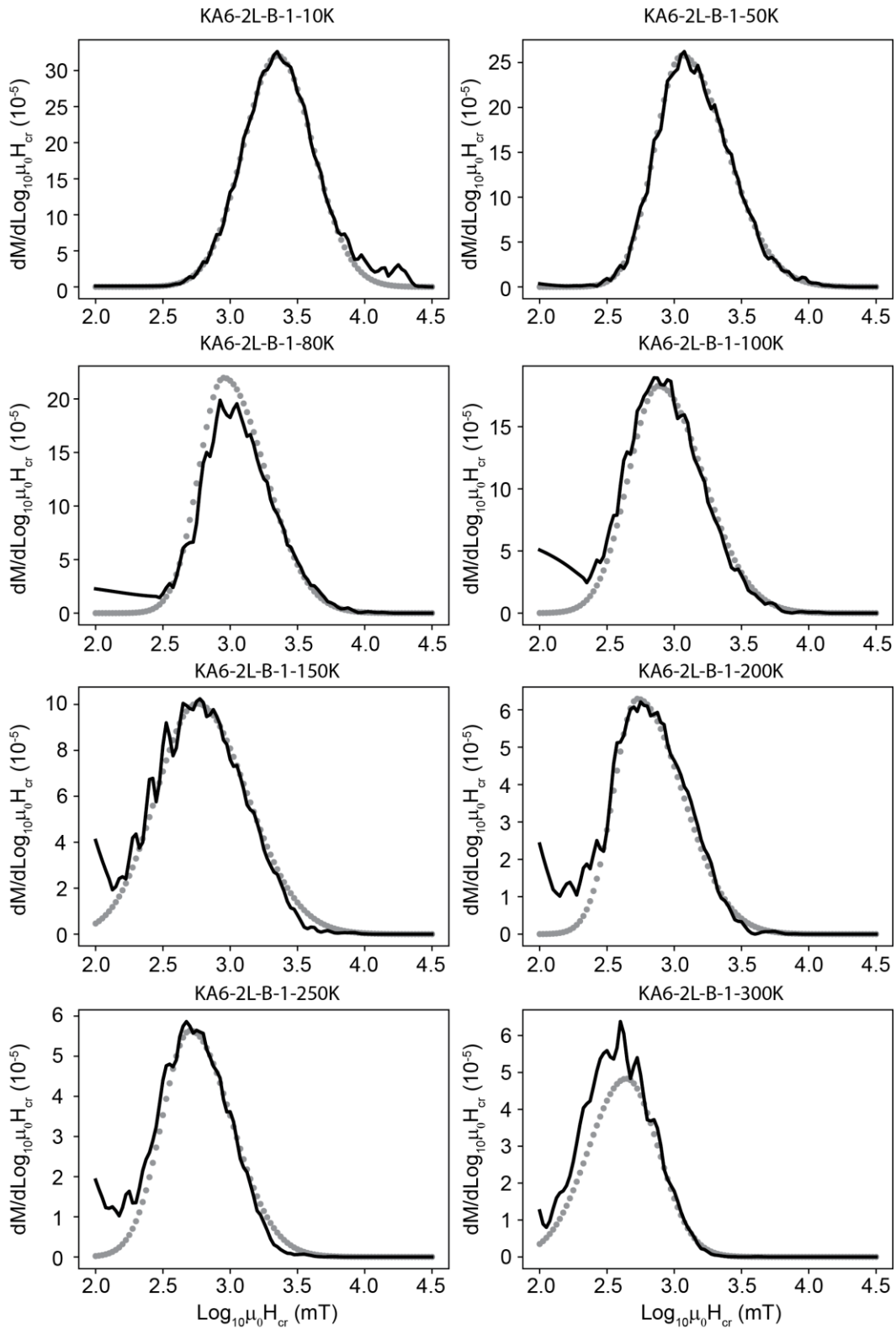
743 **Figure A3** Reconstructed (black solid lines) and measured backfield remanence curve derivatives

744 (gray dots) for Triassic sample UN2-9B-1.



745

746 **Figure A4** Reconstructed (black solid lines) and measured backfield remanence curve derivatives  
 747 (gray dots) for Jurassic sample KA6-9B-1.



748

749 **Figure A5** Reconstructed (black solid lines) and measured backfield remanence curve derivatives

750 (gray dots) for Jurassic sample KA6-2L-B-1.

751 **References**

- 752 Abrajvitch, A., R. S. Hori, & K. Kodama (2011), Magnetization carriers and remagnetization of bedded  
 753 chert, *Earth and Planetary Science Letters*, 305(1-2), 135-142.
- 754 Abrajvitch, A., R. S. Hori, & K. Kodama (2013), Rock magnetic record of the Triassic-Jurassic transition  
 755 in pelagic bedded chert of the Inuyama section, Japan, *Geology*, 41(7), 803-806.
- 756 Abrajvitch, A., B. J. Pillans, A. P. Roberts, & K. Kodama (2018), Magnetic properties and paleomagnetism  
 757 of zebra rock, western Australia: Chemical remanence acquisition in hematite pigment and ediacaran  
 758 geomagnetic field behavior, *Geochemistry Geophysics Geosystems*, 19(3), 732-748.
- 759 Banerjee, S. K. (1963), An attempt to observe basal plane anisotropy of hematite, *Philosophical Magazine*,  
 760 8(96), 2119-2120, doi:10.1080/14786436308209106.
- 761 Banerjee, S. K. (1971), New grain size limits for palaeomagnetic stability in haematite, *Nature-Physical  
 762 Science*, 232(27), 15-&, doi:10.1038/physci232015a0.
- 763 Beck, M. E., R. F. Burmester, & B. A. Housen (2003), The red bed controversy revisited: shape analysis of  
 764 Colorado Plateau units suggests long magnetization times, *Tectonophysics*, 362(1), 335-344,  
 765 doi:10.1016/S0040-1951(02)00644-3.
- 766 Bilardello, D., & K. P. Kodama (2010a), Palaeomagnetism and magnetic anisotropy of Carboniferous red  
 767 beds from the Maritime Provinces of Canada: evidence for shallow palaeomagnetic inclinations and  
 768 implications for North American apparent polar wander, *Geophysical Journal International*, 180(3),  
 769 1013-1029, doi:10.1111/j.1365-246X.2009.04457.x.
- 770 Bilardello, D., & K. P. Kodama (2010b), Rock magnetic evidence for inclination shallowing in the early  
 771 Carboniferous Deer Lake Group red beds of western Newfoundland, *Geophysical Journal International*,  
 772 181(1), 275-289, doi:10.1111/j.1365-246X.2010.04537.x.
- 773 Bloch, F. (1930), Zur Theorie des Ferromagnetismus, *Zeitschrift für Physik*, 61(3), 206-219,  
 774 doi:10.1007/BF01339661.
- 775 Bruzzone, C. L., & R. Ingalls (1983), Mossbauer-effect study of the morin transition and atomic positions  
 776 in hematite under pressure, *Physical Review B*, 28(5), 2430-2440, doi:10.1103/PhysRevB.28.2430.
- 777 Butler, R. (1992), *Paleomagnetism: Magnetic domains to geologic terranes*, Blackwell Scientific  
 778 Publications, Boston.
- 779 Collinson, D. W. (1969), Investigations into stable remanent magnetization of sediments, *Geophysical  
 780 Journal of the Royal Astronomical Society*, 18(2), 211-222, doi:10.1111/j.1365-246X.1969.tb03563.x.
- 781 Cornell, R. M., & U. Schwertmann (2004), *The Iron Oxides: Structure, Properties, Reactions, Occurrences  
 782 and Uses*, 664 pp., Wiley-VCH Verlag GmbH & Co. KGaA, doi:10.1002/3527602097.
- 783 Dekkers, M. J. (1990), Magnetic-properties of natural goethite. 3. Magnetic-behavior and properties of  
 784 minerals originating from goethite dehydration during thermal demagnetization, *Geophysical Journal  
 785 International*, 103(1), 233-250, doi:10.1111/j.1365-246X.1990.tb01765.x.
- 786 Dunlop, D. J. (1965), Grain distributions in rocks containing single domain grains, *Journal of  
 787 Geomagnetism and Geoelectricity*, 17(3-4), 459-&, doi:10.5636/jgg.17.459.
- 788 Dunlop, D. J., & Ö. Özdemir (2000), Effect of grain size and domain state on thermal demagnetization tails,  
 789 *Geophysical Research Letters*, 27(9), 1311-1314, doi: 10.1029/1999GL008461.
- 790 Dunlop, D. J., Ö. Özdemir, D. A. Clark, & P. W. Schmidt (2000), Time-temperature relations for the  
 791 remagnetization of pyrrhotite (Fe<sub>7</sub>S<sub>8</sub>) and their use in estimating paleotemperatures, *Earth and Planetary  
 792 Science Letters*, 176(1), 107-116, doi:10.1016/S0012-821X(99)00309-X.
- 793 Egglseider, M. S., A. R. Cruden, A. G. Tomkins, S. A. Wilson, & A. D. Langendam (2018), Colloidal origin  
 794 of microbands in banded iron formations, *Geochemical Perspectives Letters*, 6, 43-49,  
 795 doi:10.7185/geochemlet.1808.
- 796 Egli, R. (2021), Magnetic Characterization of Geologic Materials with First-Order Reversal Curves, in  
 797 *Magnetic Measurement Techniques for Materials Characterization*, edited by V. Franco and B. Dodrill,  
 798 pp. 455-604, Springer International Publishing, Cham, doi:10.1007/978-3-030-70443-8\_17.
- 799 Egli, R., A. P. Chen, M. Winklhofer, K. P. Kodama, & C.-S. Horng (2010), Detection of noninteracting  
 800 single domain particles using first-order reversal curve diagrams, *Geochemistry, Geophysics,  
 801 Geosystems*, 11(1), doi:10.1029/2009gc002916.

- 802 Frank, U., & N. R. Nowaczyk (2008), Mineral magnetic properties of artificial samples systematically  
 803 mixed from haematite and magnetite, *Geophysical Journal International*, *175*(2), 449-461.
- 804 Guyodo, Y., A. Mostrom, R. L. Penn, & S. K. Banerjee (2003), From nanodots to nanorods: oriented  
 805 aggregation and magnetic evolution of nanocrystalline goethite, *Geophysical Research Letters*, *30*(10),  
 806 doi:10.1029/2003gl017021.
- 807 Harrison, R. J., X. Zhao, P. Hu, T. Sato, D. Heslop, A. R. Muxworthy, H. Oda, V. S. C. Kuppili, & A. P.  
 808 Roberts (2019), Simulation of remanent, transient, and induced FORC diagrams for interacting particles  
 809 with uniaxial, cubic, and hexagonal anisotropy, *Journal of Geophysical Research: Solid Earth*, *124*(12),  
 810 12404-12429, doi:10.1029/2019JB018050.
- 811 Hendriksen, P. V., S. Linderoth, & P. A. Lindgard (1993), Finite-size modifications of the magnetic-  
 812 properties of clusters, *Physical Review B*, *48*(10), 7259-7273, doi:10.1103/PhysRevB.48.7259.
- 813 Hu, P. X., H. Oda, X. Zhao, R. J. Harrison, D. Heslop, T. Sato, A. R. Muxworthy, & A. P. Roberts (2021),  
 814 Assessment of magnetic techniques for understanding complex mixtures of magnetite and hematite: The  
 815 Inuyama red chert, *Journal of Geophysical Research-Solid Earth*, *126*(1), doi:10.1029/2020JB019518.
- 816 Huang, W., M. J. Jackson, M. J. Dekkers, P. Solheid, B. Zhang, Z. Guo, & L. Ding (2019), Nanogoethite  
 817 as a potential indicator of remagnetization in red beds, *Geophysical Research Letters*, *46*(22), 12841-  
 818 12850, doi:10.1029/2019GL084715.
- 819 Hyodo, M., T. Sano, M. Matsumoto, Y. Seto, B. Bradák, K. Suzuki, J.-i. Fukuda, M. Shi, & T. Yang (2020),  
 820 Nanosized authigenic magnetite and hematite particles in mature-paleosol phyllosilicates: New evidence  
 821 for a magnetic enhancement mechanism in loess sequences of China, *Journal of Geophysical Research:*  
 822 *Solid Earth*, *125*(3), e2019JB018705, doi:10.1029/2019JB018705.
- 823 Jackson, M., B. Carter-Stiglitz, R. Egli, & P. Solheid (2006), Characterizing the superparamagnetic grain  
 824 distribution  $f(V, H_k)$  by thermal fluctuation tomography, *Journal of Geophysical Research: Solid Earth*,  
 825 *111*(B12), doi:10.1029/2006jb004514.
- 826 Jacobsen, H. (2014), *Magnetic properties of nano-scale hematite: theory, experiments and simulations*,  
 827 University of Copenhagen.
- 828 Jiang, Z., Q. Liu, A. P. Roberts, M. J. Dekkers, V. Barrón, J. Torrent, & S. Li (2022), The magnetic and  
 829 color reflectance properties of hematite: from Earth to Mars, *Reviews of Geophysics*, *60*(1),  
 830 e2020RG000698, doi:10.1029/2020RG000698.
- 831 Jiang, Z. X., Q. S. Liu, M. J. Dekkers, V. Barron, J. Torrent, & A. P. Roberts (2016), Control of Earth-like  
 832 magnetic fields on the transformation of ferrihydrite to hematite and goethite, *Scientific Reports*, *6*,  
 833 doi:10.1038/srep30395.
- 834 Jiang, Z. X., Q. S. Liu, M. J. Dekkers, C. Colombo, Y. J. Yu, V. Barron, & J. Torrent (2014), Ferro and  
 835 antiferromagnetism of ultrafine-grained hematite, *Geochemistry Geophysics Geosystems*, *15*(6), 2699-  
 836 2712, doi:10.1002/2014gc005377.
- 837 Jiang, Z. X., Q. S. Liu, M. J. Dekkers, X. Zhao, A. P. Roberts, Z. Y. Yang, C. S. Jin, & J. X. Liu (2017),  
 838 Remagnetization mechanisms in Triassic red beds from South China, *Earth and Planetary Science*  
 839 *Letters*, *479*, 219-230.
- 840 Jones, D. L., & B. Murchey (1986), Geologic significance of paleozoic and mesozoic radiolarian chert,  
 841 *Annual Review of Earth and Planetary Sciences*, *14*, 455-492.
- 842 Kletetschka, G., & P. J. Wasilewski (2002), Grain size limit for SD hematite, *Physics of the Earth and*  
 843 *Planetary Interiors*, *129*(1), 173-179, doi: 10.1016/S0031-9201(01)00271-0.
- 844 Kneller, E. F., & F. E. Luborsky (1963), Particle size dependence of coercivity and remanence of single-  
 845 domain particles, *Journal of Applied Physics*, *34*(3), 656-658, doi:10.1063/1.1729324.
- 846 Lagroix, F., & Y. Guyodo (2017), A new tool for separating the magnetic mineralogy of complex mineral  
 847 assemblages from low temperature magnetic behavior, *Frontiers in Earth Science*, *5*(61),  
 848 doi:10.3389/feart.2017.00061.
- 849 Larrasoaña, J. C., A. P. Roberts, E. J. Rohling, M. Winklhofer, & R. Wehausen (2003), Three million years  
 850 of monsoon variability over the northern Sahara, *Climate Dynamics*, *21*(7), 689-698,  
 851 doi:10.1007/s00382-003-0355-z.

- 852 Lepre, C. J., & P. E. Olsen (2021), Hematite reconstruction of Late Triassic hydroclimate over the Colorado  
 853 Plateau, *Proceedings of the National Academy of Sciences*, 118(7), e2004343118,  
 854 doi:10.1073/pnas.2004343118.
- 855 Liu, Q., V. Barrón, J. Torrent, H. Qin, & Y. Yu (2010), The magnetism of micro-sized hematite explained,  
 856 *Physics of the Earth and Planetary Interiors*, 183(3), 387-397, doi:10.1016/j.pepi.2010.08.008.
- 857 Liu, Q. S., J. Bloemendal, J. Torrent, & C. L. Deng (2006), Contrasting behavior of hematite and goethite  
 858 within paleosol S5 of the Luochuan profile, Chinese Loess Plateau, *Geophysical Research Letters*,  
 859 33(20), doi:10.1029/2006gl027172.
- 860 Maaz, K., A. Mumtaz, S. K. Hasanain, & M. F. Bertino (2010), Temperature dependent coercivity and  
 861 magnetization of nickel ferrite nanoparticles, *Journal of Magnetism and Magnetic Materials*, 322(15),  
 862 2199-2202, doi:10.1016/j.jmmm.2010.02.010.
- 863 Martin-Hernandez, F., & S. Guerrero-Suárez (2012), Magnetic anisotropy of hematite natural crystals: high  
 864 field experiments, *International Journal of Earth Sciences*, 101(3), 637-647, doi:10.1007/s00531-011-  
 865 0665-z.
- 866 Martinez, B., A. Roig, X. Obradors, E. Molins, A. Rouanet, & C. Monty (1996), Magnetic properties of  
 867 gamma-Fe<sub>2</sub>O<sub>3</sub> nanoparticles obtained by vaporization condensation in a solar furnace, *Journal of*  
 868 *Applied Physics*, 79(5), 2580-2586, doi:10.1063/1.361125.
- 869 Matsuo, M., K. Kubo, & Y. Isozaki (2003), Moessbauer spectroscopic study on characterization of iron in  
 870 the Permian to Triassic deep-sea chert from Japan, *Hyperfine Interactions*, 5, 435-438.
- 871 Maxbauer, D. P., J. M. Feinberg, & D. L. Fox (2016), MAX UnMix: A web application for unmixing  
 872 magnetic coercivity distributions, *Computers & Geosciences*, 95, 140-145, doi:  
 873 10.1016/j.cageo.2016.07.009.
- 874 Menyeh, A., & W. O'Reilly (1995), The coercive force of fine particles of monoclinic pyrrhotite (Fe<sub>7</sub>S<sub>8</sub>)  
 875 studied at elevated temperature, *Physics of the Earth and Planetary Interiors*, 89(1), 51-62, doi:  
 876 10.1016/0031-9201(94)02999-R.
- 877 Muench, G. J., S. Araj, & E. Matijevic (1985), The Morin transition in small Alpha-Fe<sub>2</sub>O<sub>3</sub> particles,  
 878 *Physica Status Solidi a-Applied Research*, 92(1), 187-192, doi:DOI 10.1002/pssa.2210920117.
- 879 Néel, L. (1949), Théorie du traînage magnétique des ferromagnétiques en grains fins avec application aux  
 880 terres cuites, *Annales de Geophysique*, 5, 99--136.
- 881 Oda, H., & H. Suzuki (2000), Paleomagnetism of Triassic and Jurassic red bedded chert of the Inuyama  
 882 area, central Japan, *Journal of Geophysical Research-Solid Earth*, 105(B11), 25743-25767.
- 883 Özdemir, O., & D. J. Dunlop (2014), Hysteresis and coercivity of hematite, *Journal of Geophysical*  
 884 *Research-Solid Earth*, 119(4), 2582-2594, doi:10.1002/2013jb010739.
- 885 Özdemir, Ö., & D. J. Dunlop (2002), Thermoremanence and stable memory of single-domain hematites,  
 886 *Geophysical Research Letters*, 29(18), 24-21-24-24, doi: 10.1029/2002GL015597.
- 887 Peters, C., & M. J. Dekkers (2003), Selected room temperature magnetic parameters as a function of  
 888 mineralogy, concentration and grain size, *Physics and Chemistry of the Earth, Parts A/B/C*, 28(16), 659-  
 889 667, doi:10.1016/S1474-7065(03)00120-7.
- 890 Roberts, A. P., X. Zhao, D. Heslop, A. Abrajevitch, Y.H. Chen, P. Hu, Z. Jiang, Q. Liu, & B. J. Pillans  
 891 (2020), Hematite ( $\alpha$ -Fe<sub>2</sub>O<sub>3</sub>) quantification in sedimentary magnetism: limitations of existing proxies  
 892 and ways forward, *Geoscience Letters*, 7(1), 8, doi:10.1186/s40562-020-00157-5.
- 893 Roberts, A. P., X. Zhao, P. Hu, A. Abrajevitch, Y. Chen, R. Harrison, D. Heslop, Z. Jiang, J. Li, Q. Liu, A.  
 894 R. Muxworthy, H. Oda, H. St. C. O'Neill, B. J. Pillans & T. Sato (2021), Magnetic domain state and  
 895 anisotropy in hematite ( $\alpha$ -Fe<sub>2</sub>O<sub>3</sub>) from first-order reversal curve diagrams, *Journal of Geophysical*  
 896 *Research: Solid Earth*, 126(12), e2021JB023027, doi:10.1029/2021JB023027.
- 897 Salvatier, J., T. V. Wiecki, & C. Fonnesbeck (2016), Probabilistic programming in Python using PyMC3,  
 898 *PeerJ Computer Science*, doi:ARTNe5510.7717/peerj-cs.55.
- 899 Satheesh, M., A. R. Paloly, C. K. Krishna Sagar, K. G. Suresh, & M. J. Bushiri (2018), Improved coercivity  
 900 of solvothermally grown hematite ( $\alpha$ -Fe<sub>2</sub>O<sub>3</sub>) and hematite/graphene oxide nanocomposites ( $\alpha$ -Fe<sub>2</sub>O<sub>3</sub>/GO)  
 901 at low temperature, *physica status solidi (a)*, 215(2), 1700705, doi:10.1002/pssa.201700705.

- 902 Schwertmann, U. (1991), Solubility and dissolution of iron-oxides, *Plant and Soil*, 130(1-2), 1-25, doi:  
903 10.1007/Bf00011851.
- 904 Shibuya, H., & S. Sasajima (1986), Paleomagnetism of red cherts - a case-study in the Inuyama area, central  
905 Japan, *Journal of Geophysical Research-Solid Earth and Planets*, 91(B14), 14105-14116.
- 906 Stoner, E. C., & E. P. Wohlfarth (1948), A mechanism of magnetic hysteresis in heterogeneous alloys,  
907 *Philosophical Transactions of the Royal Society of London. Series A, Mathematical and Physical*  
908 *Sciences*, 240(826), 599-642, doi:10.1098/rsta.1948.0007.
- 909 Sun, S., K. O. Konhauser, A. Kappler, & Y.L. Li (2015), Primary hematite in Neoproterozoic to  
910 Paleoproterozoic oceans, *GSA Bulletin*, 127(5-6), 850-861, doi:10.1130/b31122.1.
- 911 Sunagawa, I. (1960), Growth history of hematite, *American Mineralogist*, 45(5-6), 566-575.
- 912 Sunagawa, I., & P. J. Flanders (1965), Structural and magnetic studies in hematite single crystals,  
913 *Philosophical Magazine*, 11(112), 747-&, doi:10.1080/14786436508230080.
- 914 Swanson-Hysell, N. L., L. M. Fairchild, & S. P. Slotznick (2019), Primary and secondary red bed  
915 magnetization constrained by fluvial intraclasts, *Journal of Geophysical Research: Solid Earth*, 124(5),  
916 4276-4289, doi:10.1029/2018jb017067.
- 917 Swanson-Hysell, N. L., J. M. Feinberg, T. S. Berquo, & A. C. Maloof (2011), Self-reversed magnetization  
918 held by martite in basalt flows from the 1.1-billion-year-old Keweenawan rift, Canada, *Earth and*  
919 *Planetary Science Letters*, 305(1-2), 171-184.
- 920 Tauxe, L., D. V. Kent, & N. D. Opdyke (1980), Magnetic components contributing to the NRM of middle  
921 Siwalik red beds, *Earth and Planetary Science Letters*, 47(2), 279-284, doi:10.1016/0012-  
922 821x(80)90044-8.
- 923 Van Der Voo, R., & T. H. Torsvik (2012), The history of remagnetization of sedimentary rocks: Deceptions,  
924 developments and discoveries, *371(1)*, 23-53.
- 925 Zhang, D. J., K. J. Klabunde, C. M. Sorensen, & G. C. Hadjipanayis (1998), Magnetization temperature  
926 dependence in iron nanoparticles, *Physical Review B*, 58(21), 14167-14170,  
927 doi:10.1103/PhysRevB.58.14167.

928

1 **Estimating particle size and coercivity distributions of pigmentary hematite in red**  
2 **chert with thermal fluctuation tomography**

3 **Pengxiang Hu<sup>1,2</sup>, Xiang Zhao<sup>1,2</sup>, David Heslop<sup>1,2</sup>, Hirokuni Oda<sup>2</sup>, Andrew P. Roberts<sup>1,2</sup>**  
4

5 <sup>1</sup> *Research School of Earth Sciences, Australian National University, Canberra, ACT 2601,*  
6 *Australia*

7 <sup>2</sup> *Research Institute of Geology and Geoinformation, Geological Survey of Japan, National*  
8 *Institute of Advanced Industrial Science and Technology (AIST), AIST Tsukuba Central 7, 1-1-*  
9 *1 Higashi, Tsukuba, Ibaraki, 305-8567, Japan*

10  
11 *Corresponding author: Pengxiang Hu ([pengxiang.hu@anu.edu.au](mailto:pengxiang.hu@anu.edu.au))*

12  
13 **Key Points:**

- 14 • Thermal fluctuation tomography is applied to red cherts to estimate grain size and  
15 microcoercivity distributions of pigmentary hematite
- 16 • Fine hematite particles (35 - 160 nm) occur in all samples including superparamagnetic  
17 hematite down to a few nanometers
- 18 • Temperature-dependent coercivity variations in pigmentary hematite follow Kneller's law  
19

20 **Plain language Summary**

21 Pigmentary hematite widely presents in rocks and sediment and is crucial for paleomagnetic and  
22 paleoenvironmental studies because they can record ancient earth magnetic field and past climate  
23 signals. As the most important properties in paleomagnetic and paleoenvironmental applications,  
24 the coercivity and grain size distribution of natural pigmentary hematite is poorly constrained  
25 due to the weak magnetism of hematite and the small size. In this study, we provide a strategy  
26 using low-temperature demagnetization curves for estimating joint particle volume and  
27 microcoercivity distribution of pigmentary hematite in Inuyama red chert samples. The hematite  
28 coercivity increases exponentially with decreasing temperature. Hematite microcoercivity  
29 without thermal fluctuation has a wide but approximately symmetric distribution in logarithmic

30 space from ~1 tesla to tens of tesla. The grain size of hematite varies from several nanometers to  
31 about 160 nm. The fine particle size of these hematite results in low unblocking temperature,  
32 which makes them suitable to record remagnetization in geological time.

33

## 34 **Abstract**

35 Pigmentary hematite carries important signals in paleomagnetic and paleoenvironmental studies.  
36 However, weak magnetism and the assumption that it has high magnetic coercivity prevents  
37 routine identification of the size distribution of pigmentary hematite, especially for fine particle  
38 sizes. We present a strategy for estimating joint hematite particle volume and microcoercivity ( $f$   
39 ( $V$ ,  $H_{k0}$ )) distributions from low-temperature demagnetization curves and thermal fluctuation  
40 tomography (TFT) of pigmentary hematite in bulk samples of Triassic-Jurassic Inuyama red chert,  
41 Japan. The coercivity of the pigmentary hematite increases exponentially with decreasing  
42 temperature, following a modified Kneller's law, where microcoercivity has a wide but  
43 approximately symmetric distribution in logarithmic space from ~1 tesla to tens of tesla. All of the  
44 red chert samples contain stable single domain (SSD) hematite with 35 - 160 nm diameter; a  
45 significant superparamagnetic (SP) hematite population with sizes down to several nanometers  
46 also occurs in Jurassic samples. The SP/SSD threshold size is estimated to be 8 - 18 nm in these  
47 samples. The fine particle size of the pigmentary hematite is evident in its low median unblocking  
48 temperature (194 °C to 529 °C) and, thus, this hematite may contribute to all four paleomagnetic  
49 components identified in published thermal magnetization studies of the Inuyama red chert. In this  
50 work, uniaxial anisotropy and magnetization switching via coherent rotation are assumed. Uniaxial  
51 anisotropy is often dominant in fine-grained hematite, although the dominant anisotropy type  
52 should be evaluated before using TFT. This approach is applicable to studies that require  
53 knowledge of coercivity and size distributions of hematite pigments.

54

## 55 **1. Introduction**

56 Hematite is abundant in sedimentary rocks, especially red beds. It occurs commonly as a fine-  
57 grained chemically precipitated pigment and as coarser detrital or specular hematite (Cornell and  
58 Schwertmann, 2003; Lepre and Olsen, 2021; Jiang et al., 2022; Swanson-Hysell et al., 2019; Tauxe

59 et al., 1980). Poorly crystalline pigmentary hematite can be the dominant iron oxide in many red  
60 soils and sediments and is responsible for their characteristic red color. Both specular and  
61 pigmentary hematite can carry magnetic remanence. Specular hematite carries a detrital remanent  
62 magnetization (DRM), which is often assumed to be a primary or near-primary magnetization.  
63 Widely observed red bed remagnetizations tend to be associated with late diagenetic pigmentary  
64 hematite formation. Debate about whether red beds record a primary DRM or a secondary  
65 chemical remanent magnetization (CRM) led to the “red bed controversy” (Beck et al., 2003;  
66 Butler, 1992; Van Der Voo & Torsvik, 2012). Identification of CRM acquisition in pigmentary  
67 hematite can enable more accurate paleomagnetic interpretations in regional tectonic studies  
68 (Abrajevitch et al., 2018; Jiang et al., 2017; Swanson-Hysell et al., 2019). As the most abundant  
69 surficial iron oxide on Earth resulting from near-surface processes, hematite is also an excellent  
70 recorder of paleoenvironmental signals. Its formation via authigenic chemical processes means  
71 that pigmentary hematite is used as an indicator of hydration conditions, acidity of aqueous  
72 environments, and monsoon evolution (e.g., Larrasoña et al., 2003; Abrajevitch et al., 2013; Lepre  
73 and Olsen, 2021). Despite the usefulness of pigmentary hematite as a paleoclimatic indicator or as  
74 a carrier of paleomagnetic records, it is often described vaguely as a “fine hematite population”,  
75 with poorly constrained coercivity and grain size distributions.

76  
77 Characterizing the grain size and coercivity of pigmentary hematite is challenging because it is  
78 necessary to overcome the combined difficulty of detecting weakly magnetic hematite when it co-  
79 occurs with other magnetic minerals and characterizing poorly crystalline nanoparticles. Magnetite  
80 has a spontaneous magnetization that is more than 200 times stronger than hematite, so even small  
81 amounts of magnetite can overwhelm the magnetic contribution of hematite (Dekkers, 1990; Frank  
82 and Nowaczyk, 2008; Roberts et al., 2020). In practice, hematite detection in natural samples often  
83 relies on its high coercivity and distinctive color (Roberts et al., 2020; Jiang et al., 2022 and  
84 references therein). However, the small size and often poorly crystalline nature of hematite  
85 nanoparticles means that hematite concentrations can be difficult to determine with many  
86 spectroscopic approaches. Such particles will also be responsible for a substantial low-coercivity  
87 distribution that is not usually attributed to hematite in mineral magnetic studies, especially when  
88 using magnetic parameters with cut-off fields of 300 mT (Roberts et al., 2020). Isothermal  
89 remanent magnetization (IRM) component analysis appears to be the most suitable magnetic

90 method for detecting hematite because it enables estimation of continuous, non-truncated  
91 coercivity distributions (Hu et al., 2021; Roberts et al., 2020). However, superparamagnetic (SP)  
92 pigmentary hematite, which is abundant in natural environments (Collinson, 1969; Schwertmann,  
93 1991), will not be evident in room temperature IRM results. Color and diffuse reflectance methods  
94 also have limitations for detecting or quantifying hematite because they depend strongly on grain  
95 size and crystallinity. Decreasing grain size tends to reduce the reflectance wavelength and  
96 changes the color from purple-red to yellow-red (Cornell and Schwertmann, 2003; Jiang et al.,  
97 2022). Evaluating grain size distributions for pigmentary hematite is, therefore, difficult because  
98 grain size influences most proxies used to estimate hematite properties.

99

100 Microscopy observations reveal the existence of nano-sized hematite with sizes from ~20 nm to a  
101 few hundred nanometers in soils and banded iron formations (Eggseder et al., 2018; Hyodo et al.,  
102 2020; Sun et al., 2015). A more systematic relationship between hematite grain size and  
103 unblocking temperature has been established by Swanson-Hysell et al. (2011, 2019) using Néel  
104 (1949) relaxation theory. The grain size range of remanence-carrying hematite can be inferred  
105 using unblocking temperatures from thermal demagnetization experiments, although this approach  
106 cannot be used to estimate SP particles because they do not carry a stable remanence at room  
107 temperature.

108

109 Grain volume is a key variable in Néel (1949) theory. Dunlop (1965) pointed out that it is possible  
110 to combine field- and temperature-dependent measurements to determine the joint grain volume  
111 ( $V$ ) and microcoercivity at absolute zero ( $H_{k0}$ ) distribution;  $f(V, H_{k0})$ . Jackson et al. (2006)  
112 developed a procedure to estimate  $f(V, H_{k0})$  for particle assemblages that contain both SP and  
113 stable single domain (SSD) magnetite based on backfield remanence curves measured over a range  
114 of temperatures, which they called “thermal fluctuation tomography” (TFT). This method was  
115 used to reconstruct the grain size distribution of magnetite in both synthetic and natural tuff and  
116 paleosol samples. Theoretically, TFT can also be used for weakly magnetic minerals like hematite  
117 that have a wider size range for SSD behaviour (Banerjee, 1971; Kletetschka and Wasilewski,  
118 2002; Özdemir and Dunlop, 2014). Here, we present a TFT procedure to estimate the grain size  
119 and microcoercivity distribution for pigmentary hematite in natural red chert samples based on the  
120 approach of Jackson et al. (2006). Multiple low-temperature magnetic measurements are integrated

121 to constrain the magnetic mineralogy of natural hematite-magnetite-bearing samples. Our results  
122 also provide new insights into the nature of pigmentary hematite in red sedimentary rocks.  
123

## 124 **2. Materials and Methods**

### 125 ***2.1. Inuyama red chert***

126 Red chert is a distinctive hematite-rich biosiliceous sedimentary rock, which was a common  
127 pelagic marine sediment type from the Ordovician to the early Late Cretaceous (Jones and  
128 Murchey, 1986). The Inuyama red chert crops out along the Kiso River about 30 km north of  
129 Nagoya, Japan. Red chert, gray chert, and siliceous claystone were deposited alternately over  
130 thicknesses of several hundred meters in the middle Triassic to early Jurassic (Oda and Suzuki,  
131 2000). Hematite occurs as a finely dispersed pigment of chemical origin in red cherts (Jones and  
132 Murchey, 1986; Matsuo et al., 2003). The Inuyama red chert contains variable mixtures of  
133 magnetite and pigmentary hematite (Oda and Suzuki, 2000; Abrajevitch et al., 2011; Hu et al.,  
134 2021). Four representative samples were selected from three red bedded chert sites (KA1, KA6,  
135 UN2) in the Inuyama area. Biostratigraphic, paleomagnetic, and rock magnetic results for the same  
136 sample set have been published by Oda and Suzuki (2000) and Hu et al. (2021). Radiolarian fossils  
137 indicate that the KA1 and UN2 samples have middle (Anisian) and late Triassic (Norian) ages  
138 while two KA6 samples are of early Jurassic age (Oda and Suzuki, 2000).

139

### 140 ***2.2. Low temperature magnetic measurements***

141 Samples were cut into 4 mm × 4 mm × 3 mm pieces and were measured with a Quantum Design  
142 Magnetic Properties Measurement System (MPMS) at the Black Mountain Paleomagnetism  
143 Laboratory, Australian National University. First, an isothermal remanent magnetization (IRM)  
144 was imparted at 10 K in a 5 T field (LTSIRM) after cooling in zero field (ZFC) and then  
145 demagnetized by ramping the superconducting magnet down in oscillation mode from 100 to 0  
146 mT to simulate an alternating field (AF) demagnetization at 10 K (Lagroix and Guyodo, 2017).  
147 The resulting magnetization was then measured from 10 K to 300 K to obtain LTIRM<sub>@AF100</sub>  
148 warming curves. Following the same protocol, LTIRM<sub>@AF300</sub> warming curves were also measured  
149 for the same sample by ramping the magnet down from 300 to 0 mT after imparting a LTSIRM.

150 In this way, magnetizations carried over different coercivity ranges (>300 mT, 100-300 mT, and  
 151 <100 mT) were separated to identify their low temperature characteristics. In this study,  
 152  $LTIRM_{>300 \text{ mT}}$  is represented by  $LTIRM_{@AF300}$ ,  $LTIRM_{100-300 \text{ mT}}$  is given by  $LTIRM_{@AF100} -$   
 153  $LTIRM_{@AF300}$ , and  $LTIRM_{<100 \text{ mT}}$  is calculated as  $LTSIRM - LTIRM_{@AF100}$ . Second, a 5 T field  
 154 was imparted again at 10 K after ZFC and IRM was measured in zero field during warming to 300  
 155 K to obtain ZFC-LTSIRM curves. Samples were then field-cooled (FC) to 10 K in a 5 T field and  
 156 measured during warming back to 300 K after removing the field (FC-LTSIRM). Third, backfield  
 157 demagnetization curves were measured for the same four samples at 50 logarithmically spaced  
 158 steps from 0.001 T to 5 T after being saturated with an initial 5 T field at eight temperatures: 300  
 159 K, 250 K, 200 K, 150 K, 100 K, 80 K, 50 K, and 10 K. These curves were later decomposed into  
 160 skew-normal coercivity components using the fitting software MAX UnMix (Maxbauer et al.,  
 161 2016). Finally, to test for goethite contributions that will be fully demagnetized at 400 K, samples  
 162 were given a room temperature IRM (RTSIRM) in a 5 T field and were demagnetized by ramping  
 163 the magnet from 300 to 0 mT in oscillation mode. The remaining remanence  $RTSIRM_{@AF300}$  was  
 164 measured in zero field during cooling to 150 K and then during warming to 400 K and then during  
 165 cooling back to 150 K.

166

### 167 **3. Thermal fluctuation tomography theory for hematite**

168 We adapted the tomographic imaging method of Jackson et al. (2006) to estimate  $f(V, H_{k0})$   
 169 distributions for SP and SDD hematite grains. The procedure is described briefly below, with focus  
 170 on modifications made for hematite. For a detailed explanation and derivation of TFT theory, see  
 171 Jackson et al. (2006) and Dunlop (1965).

172

173 The TFT approach involves using backfield remanence data to estimate the blocking field ( $H_B$ ).  
 174 For hematite at a given temperature, we evaluate  $H_B = H_{cr} - H_q$ , where  $H_{cr}$  is the coercivity of  
 175 remanence, and  $H_q$  is the thermal fluctuation field. For a randomly oriented population of  
 176 identical grains,  $H_q$  is expressed as (equation 8 of Jackson et al. (2006)):

$$177 \quad H_q = 0.801 \left( \frac{kT\sqrt{H_k(T)}}{\mu_0 VM_S(T)} \right)^{\frac{2}{3}} \ln^{\frac{2}{3}} \left[ \frac{\tau_{exp}}{\tau_0 \mu_0 \Delta H_{DC} \sqrt{\mu_0 H_k(T)}} \times \left( \frac{kT}{VM_S(T)} \right)^{\frac{2}{3}} \right], \quad (1)$$

178 where  $M_s$  (T) and  $H_k$  (T) are the saturation magnetization and microcoercivity as a function of  
 179 absolute temperature, T, respectively,  $\mu_0$  is the permeability of free space ( $4\pi \times 10^{-7}$  H/m),  $k$  is  
 180 Boltzmann's constant ( $1.38 \times 10^{-23}$  J/K),  $V$  is the hematite particle volume, and  $\tau_0$  is a characteristic  
 181 time related to the natural frequency of gyromagnetic precession. For nanosized hematite,  $\tau_0$  is  
 182 found to be  $10^{-12}$  -  $10^{-11}$  s (Henrik, 2014 and references therein). We here assume  $\tau_0$   $10^{-12}$  s. The  
 183 exposure time  $\tau_{exp}$  for the backfield treatments is assigned as 300 s, and  $\Delta H_{DC}$  is the applied field  
 184 difference between successive backfields. We assume here that the saturation magnetization at  
 185 absolute zero ( $M_{S0}$ ) is 2500 A/m for hematite (Dunlop and Özdemir, 1997), then  $M_S(T)$  can be  
 186 represented using Bloch's 3/2 law (Bloch, 1930):

$$187 \quad M_S(T) = M_{S0} \times \left(1 - B \times T^{\frac{3}{2}}\right), \quad (2)$$

188 where B is the Bloch constant. B is determined by the spin-wave stiffness constant; we adopt  $B =$   
 189  $10^{-5}$  for hematite nanoparticles (Martínez et al., 1996).

190

191 The next step is to describe microcoercivity ( $H_k$ ) as the function of temperature. Two analytic  
 192 models have been used previously to describe the temperature dependence of the coercive force.

193 1. By taking  $\frac{H_k(T)}{H_{k0}} = \left(\frac{M_S(T)}{M_{S0}}\right)^n$  (Dunlop and Özdemir, 2000; Jackson et al., 2006; Menyeh  
 194 and O'Reilly, 1995), where n depends on the dominant anisotropy, we can calculate  
 195  $H_k(T)$  based on Bloch's 3/2 law:

$$196 \quad H_k(T) = H_{k0} \left(1 - B \times T^{\frac{3}{2}}\right)^n, \quad (3)$$

197 However, hematite anisotropy can be complex and published n values for fine-grained  
 198 hematite below room temperature are rare. Study of synthetic nano-sized hematite  
 199 reveals that temperature has a minimal impact on  $M_S(T)$  while coercivity increases  
 200 significantly at low temperature due to frozen canted spins (Satheesh et al., 2017).  
 201 Therefore, n should be large because of the significant  $H_k(T)$  change compared to  
 202 minimal  $M_S(T)$  change. Satheesh et al. (2017) reported  $M_s$  and  $H_c$  for a 64 nm hematite  
 203 sample at both 5 K and 300 K, to give a calculated n value of ~10.

204 2. The temperature dependence of coercivity,  $H_c$  (T), can also be expressed by Kneller's  
 205 law (Kneller and Luborsky, 1963):

$$H_c(T) = H_{c0} \left( 1 - \left( \frac{T}{T_B} \right)^\alpha \right), \quad (4)$$

206 where  $T_B$  is the blocking temperature for SP particles,  $\alpha$  is Kneller's exponent and  $H_{c0}$  is  
 207 the coercivity at absolute zero. For non-interacting single domain nanoparticles with  
 208 uniaxial anisotropy,  $\alpha$  usually takes a value of 0.5 (Kuncser et al., 2020; Maaz et al., 2010;  
 209 Osman and Moyo, 2015). However,  $\alpha$  can deviate from 0.5 due to finite size effects at the  
 210 nanoscale as well as due to variations in volume distribution, randomness of anisotropy  
 211 axes, and interparticle interactions (Nayek et al., 2017). Similar to the  $n$  value in equation  
 212 (3),  $\alpha$  for hematite nanoparticles is poorly constrained.  
 213

214  
 215 To establish a thermally dependent coercivity model for pigmentary hematite in Inuyama red chert,  
 216 we compare the hematite median  $H_{cr}$  values obtained from backfield curve decomposition using  
 217 both models. First, we need to clarify the relationship among different coercivity forms,  $H_c$ ,  $H_{cr}$   
 218 and  $H_k$ . Experimental  $H_{cr}/H_c$  ratios for SSD hematite are almost constant at  $\sim 1.5$  (Martin-  
 219 Hernandez and Guerrero-Suarez, 2012; Peters and Dekkers, 2003; Özdemir and Dunlop, 2014;  
 220 Roberts et al., 2021). The relationship between  $H_{cr}$  and  $H_k$  depends largely on the dominant  
 221 anisotropy type. For randomly oriented identical particles with uniaxial anisotropy, Stoner and  
 222 Wohlfarth (1948) theory gives  $H_{cr}/H_k = 0.524$ . Multiaxial anisotropy, such as cubic or hexagonal  
 223 anisotropy, can increase  $H_{cr}$  (Harrison et al., 2019) and therefore raise this ratio close to 1. The  
 224 high magnetostriction of hematite and weak  $M_s$  suggests a high sensitivity to magnetostrictive  
 225 strain in hematite (Banerjee, 1963); this strain-related anisotropy is taken to be uniaxial. FORC  
 226 diagrams for the studied red chert samples have “ridge-type” distributions for hematite up to 1.2  
 227 T (Hu et al., 2021), which is typical of uniaxial SSD particle assemblages (Egli et al., 2010).  
 228 Therefore, by assuming a dominant uniaxial anisotropy and relatively constant  $H_{cr}/H_c$  ratios for  
 229 SP/SSD hematite in the Inuyama red chert, we adopt linear relationships among  $H_c$ ,  $H_{cr}$  and  $H_k$ .  
 230 Then, for model 1, we fit the hematite median  $H_{cr}$  data using equation (3). Under the assumption  
 231 of a common  $n$  value for all samples, we estimate both  $H_{cr0}$  and  $n$  using Bayesian regression.  
 232 Similarly, by assuming a common  $\alpha$  value, we fit the hematite  $H_{cr}$  data using equation (4) and  
 233 obtain median posterior estimates of  $H_{cr0}$ ,  $T_B$ , and  $\alpha$  via Bayesian regression for model 2 (see  
 234 section 4.3 for details). By selecting an appropriate model based on our experimental data (section

235 4.3) and assigning  $H_{cr0} = 0.524H_{k0}$ , we can estimate  $H_k(T)$ . Then  $H_B(T)$  is obtained by substituting  
 236  $H_B = 0.524H_k - H_q$  into equation (1).

237  
 238 After constructing field blocking contours for hematite, we describe each hematite grain using two  
 239 essential attributes,  $V$  and  $H_{k0}$ . A saturating field applied and removed isothermally at temperature  
 240  $T_1$  magnetizes the entire thermally stable population at that temperature (Figure 1, blue shaded  
 241 region), which corresponds to grains with  $(V, H_{k0})$  that plot above and to the right of the zero-field  
 242 blocking contour for  $T_1$  (Figure 1). Subsequent application and removal of a reverse DC field,  $H_1$ ,  
 243 flips the magnetic moments of grains with  $(V, H_{k0})$  that plot below and to the left of the blocking  
 244 contour for  $(T_1, H_1)$  (Figure 1, hatched area). Each backfield reverses the moments of grains that  
 245 plot in a region on the Néel diagram (Dunlop, 1965; Néel, 1949) bounded by two blocking field  
 246 contours for a specified temperature. The change in remanence  $\Delta M_R$  produced by each DC  
 247 backfield treatment can, therefore, be expressed as (equation 11 of Jackson et al. (2006)):

$$248 \quad \Delta M_R = \int f(V, H_{k0}) d\Omega, \text{ and}$$

$$249 \quad \Omega = \left\{ V, H_{k0} \mid H_{i-1} \leq H_B \leq H_i \right\} \quad (5)$$

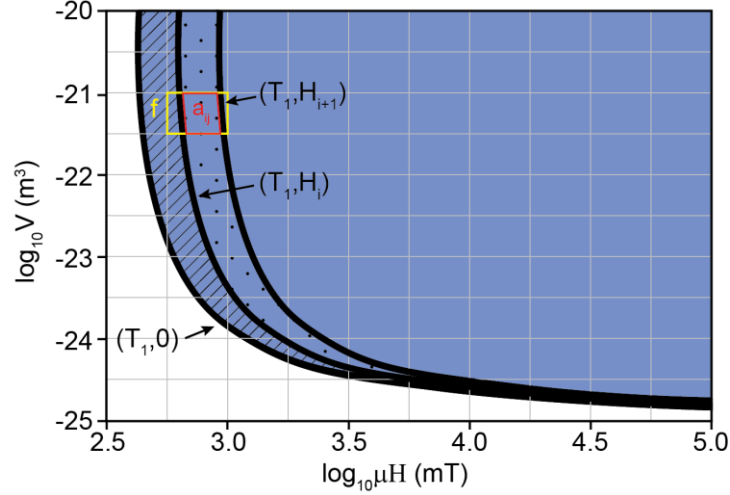
250 where  $\Omega$  represents the region bounded by two blocking field contours and  $H_i$  represents a reverse  
 251 DC field treatment. Therefore, the procedure is essentially an inverse problem involving  $f(V, H_{k0})$   
 252 estimation from a series of DC backfield remanence curves for hematite. Details of procedures  
 253 used to obtain hematite backfield remanence curves are explained in section 4.2.

254  
 255 To estimate  $f(V, H_{k0})$ , we divided the Néel diagram into a rectilinear grid of cells in which  $f$  is  
 256 uniform in each cell (Figure 1, yellow cell). The discrete equivalent of equation (5) is:

$$257 \quad \Delta M_{Ri} = \sum_{j=1}^{n_{\text{cells}}} f_j a_{ij}, \quad (6)$$

258 Where  $a_{ij}$  is the area of cell  $j$  within the area bounded by the blocking contours for a given  
 259 temperature and applied field used when measuring  $\Delta M_{Ri}$  (Figure 1, red region). Each temperature  
 260 and applied field,  $H_{app}$ , pair  $(T, H_{app})$  corresponds to a unique blocking contour, defined as the  
 261 locus of  $(V, H_{k0})$  for which  $H_B(T, V, H_{k0}) = H_{app}$ , so we can calculate intersection points of the

262 contours with the grid lines by piecewise linear interpolation between nodes and approximate the  
 263 contours by straight-line segments between these intersection points to estimate the areas  $a_{ij}$ .



264

265 **Figure 1** Schematic illustration of the TFT technique, modified from Jackson et al. (2006). A  
 266 strong field IRM imparted at temperature  $T_1$  is carried by the entire thermally stable population  
 267 (blue shaded area); a backfield,  $H_1$ , applied and removed at temperature  $T_1$ , reverses the moments  
 268 of grains in the hatched area; a larger backfield,  $H_2$ , further reverses the moments of grains in the  
 269 dotted area.  $a_{ij}$  (red area) represents the area bounded by the blocking contours for  $T_1$  and applied  
 270 fields  $H_{i+1}$  and  $H_i$  when measuring  $\Delta M_{Ri}$ . The yellow rectangle represents the  $j^{\text{th}}$  cell,  $f_j$  is the value  
 271 of  $f(V, H_{k0})$  for the  $j^{\text{th}}$  cell.

272

273 We employ an initialization of  $f = 0$  at all points to generate a forward model based on equation  
 274 (6). Residuals are then calculated as the difference between the measured and model remanence  
 275 data:

$$276 \quad R_i = \Delta M_{Ri, \text{measured}} - \Delta M_{Ri, \text{model}} \quad (7)$$

277 The model is then adjusted by “back-projecting” the residuals:

278

$$279 \quad {}^s \Delta f_{ij} = \frac{R_i a_{ij}}{\sum_{k=1}^{n_{\text{cells}}} a_{ik}^2}. \quad (8)$$

280 The adjustment for cell  $j$  is proportional to  $R_i$  and the area  $a_{ij}$  bounded by the blocking contours.  
 281  $n_{\text{cells}}$  represents the number of cells and  $s$  represents the current simulation. Stepwise updates are  
 282 applied after all calculations for each iteration:

283

$$f_j^{s+1} = f_j^s + \frac{C}{n_{\text{measurements}}} \sum_{i=1}^{n_{\text{measurements}}} \Delta f_{ij} \quad (j = 1 \dots n_{\text{cells}}). \quad (9)$$

285

286 C is a dimensionless constant used to control the rate of convergence, where higher values cause  
 287 more rapid convergence, but excessive values can cause the process to become unstable and  
 288 diverge. Our aim is to reduce the fitting error to ~10% within 100 iterations; after multiple attempts,  
 289 we found that a C value of 50 generally meets our requirement.

290

## 291 **4. Results**

### 292 **4.1. Unblocking of pigmentary hematite**

293 LTSIRM variations of different coercivity fractions for both Triassic and Jurassic red chert  
 294 samples are shown in Figure 2. The Verwey transition for magnetite is clearly evident at ~120 K  
 295 for particles with coercivity < 300 mT, which disappears or becomes less noticeable in  $LTIRM_{>300}$   
 296 curves for the high coercivity component (Figure 2a, 2b), and demonstrating that the coercivity of  
 297 magnetite is mostly less than 300 mT. For Jurassic specimens,  $LTIRM_{>300}$  warming curves decay  
 298 steeply compared to the relatively flat  $LTIRM_{<100}$  curves (Figure 2b), which indicates a wide  
 299 unblocking temperature distribution of a SP hematite content. A concave shape around 200 K is  
 300 present in  $LTIRM_{>300}$  curves, but not in the low coercivity component, which indicates a likely  
 301 Morin transition that was not completely smeared out by progressive unblocking of fine hematite  
 302 (Figure 2b). The  $LTIRM_{100-300}$  warming curve contains both a Verwey transition and marked low  
 303 temperature unblocking, which suggests a mixture of magnetite and finer hematite in this  
 304 coercivity range. Hematite unblocking is less significant for Triassic samples, which indicates a  
 305 smaller SP hematite contribution (Figure 2a). However,  $LTIRM_{>300}$  curves for both Triassic and  
 306 Jurassic samples have comparable magnetizations despite the fact that magnetite has a much  
 307 stronger magnetization, which indicates that hematite dominates the red chert magnetism by mass.

308

309 A Verwey transition is clearly present in both ZFC-LTSIRM and FC-LTSIRM curves, while a  
 310 Morin transition is likely smeared by progressive unblocking of SP hematite (Figure 2c, 2d). ZFC-  
 311 LTSIRM and FC-LTSIRM curves are not widely separated, which contrasts with the behavior of

312 goethite-rich samples (Guyodo et al., 2003; Liu et al., 2006; Huang et al., 2019). Given that the  
313 curves almost overlap (Figure 2c, 2d) it is inferred that any goethite contribution is insignificant.

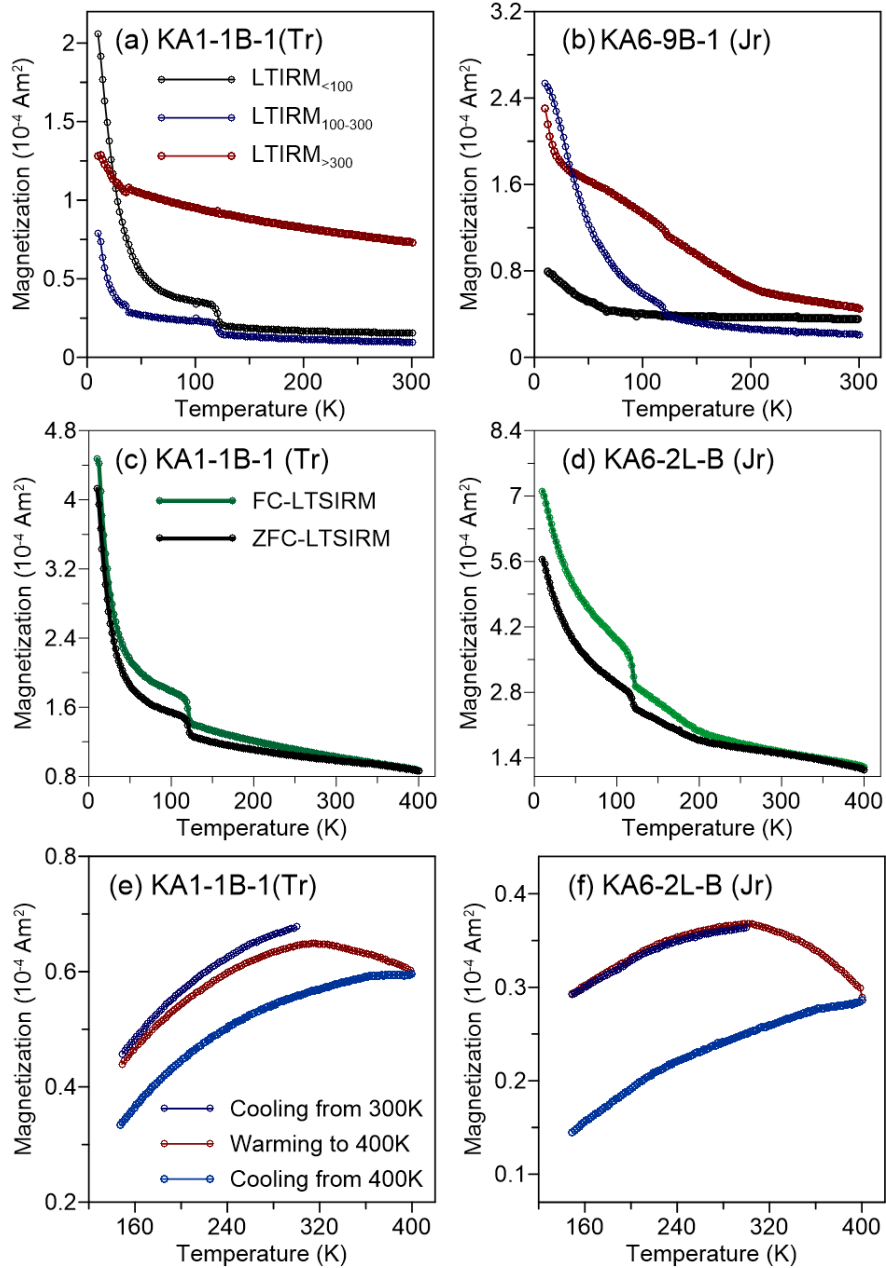
314

315 After removing the low coercivity contribution by applying a 300 mT AF,  $RTSIRM_{@AF300}$   
316 warming curves decrease gradually from 300 K to 400 K with a net remanence loss during re-  
317 cooling (Figure 2e, 2f). No sharp drop is seen at the Néel temperature for goethite. The gradual  
318 decrease in warming curves above 300 K is likely due to unblocking of slightly larger hematite  
319 particles near the SP/SSD size threshold at room temperature.

320

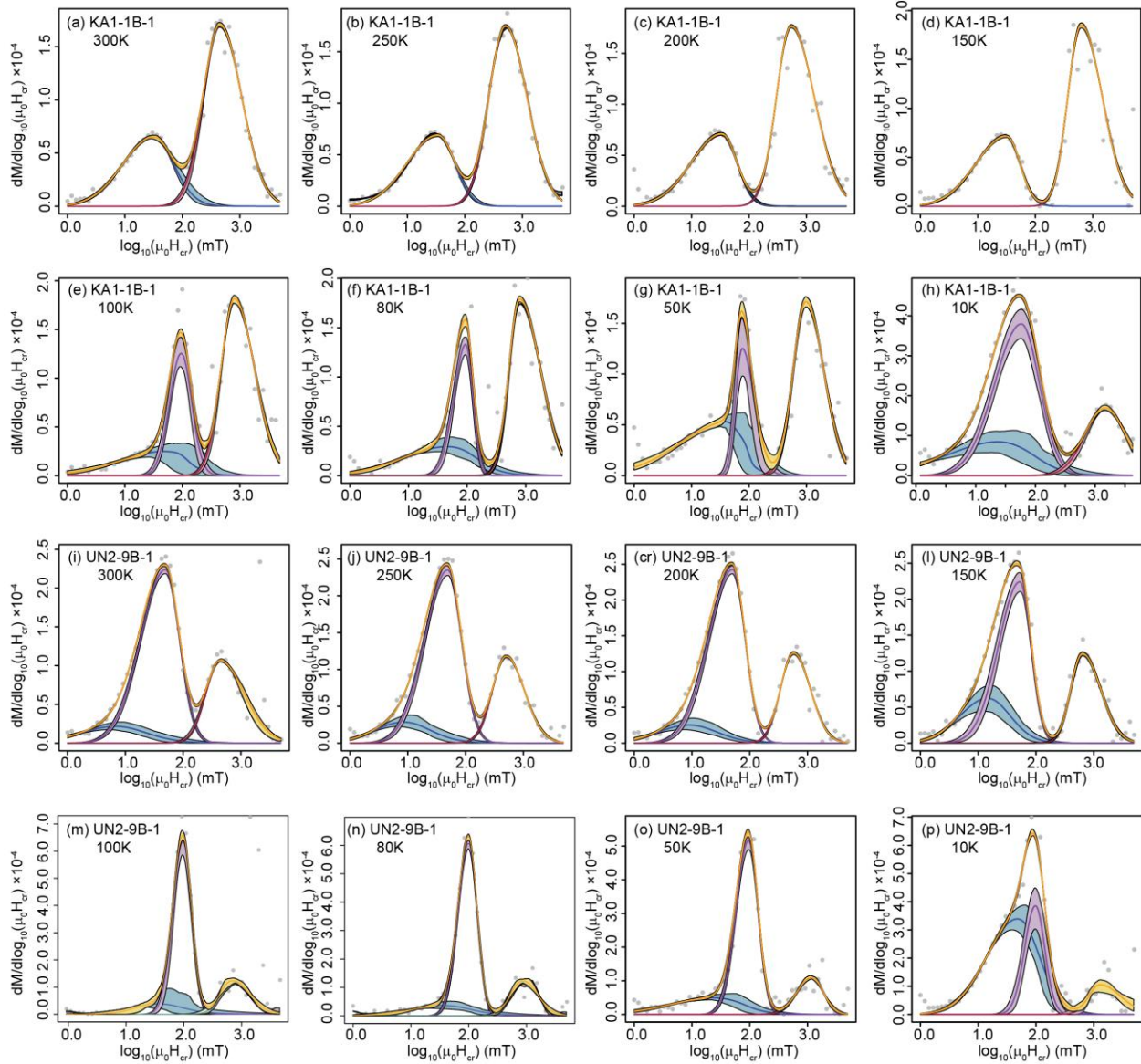
#### 321 ***4.2. Coercivity distributions for pigmentary hematite***

322 The results shown in Figure 2 indicate that goethite is not magnetically important in the Inuyama  
323 red chert and that magnetite is mostly confined to the low coercivity component ( $< 300$  mT). We  
324 further examine coercivity spectra at eight temperatures from 10 K to 300 K. At room temperature,  
325 most Triassic and Jurassic specimens are well fitted with two skew-normal distributions (Figures  
326 3a, 4a, 4i). One distribution has a 19-35 mT median coercivity and extends from 0 to  $\sim 500$  mT  
327 (based on  $\pm 3$  standard deviations from the median coercivity). The other distribution has a higher  
328 median coercivity of 413-598 mT and extends from  $\sim 60$  mT to  $\sim 6$  T, which is likely to be due to  
329 SSD hematite. Triassic sample UN2-9B-1 has an additional lowest-coercivity contribution with a  
330 broad distribution that extends to  $\sim 200$  mT (Figure 3i). At room temperature there is only a small  
331 overlap between the low- and high-coercivity components. With decreasing temperature, the  
332 overlap is reduced and finally disappears or becomes insignificant below 100 K. This behavior is  
333 consistent with hematite coercivity increasing with decreasing temperature (equations (3) and (4)),  
334 while magnetite has a much less dramatic coercivity change with temperature (Özdemir et al.,  
335 2002). The low-temperature dividing point of the low-coercivity component appears at  $\sim 250$  mT,  
336 which is consistent with the Verwey transition being significant in the  $IRM_{<300}$  component (Figure  
337 2a, 2b). Therefore, for both Triassic and Jurassic specimens, the hematite population can be well  
338 separated from magnetite based on their coercivity distributions.



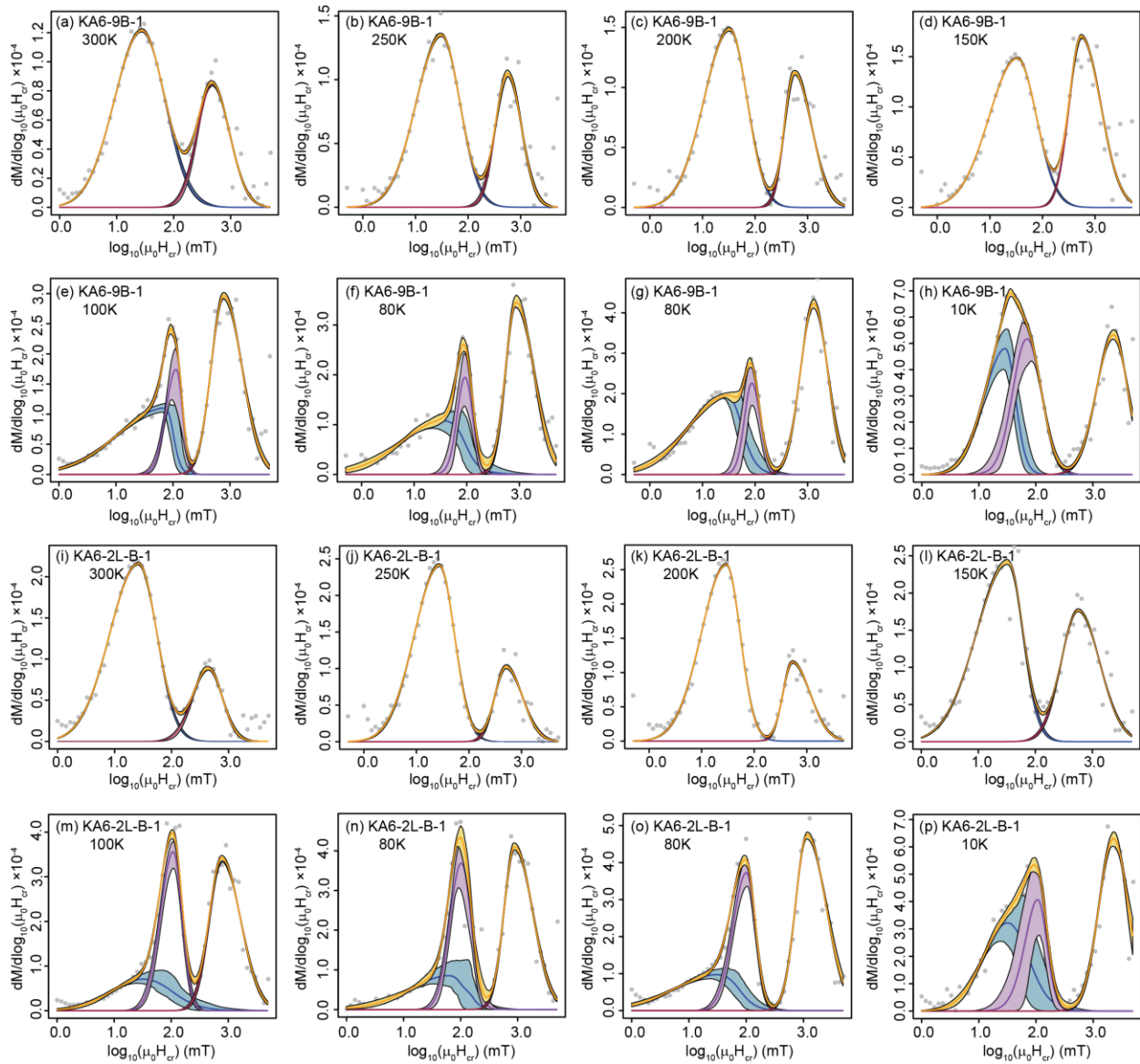
339

340 **Figure 2** LTSIRM variations versus temperature. (a, b) Samples were given a SIRM in a 5 T field  
 341 at 10 K and then AF demagnetized in peak fields of 100 and 300 mT, respectively. Then the  
 342 LTSIRM was measured during warming for components with coercivity ranges of < 100 mT  
 343 (black), between 100 and 300 mT (blue line), and > 300 mT (red). (c, d) ZFC (black) and FC  
 344 (green) LTSIRM curves. (e, f) Samples were saturated in a 5 T field at 300 K and then AF  
 345 demagnetized in a 300 mT peak field. The  $RTSIRM_{@AF300}$  was then measured during cooling to  
 346 150 K (dark blue), warming to 400 K (red), and then cooling back to 150 K (light blue). Tr =  
 347 Triassic; Jr = Jurassic.



348

349 **Figure 3** Coercivity spectra from backfield SIRM demagnetization curves for two Triassic  
 350 specimens (KA1-1B-1, Anisian; UN2-9B-1, upper Norian). The data were fitted using skew-  
 351 normal distributions with the Max Unmix software (Maxbauer et al., 2016). We fitted data with a  
 352 minimum number of components. At eight temperatures, the data can be fitted with 2-3  
 353 components: the lowest coercivity component is shown in blue, the intermediate coercivity  
 354 distribution in purple, and the highest coercivity distribution in red. Yellow lines represent the sum  
 355 of all components, while grey dots represent the data. Shaded areas are 95% confidence intervals  
 356 for each component.

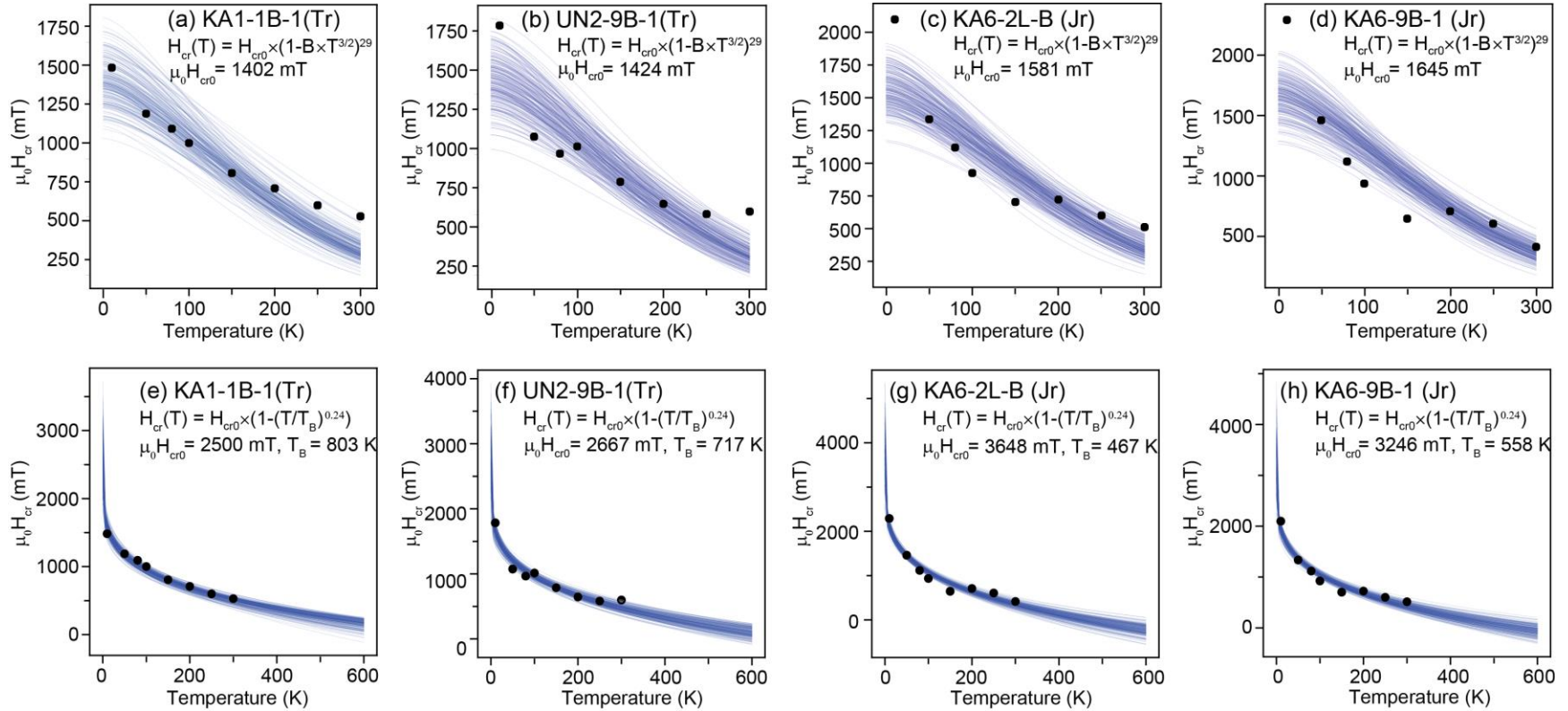


357

358 **Figure 4** Coercivity spectra from backfield SIRM demagnetization curves for two Jurassic  
 359 specimens (KA6-9B-1; KA6-2L-B-1 from early Jurassic). Formatting is the same as Figure 3.

360

361



362

363

364

365

366

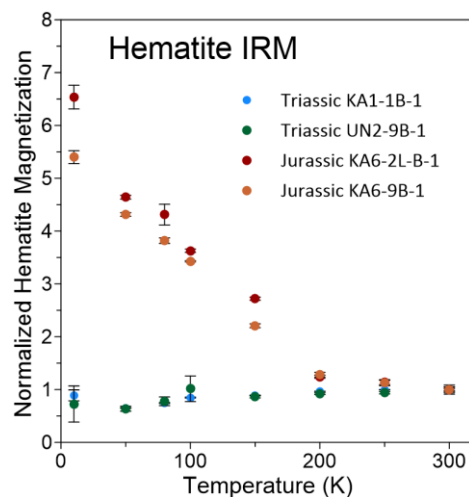
367

368

369

**Figure 5** Hematite median remanent coercivity variation with temperature. (a-d) Bayesian posterior distribution of fitted curves based on equation (3) given the priors listed in Appendix A and assuming a common  $n$  value for all samples. (e-h) Bayesian posterior distribution of fitted curves based on equation (4) given the Bayesian priors listed in Appendix A and assuming a common value of Kneller's  $\alpha$  exponent for all samples. The  $n$  and  $\alpha$  parameters,  $T_B$  shown in the equations are the median values from the parameter posterior distributions. Standard deviations and other posterior distribution statistics are provided in Appendix A.

370 Increases in the coercivity of hematite with decreasing temperature are illustrated in Figure 5.  
 371 Below  $\sim 150$  K, the increase is steeper; it triples for Triassic specimens and increases five-fold for  
 372 Jurassic specimens at 10 K compared to room temperature. The coercivity-temperature fits in  
 373 Figures 5a-5d and 5e-5h were made using equations (3) and (4), respectively, using Bayesian  
 374 regression (Appendix A). In this study, we assume that the exponent parameter  $n$  or  $\alpha$  is constant  
 375 for pigmentary hematite in Triassic/Jurassic Inuyama red chert. Under this assumption, we  
 376 combine all 32 data points from four specimens at eight temperatures to estimate a common  $n$  and  
 377  $\alpha$  posterior distribution and individual posterior distributions of  $H_{cr0}$  and  $T_B$  for each specimen by  
 378 Bayesian regression (see Appendix A for details). As expected, large  $n$  values of 22 - 36 (97%  
 379 high density interval) are obtained, which demonstrates that the hematite coercivity increases more  
 380 strongly than  $M_s$ . However, these fits are less satisfying at low- and room-temperature. The fits  
 381 tend to underestimate  $H_{cr0}$  and the coercivity close to room temperature due to the flatness of the  
 382 fitted curves, which largely comes from the  $3/2$  exponent. Fits based on equation (4) achieve better  
 383 results (Figure 5e-5h). The posterior  $\alpha$  ranges from 0.151 to 0.339 (97% high density interval) with  
 384 median value of 0.24. Triassic red chert samples have lower  $H_{cr0}$  and higher  $T_B$  than Jurassic red  
 385 cherts. Low  $T_B$  values of  $\sim 194$  °C and  $\sim 285$  °C are predicted for hematite in Jurassic red cherts,  
 386 which suggests they have a fine grain size.



387

388 **Figure 6** Hematite IRM variation with temperature. Data are normalized by hematite IRM at 300  
 389 K for each sample. Error bars represent fitting errors for the hematite component.

390

391 Distinctively IRM intensity changes for hematite with temperature are shown for Triassic and  
392 Jurassic samples, respectively, in Figure 6. The hematite remanence remains relatively constant  
393 for the Triassic specimens (blue and green dots), which indicates that almost all of the hematite is  
394 in the SSD state at room temperature. In contrast, hematite remanence increases exponentially with  
395 decreasing temperature for the Jurassic samples (brown and red dots), which indicates a significant  
396 SP contribution with a wide blocking temperature range.

397

#### 398 ***4.4. Tomographic Analysis***

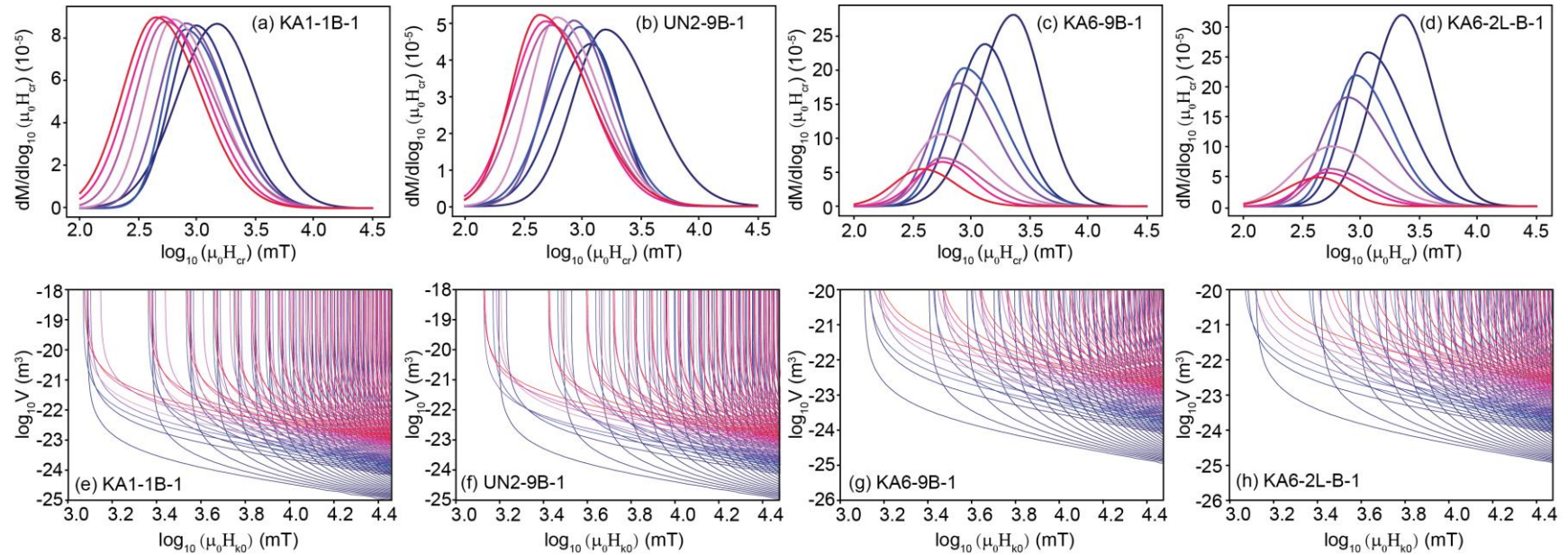
399 Based on the above results, for our tomographic analysis we adopted Kneller's law as a coercivity-  
400 temperature relationship with  $\alpha = 0.24$  and  $H_{cr} = 0.524H_k$ . The median  $T_B$  values shown in Figure  
401 5e-5f are used for each specimen to calculate hematite blocking contours. Hematite coercivity  
402 distributions extracted from the high-coercivity component fitting in Figures 3 and 4 are shown in  
403 Figure 7a-7d. Each dataset contains 808 backfield remanence data points (101 field steps at each  
404 of eight temperatures). These data are combined with equations (1) and (4) and are mapped into  
405 blocking contours (Figure 7e-7h).

406

407 Upon cooling to 10 K, all backfield derivative curves shift progressively to higher coercivities as  
408 expected. Peak heights are roughly constant for Triassic samples but increase significantly upon  
409 cooling for Jurassic samples (Figure 7). This indicates a greater SP hematite content that blocks  
410 gradually with cooling in Jurassic red chert, while the Triassic red chert is dominated by coarser  
411 SSD hematite. The blocking contour density is nonuniform, so poor resolution is expected for  
412 particles smaller than  $\sim 10$  nm with microcoercivities less than  $\sim 1$  T.

413

414 After determining the blocking contours, we start the iterative process to calculate the joint grain  
415 size and microcoercivity distribution of hematite particles. Best-fit backfield derivative curves  
416 reproduce large-scale features of the measured spectra, while still containing higher frequency  
417 deviations (Figures A2-A5). Fitting errors are below 15% for all samples.



418

419 **Figure 7** Hematite backfield remanence data and blocking contours for Triassic and Jurassic red cherts. (a-d) Hematite coercivity  
 420 distributions extracted from backfield LTSIRM decomposition at eight temperatures from 10 K to 300 K. (e-h) Blocking contours for  
 421 the fields and temperatures in the corresponding datasets above. The equations in Figure 5e-5h are used for each respective specimen.  
 422 Color variations indicate temperature changes from 10 K (blue) to 300 K (red).

423

424

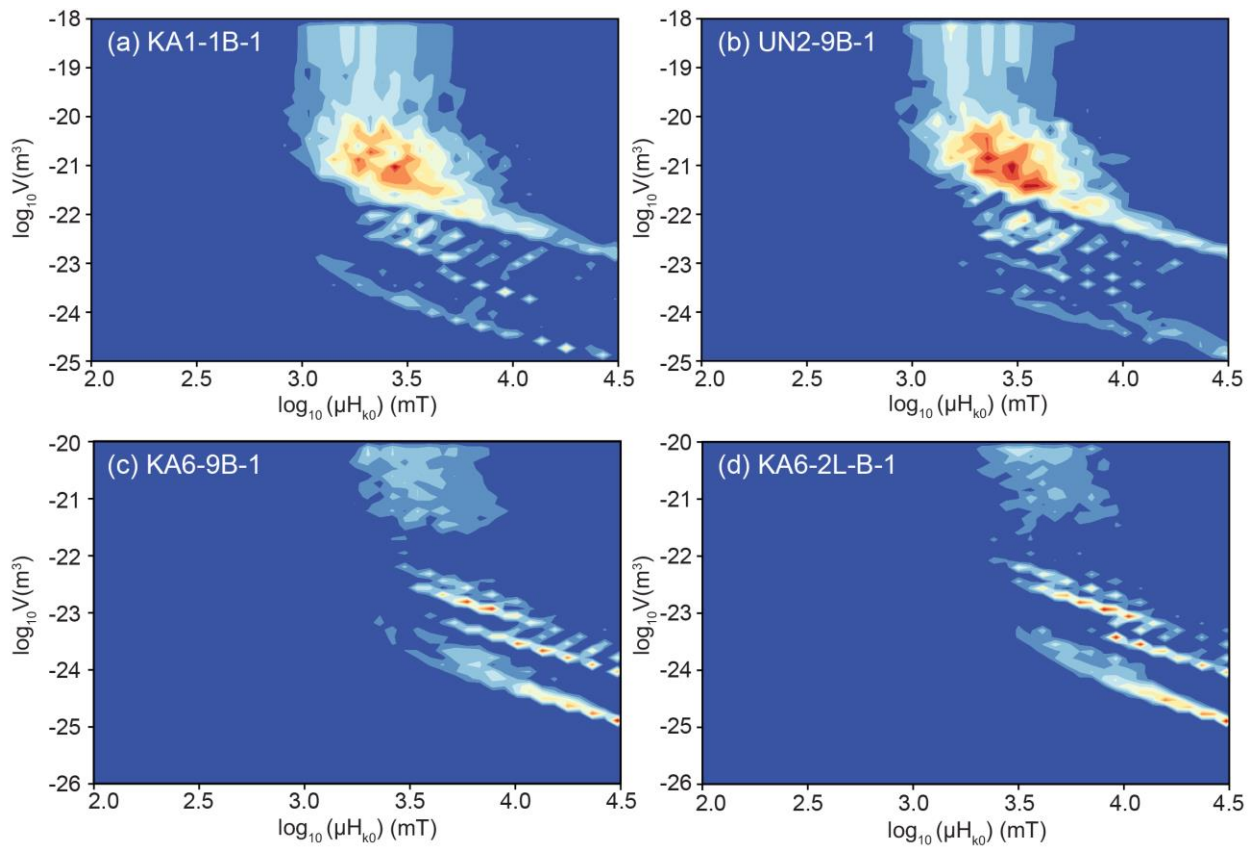
425

426

427

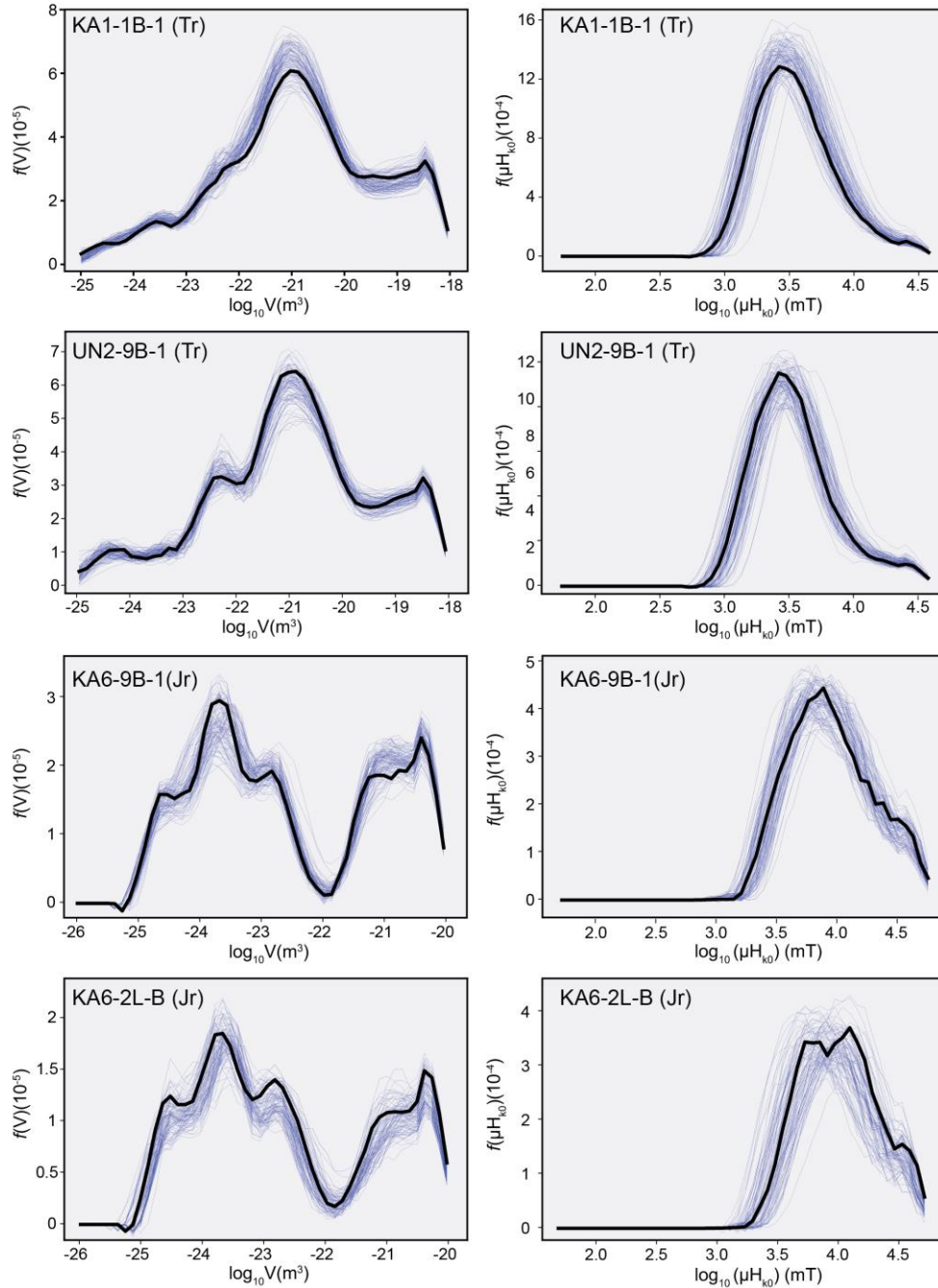
428

429 Estimated  $f(V, H_{k0})$  distributions for Triassic samples have a continuous feature centering at  
 430 volumes around  $1 \times 10^{-21} \text{ m}^3$  and microcoercivities between 1 T and 10 T (Figure 8a, 8b). The  
 431 central volumes are equivalent to spherical hematite particles with  $\sim 75 \text{ nm}$  diameters. In Jurassic  
 432 samples, the hematite particles are smaller but magnetically harder (Figure 8c, 8d), with more  
 433 discrete distributions centered around volumes of  $\sim 1 \times 10^{-25} \text{ m}^3$ ,  $\sim 1 \times 10^{-23.5} \text{ m}^3$ ,  $\sim 1 \times 10^{-22.5} \text{ m}^3$ , and  
 434  $> 1 \times 10^{-22} \text{ m}^3$ , which correspond to diameters of  $\sim 3 \text{ nm}$ ,  $\sim 11 \text{ nm}$ ,  $\sim 24 \text{ nm}$ , and  $> 35 \text{ nm}$  for  
 435 spherical hematite. The microcoercivity of Jurassic hematite ranges from 3 T to  $> 30 \text{ T}$ . There is  
 436 clear elongation of the distribution toward the lower right, along with the dominant blocking  
 437 contour orientation, which may be an artifact of the inversion process (Jackson et al., 2006).  
 438



439  
 440  
 441 **Figure 8** Estimated  $f(V, H_{k0})$  for (a, b) Triassic and (c, d) Jurassic red chert samples from the  
 442 data in Figure 6a-d. Contour interval =  $f_{\text{max}}/30$ .

443  
 444



445

446 **Figure 9** Volume and microcoercivity distributions obtained by summing the rows and columns  
 447 of the 2D model. The data were smoothed with a Savitzky-Golay filter with window length of 5  
 448 in ‘nearest’ mode using the Python Scipy.signal package. Thick black lines represent the median  
 449 value; light blue lines represent calculations based on 100 randomly drawn  $T_B$  and  $\alpha$  values from  
 450 the Bayesian posterior distribution in Figure A1, which are used to indicate the uncertainty on  
 451 the calculation of the volume and microcoercivity distribution.

452 Bayesian modeling was used to calculate the volume and microcoercivity distributions shown in  
453 Figure 9. Thick black lines represent the median volume and microcoercivity distribution for each  
454 sample based on median  $T_B$  and  $\alpha$  values. The light blue lines represent calculations based on 100  
455 randomly drawn  $T_B$  and  $\alpha$  values from their Bayesian posterior distribution in Figure A1, which  
456 indicates the uncertainty on the volume and microcoercivity distribution calculation. The  
457 marginalized microcoercivities are nearly lognormally distributed. Additional high  
458 microcoercivity contributions ( $> 10$  T) are more evident in the Jurassic hematite than Triassic  
459 hematite. By contrast, volume distributions are asymmetrical and more complex. Triassic hematite  
460 populations have a small peak at  $1 \times 10^{-23}$  to  $1 \times 10^{-22}$  m<sup>3</sup> and then gradually increase to a major peak  
461 at  $\sim 1 \times 10^{-21}$  m<sup>3</sup> (Figure 9a). Additional coarse particles with volume larger than  $1 \times 10^{-20}$  m<sup>3</sup> are also  
462 present. The Jurassic hematite population has a roughly bimodal distribution separated at around  
463  $1 \times 10^{-22}$  m<sup>3</sup>. The larger particle population has a broad peak from  $1 \times 10^{-22}$  m<sup>3</sup> to  $1 \times 10^{-20}$  m<sup>3</sup>. The  
464 smaller particle population has a major peak at  $\sim 1 \times 10^{-24}$  m<sup>3</sup> with two smaller peaks at  $1 \times 10^{-24.6}$  m<sup>3</sup>  
465 and  $1 \times 10^{-23}$  m<sup>3</sup>, which correspond to their discrete components in Figure 8c, 8d. The discrete  
466 nature of the distribution is most likely due to the limited numbers of temperatures used here  
467 because the distributions are all elongated along the unblocking contours. Nevertheless, two grain  
468 size populations are evident in Jurassic samples; the finer fraction ranges from a few nanometers  
469 to  $\sim 35$  nm in diameter while the coarser fraction is from  $\sim 35$  nm to  $\sim 160$  nm in diameter and is  
470 comparable with Triassic samples.

471

## 472 **5. Discussion**

### 473 ***5.1. Coercivity of pigmentary hematite in red chert***

474 Early studies of the Inuyama red chert reported large saturating fields of up to several tesla for  
475 pigmentary hematite from IRM acquisition curves (Oda and Suzuki, 2000; Shibuya and Sasajima,  
476 1986). In our results, room temperature  $\mu_0 H_{cr}$  ranges from  $\sim 60$  mT to  $\sim 6$  T in Triassic red chert  
477 and from  $\sim 70$  mT to  $\sim 3$  T in Jurassic red chert (Figures 3 and 4), which is comparable to recent  
478 studies (Abrajevitch et al., 2013; Hu et al., 2021). Published data for pigmentary hematite in red  
479 beds have a similarly wide range of  $\mu_0 H_{cr}$  values. In the Deer Lake Group red beds of western  
480 Newfoundland, hematite remanent coercivity ranges from  $\sim 60$  mT to 3 T (Bilardello and Kodama,  
481 2010a), and for red beds from the Maritime provinces of Canada, it varies from  $\sim 40$  mT to 5 T and

482 beyond (Bilardello and Kodama, 2010b). Hematite in Triassic red beds from South China has  
483 remanent coercivity values from ~60 mT to 3 T (Jiang et al., 2017). For zebra rock in Western  
484 Australia, strong fields up to 3 T are needed to saturate hematite (Abrajevitch et al., 2018). North  
485 American red siltstone intraclasts have remanent coercivity of ~100 mT to 1.8 T and beyond  
486 (Swanson-Hysell et al., 2019). Thus,  $\mu_0 H_{cr}$  values of ~60 mT to ~3 T are typical of natural  
487 pigmentary hematite in red beds, although values up to even ~6 T are sometimes observed. This  
488  $\mu_0 H_{cr}$  range gives an idea of the remanent coercivity distribution of natural SSD pigmentary  
489 hematite.

490

491 We further illustrate remanent coercivity variations with temperature for pigmentary hematite.  $H_{cr}$   
492 increases exponentially with decreasing temperature, following the  $T^\alpha$  law, where  $\alpha = 0.24$  is the  
493 median posterior value for red chert samples in this study (Figure 5e, 5f, 5g, 5h). This behavior  
494 can be understood by considering thermal fluctuation effects of blocked moments across an  
495 anisotropy barrier (Maaz et al., 2010). For natural pigmentary hematite, this simple thermal  
496 activation model appears to be applicable from 10 K to 300 K. The significant  $H_{cr}$  increase at low  
497 temperatures also provides a way to separate a hematite component from magnetite. Based on  
498 results in Figures 2 and 3, there is almost no overlap between magnetite and hematite components  
499 below 100 K.

500

501 Quintupled hematite  $M_{rs}$  values at 10 K compared to room temperature confirms the presence of a  
502 large SP hematite population in the Jurassic red chert (Figure 6). The steep  $M_{rs}$  rise below 200 K  
503 indicates that the blocking temperature of most SP hematite is below 200 K. Our results  
504 demonstrate that decomposition of low temperature backfield curves reveals and potentially  
505 enables quantification of entire pigmentary hematite populations, especially SP particles. Although  
506 SP signatures are detected in remanent FORC diagrams (Hu et al., 2021), these signals tend to be  
507 dominated by magnetite because FORC diagrams reflect bulk signals and the magnetization of  
508 hematite is more than two hundred times lower than magnetite (Dunlop and Özdemir, 1997).

509

510 Compared to room-temperature  $H_{cr}$ , which only represents SSD populations,  $H_{k0}$  provides a  
511 measure of the entire hematite population, including SP particles. In the calculations of Jackson et  
512 al. (2006),  $\mu_0 H_{k0}$  values for magnetite in a Tiva Canyon Tuff sample can extend to 300 mT, which

513 is the upper limit for prolate spheroids with magnetite-like magnetizations. According to our  
514 calculations,  $\mu_0 H_{k0}$  for the pigmentary hematite can be much higher, and varies from 1 T to  $\sim 10$  T  
515 in Triassic red chert and from  $\sim 1.5$  T to  $> 30$  T in Jurassic red chert (Figure 9). As is the case for  
516 magnetite, microcoercivity distributions for hematite are nearly symmetric in logarithmic space  
517 (Figure 9).

518

519 The high coercivity of pigmentary hematite cannot be explained by shape anisotropy (Banerjee,  
520 1971). Özdemir and Dunlop (2014) concluded by studying MD hematite that both magnetoelastic  
521 and magnetocrystalline effects contribute to coercivity. However, magnetocrystalline anisotropy  
522 causes a gradual coercivity decrease during cooling below room temperature (Liu et al., 2010;  
523 Özdemir et al., 2002), which is opposite to the temperature dependence of coercivity observed  
524 here. The increasing coercivity trend with cooling in pigmentary hematite is interpreted to be due  
525 to magnetoelastic anisotropy, which arises from crystal defects, dislocations, or internal strain  
526 (Sunagawa and Flanders, 1965; Sunagawa, 1960; Liu et al., 2010).

527

## 528 ***5.2. Grain size distribution and unblocking temperature of pigmentary hematite in red chert***

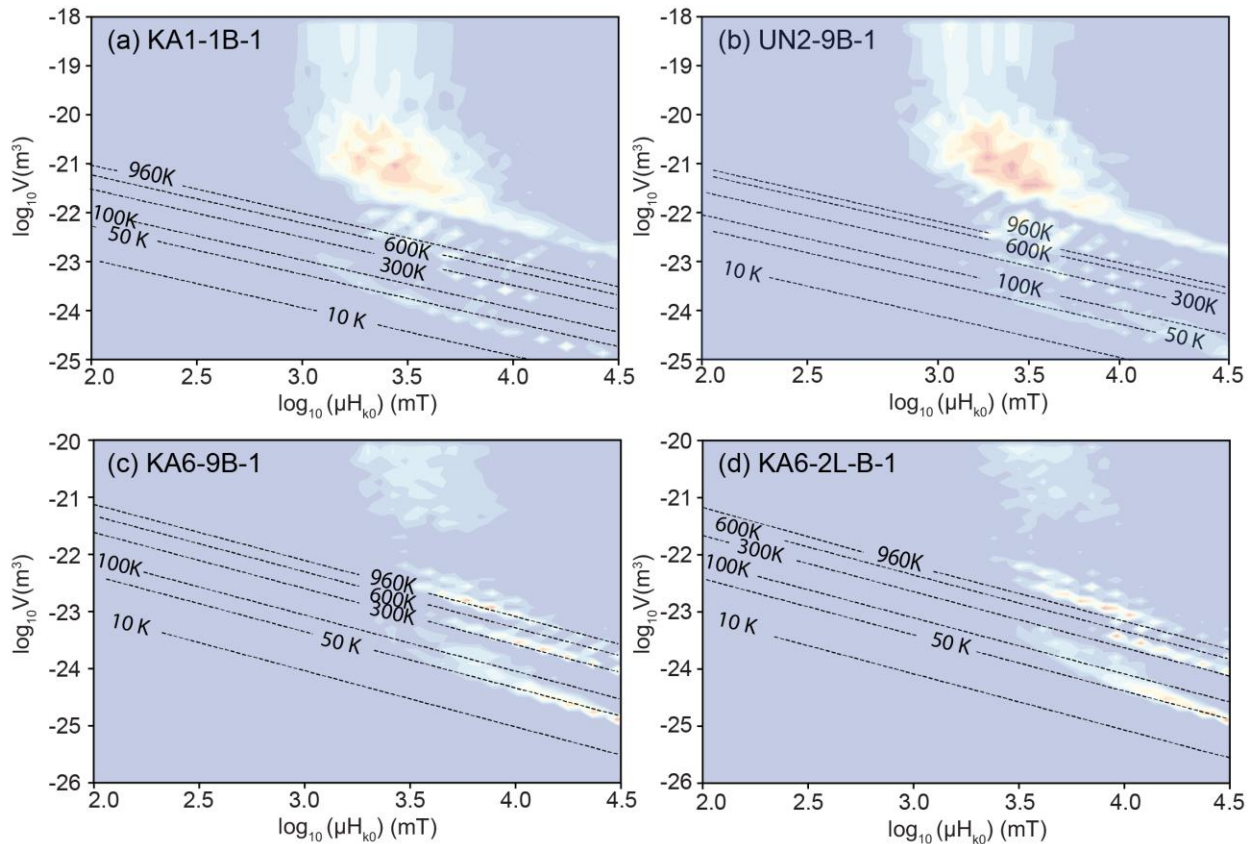
529 Our analysis reveals that both Triassic and Jurassic red chert samples have hematite population  
530 with median size of  $\sim 75$  nm. Additional large amounts of finer hematite  $< \sim 35$  nm occurs in the  
531 Jurassic red chert (Figure 9). The median  $T_B$  for each red chert sample is  $529$  °C (KA1-1B-1),  
532  $438$  °C (UN2-9B-1),  $194$  °C (KA6-2L-B-1), and  $285$  °C (KA6-9B-1). The low unblocking  
533 temperatures are also consistent with the small particle size of pigmentary hematite. According to  
534 the unblocking temperature and grain size model of Swanson-Hysell et al. (2011, 2019), the  
535 median unblocking temperatures in red chert correspond to grain sizes of 100-160 nm, which is  
536 within the range of our calculated grain size distributions. The broad unblocking temperature  
537 distribution reflects the wide size distribution of natural pigmentary hematite.

538

539 We further calculated  $T_B$  contours based on the volume and microcoercivity distributions obtained  
540 here (Figure 10). Almost the entire pigmentary hematite population in the Triassic red cherts is in  
541 the SSD state at room temperature, with unblocking temperatures generally above 300 K (Figure  
542 10a, b). For the Jurassic red cherts, a significant part of the hematite is in the SP state with

543 unblocking temperatures extending below 100 K. The SP/SSD threshold size for stoner-wohlfarth  
 544 hematite has been estimated at 25-30 nm (Banerjee, 1971; Özdemir & Dunlop, 2014) and at 17  
 545 nm for Al-hematite (Jiang et al., 2014). From our  $T_B$  calculations, the SP/SSD threshold size for  
 546 stoichiometric hematite in the Jurassic red cherts is 7-18 nm, which is close to estimates for Al-  
 547 hematites.

548



549

550 **Figure 10** Calculated blocking temperature contours from 10 K to 960 K with  $f(V, H_{k0})$

551 distributions for (a, b) Triassic and (c, d) Jurassic samples.

552

553 Detailed paleomagnetic studies have been conducted on the Inuyama red chert, with four  
 554 remanence components identified from stepwise thermal demagnetization (Oda and Suzuki, 2000;  
 555 Shibuya and Sasajima, 1986). The four components are labeled A (70-200 °C), B (200-350 °C), C  
 556 (350-530 °C), and D (530-680 °C). Components B and C were thought to be Late Cretaceous  
 557 remagnetizations, although the remagnetization mechanism has been debated. Partial thermal  
 558 demagnetization (ThD) after alternating field (AF) demagnetization at 80 mT reveals the same

559 four components (Oda and Suzuki, 2000), which indicates that hematite was at least partly  
560 responsible for all four components. This is consistent with the wide unblocking temperature range  
561 for hematite in our calculations. Paleomagnetic studies of the Inuyama red chert have all suggested  
562 that magnetite is the dominant remanence carrier for components A, B, and C and, thus, magnetite  
563 carries the remagnetizations. However, pigmentary hematite should also contribute to the  
564 remagnetizations due to its low unblocking temperature, especially for Component B. We suggest  
565 this because the unblocking temperature range of component B (200-350 °C) and C (350-530 °C)  
566 spans the median hematite unblocking temperature range. Meanwhile, little magnetization for  
567 component B was lost between 200 and 350 °C in the original ThD experiment (Figure 6a from  
568 Oda and Suzuki (2000)), but the magnetization drops significantly after AF demagnetization of 80  
569 mT (Figure 6c in Oda and Suzuki (2000)). According to our analysis on the magnetite remanent  
570 coercivity distribution of the Inuyama red chert at room temperature (Figure 3 and Figure 4), an  
571 alternating field of 80 mT will demagnetize most of the magnetite, which suggests that the more  
572 significant unblocking feature of component B after AF demagnetization is likely due to  
573 pigmentary hematite.

### 574 ***5.3. Limitations of the TFT method for reconstructing hematite grain size distributions***

575 There are two main limitations of the TFT technique for hematite. First, it has the same limitation  
576 for hematite as it does for magnetite (Jackson et al., 2006). Reconstructed size distributions are  
577 elongated toward the upper left and lower right-hand sides of the Néel diagram, along the blocking  
578 contour orientation. This elongation can be due to artifacts in the inversion method, the physical  
579 model, and the assumption made, as shown by Jackson et al. (2006) and Dunlop (1965). Resolution  
580 limits also remain for inversion due to the restricted orientation distribution of integration paths.  
581 Areas of marginal resolution are sampled sparsely by subparallel contours, such as within the small  
582  $V$ , high  $H_{k0}$  region that is stable only at the lowest temperatures. At the same time, given the small  
583 numbers of temperatures employed, the resolution of our results is imperfect, and stripes are  
584 evident in the  $f(V, H_{k0})$  distribution rather than a smooth continuous distribution (Figure 8c, d).  
585 Increasing the number of temperature steps will improve the resolution, but will also be time and  
586 helium expensive, especially for multiple specimens.

587

588 Second, compared to magnetite, an additional challenge when modeling hematite is the complexity  
589 of its anisotropy. An important assumption in our calculation is that we assign  $H_{cr} = 0.524H_K$ ,  
590 which is based on Stoner and Wohlfarth (1948) theory for identical randomly oriented uniaxial  
591 particles. Harrison et al. (2019) simulated remanence FORC diagrams for particles with uniaxial,  
592 cubic, and hexagonal anisotropy. Among these anisotropy types, randomly oriented, non-  
593 interacting particles with uniaxial anisotropy have the lowest  $H_{cr}$  values, while  $H_{cr}$  for cubic and  
594 hexagonal anisotropy is approximately 1.05 and 1.8 times larger, respectively. Therefore,  
595 multiaxial anisotropy will produce  $0.5 < H_{cr}/H_K < 1$ . Magnetic minerals with uniaxial, cubic, and  
596 hexagonal anisotropy produce distinctive FORC diagram types (e.g., Egli, 2021; Roberts et al.,  
597 2021), which provides a useful way to evaluate the dominant anisotropy type before undertaking  
598 TFT analyses. Conventional and remanence FORC diagrams for the Inuyama red chert all have a  
599 central ridge up to 1.2 T. Although magnetite dominates the FORC signatures, hematite is  
600 responsible for central ridges with coercivities  $> 300$  mT. Ridge-type signatures for conventional  
601 and remanence FORC diagrams are explained as a manifestation of uniaxial SD magnetic behavior  
602 based on simulations (Harrison et al., 2019). However, instead of being shape dominated, as is the  
603 case for magnetite, ridge-type FORC signals for hematite nanoparticles reflect stress-induced  
604 uniaxial anisotropy that dominates the intrinsic magnetocrystalline anisotropy (Roberts et al.,  
605 2021). This magnetostrictive anisotropy associated with uniaxial internal stress controls the  
606 coercivity of hematite, which is consistent with the rapid  $H_{cr}$  increase at low temperatures (Figure  
607 5) that is usually enhanced in nanoparticles (Muench et al., 1985; Bruzzone and Ingalls, 1983).  
608 Therefore, considering the ridge-type signals observed in both conventional and remanence FORC  
609 diagrams for the red chert (see Figure 2 and 3 in Hu et al. (2021)) and  $H_{cr}$  variation with  
610 temperature, we predict that uniaxial anisotropy dominates pigmentary hematite in red chert and  
611 adopt  $H_{cr}/H_K = 0.524$ . Increased  $H_{cr}/H_K$  will result in decreased microcoercivity, increased  $T_B$   
612 estimates, and slightly decreased grain size estimates. Thus, when considering variations in the  
613 dominant anisotropy type, our calculations at least provide an upper limit of microcoercivity and  
614 grain size and a lower  $T_B$  limit.

615

## 616 **6. Conclusions**

617 Reconstructions of particle microcoercivity and volume distributions were performed with the  
618 method of Jackson et al. (2006) for SP/SSD hematite assemblages assuming a dominant uniaxial

619 anisotropy. The median temperature variation of  $H_{cr}$  for pigmentary hematite in Triassic/Jurassic  
620 red chert over eight temperatures from 300 K to 10 K follows a modified Kneller's law;  
621  $H_{cr}(T) = H_{cr0} \left( 1 - \left( \frac{T}{T_B} \right)^{0.24} \right)$ . The coercivity of hematite increases more rapidly than for  
622 magnetite with decreasing temperature, and coercivity distribution overlap between the two  
623 minerals starts to disappear below 100 K. Microcoercivity distributions that are nearly symmetric  
624 in logarithmic space vary from 1 T to ~10 T in Triassic red chert and from ~3 T to 30 T in  
625 Jurassic red chert. Both Triassic and Jurassic red chert have wide hematite grain size  
626 distributions. Most of the Triassic hematite ranges between ~35 nm to ~160 nm in diameter  
627 while the Jurassic red chert has a coarser hematite particles fraction similar to the Triassic  
628 hematite and a finer hematite fraction with grain size from a few nanometers to ~35 nm in  
629 diameter. Calculated median  $T_B$  varies from ~194 °C to 529 °C for red chert samples and  $T_B$   
630 contours indicate that most of the Triassic hematite is in the SSD state with a significant SP  
631 particle content with  $T_B < 300$  K. The SP/SSD threshold size for pigmentary hematite in Jurassic  
632 red chert is estimated to be 8-18 nm. Considering the low and broad  $T_B$  distribution in the  
633 Inuyama red chert, we propose that pigmentary hematite has a significant contribution to a  
634 secondary early Cenozoic thermoviscous magnetization rather than magnetite (Component B  
635 defined by Oda and Suzuki (2000)).

636  
637 Our work demonstrates that the main features of SP/SSD hematite  $f(V, H_{k0})$  distributions can be  
638 recovered using the TFT technique, although details should be interpreted judiciously. Smearing  
639 of results due to low measurement resolution, artifacts, and variations in dominant anisotropy of  
640 hematite should be considered on a case-by-case basis. Ridge-like FORC signatures for red chert  
641 are interpreted here to indicate a dominant uniaxial anisotropy. If multiaxial anisotropy is instead  
642 dominant in hematite samples (e.g., Roberts et al., 2021), this would increase  $T_B$  estimates and  
643 decrease microcoercivity and grain size estimates.

644

#### 645 **Data Availability Statement**

646 All low-temperature magnetic data used here will be uploaded to the Magnetic Information  
647 Consortium rock magnetic portal (MagIC; [www.earthref.org](http://www.earthref.org)).

648

649

650 **Acknowledgments**

651 We thank Mike Jackson for providing the original TFT code. This work was supported by the  
 652 National Institute of Advanced Industrial Science and Technology, Ministry of Economy, Trade  
 653 and Industry, Japan, and the Australian Research Council through grants DP160100805 and  
 654 DP200100765.

655

656

657 **Appendix A**

658 Bayesian regression was performed using the PyMC3 Python package (Salvatier et al., 2016).

659 The parameterizations of the Bayesian prior distributions for  $H_{cr0}$ ,  $T_B$ ,  $\alpha$  and fitting error  $\sigma$  are  
 660 provided below.

661 **1.  $H_{cr0}$**

662 The prior for  $\mu_0 H_{cr0}$  follows a log normal distribution with median value of 0 and variance of  
 663 1. Thus, the probability density function can be expressed as:

664

$$665 \quad p(\mu_0 H_{cr0}) = \frac{1}{\mu_0 H_{cr0} \sqrt{2\pi}} \exp\left(-\frac{\ln(\mu_0 H_{cr0})^2}{2}\right) \quad (A1)$$

666

667

668

669 **2.  $T_B$**

670 Theoretically,  $T_B$  can vary between 0 and 960 K for hematite. For better calculation efficiency,  
 671 we set all variable values between 0 and 1 in the Bayesian regression. Therefore, instead of  $T_B$ , we  
 672 use  $T_B/1000$  to follow a Beta distribution with  $\alpha = 2$  and  $\beta = 2$ , the probability density function can  
 673 be expressed as:

$$674 \quad p\left(\frac{T_B}{1000}\right) = \frac{\frac{T_B}{1000} \times \left(1 - \frac{T_B}{1000}\right)}{B(2,2)}; \text{ and} \quad (A2)$$

675

676

$$677 \quad B(2,2) = \frac{\Gamma(2)\Gamma(2)}{\Gamma(4)} \quad (A3)$$

678

679 Where  $\Gamma$  is the Gamma function.

680

681 **3.  $\alpha$  and  $n$**

682  $\alpha$  and  $n$  follow a Beta distribution with  $\alpha = 8$  and  $\beta = 8$ , the probability density function can be  
 683 expressed as:

$$684 \quad p(\alpha) = \frac{\alpha^7 \times (1 - \alpha)^7}{B(8,8)} \text{ or } p\left(\frac{n}{50}\right) = \frac{\left(\frac{n}{50}\right)^7 \times \left(1 - \left(\frac{n}{50}\right)\right)^7}{B(8,8)}, \text{ with} \quad (A4, A5)$$

685  
 686

$$687 \quad B(8,8) = \frac{\Gamma(8)\Gamma(8)}{\Gamma(16)} \quad (A6)$$

688

689 Based on previous studies,  $n$  rarely exceeds the value of 50. Therefore, we normalized  $n$  by 50  
 690 for it to vary from 0 to 1.  $\Gamma$  in equation (A6) is the Gamma function.

691

#### 692 **4. Fitting error $\sigma$**

693  $\sigma$  follows a half-Cauchy distribution with location parameter of 0 and scale parameter of 1.  
 694 The probability density function can be expressed as:

$$695 \quad f(\sigma, 1) = \frac{2}{\pi(1 + \sigma)} \quad (A7)$$

696  
 697

698 The, no U-Turn Sampler (NUTS) from the Python Pymc3 package was used for sampling, in  
 699 where we set both the sampling number and iteration number to 4000.

700

701 Statistical results of Bayesian regression using equation (3) and equation (4), respectively are  
 702 listed. Two hundreds regression curves for each sample are shown in Figure 5. In the following  
 703 tables, hdi\_3% and hdi\_97% are the lower and upper bounds of the 97% high density interval.  
 704  $R_{\hat{}}$  is the Gelman-Rubin convergence statistic, where a value of 1 indicates that the chains have  
 705 converged.

706

707

708

709

710

711

712

713

714 Table A1 Posterior statistics of Bayesian regression of equation (3)

715

	Median	Standard deviation	hdi_3% <sup>1</sup>	hdi_97% <sup>2</sup>	R_hat <sup>3</sup>
n	28.650	3.700	21.650	35.600	1
$\mu_0 H_{cr0}$ (T) (KA1-1B-1)	1.402	0.137	1.133	1.649	1
$\mu_0 H_{cr0}$ (T) (UN2-9B-1)	1.424	0.139	1.166	1.682	1
$\mu_0 H_{cr0}$ (T) (KA6-9B-1)	1.581	0.145	1.308	1.853	1
$\mu_0 H_{cr0}$ (T) (KA6-2L-B-1)	1.645	0.145	1.371	1.916	1
$\sigma$	0.253	0.037	0.189	0.321	1

716

717 Table A2 Posterior statistics of Bayesian regression of equation (4)

718

719

720

721

722

723

724

725

726

727

728

729

730

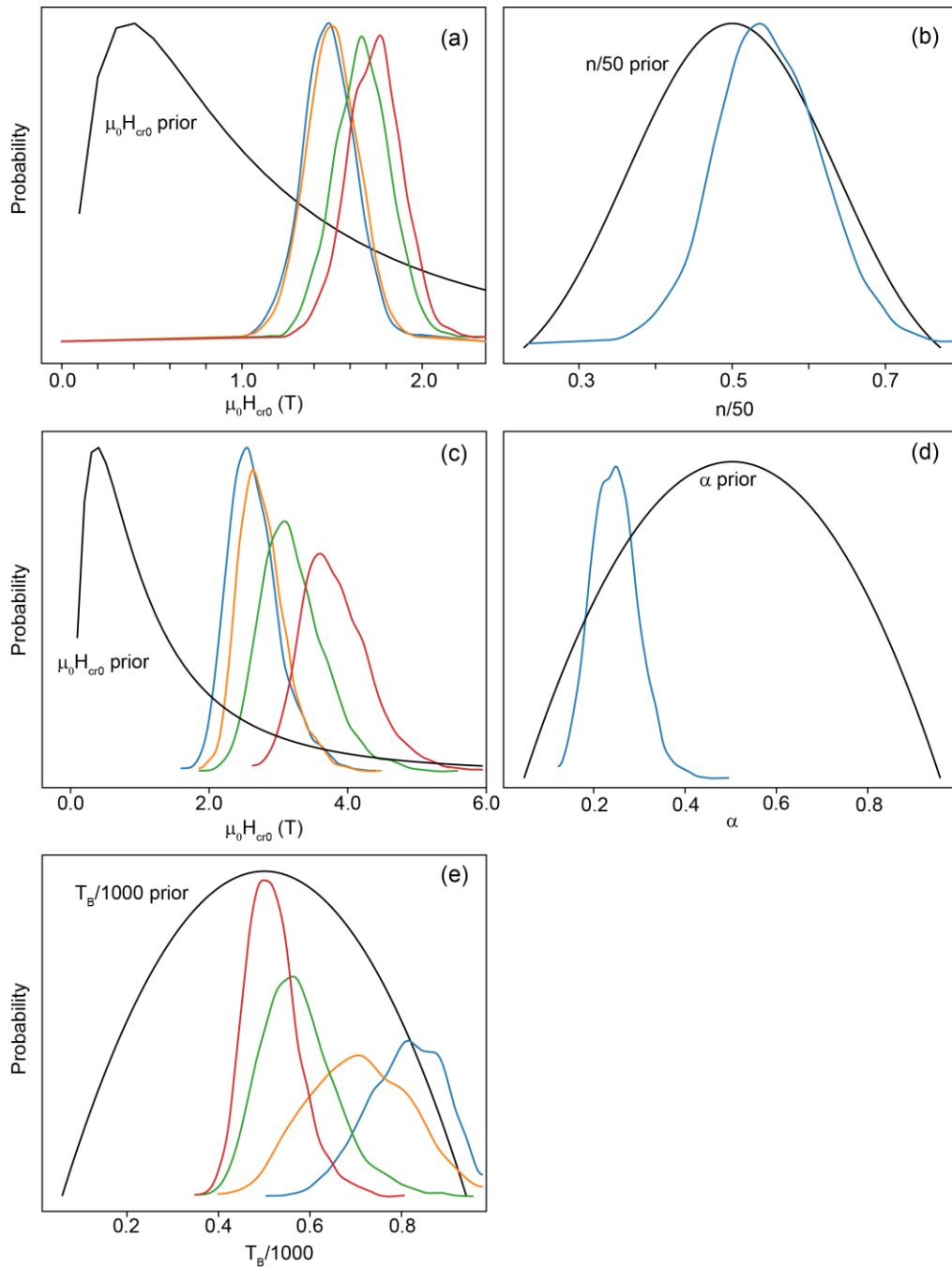
731

732

	mean	Standard deviation	hdi_3% <sup>1</sup>	hdi_97% <sup>2</sup>	R_hat <sup>3</sup>
$\alpha$	0.240	0.052	0.151	0.339	1
$\mu_0 H_{cr0}$ (T) (KA1-1B-1)	2.500	0.383	1.829	3.211	1
$\mu_0 H_{cr0}$ (T) (UN2-9B-1)	2.667	0.405	1.947	3.446	1
$\mu_0 H_{cr0}$ (T) (KA6-9B-1)	3.246	0.494	2.335	4.164	1
$\mu_0 H_{cr0}$ (T) (KA6-2L-B-1)	3.648	0.561	2.627	4.664	1
$T_B/100$ (K) (KA1-1B-1)	0.803	0.099	0.621	0.972	1
$T_B/1000$ (K) (UN2-9B-1)	0.717	0.103	0.534	0.919	1
$T_B/1000$ (K) (KA6-9B-1)	0.558	0.076	0.425	0.701	1
$T_B/1000$ (K) (KA6-2L-B-1)	0.467	0.054	0.370	0.567	1
$\sigma$	0.111	0.019	0.078	0.148	1

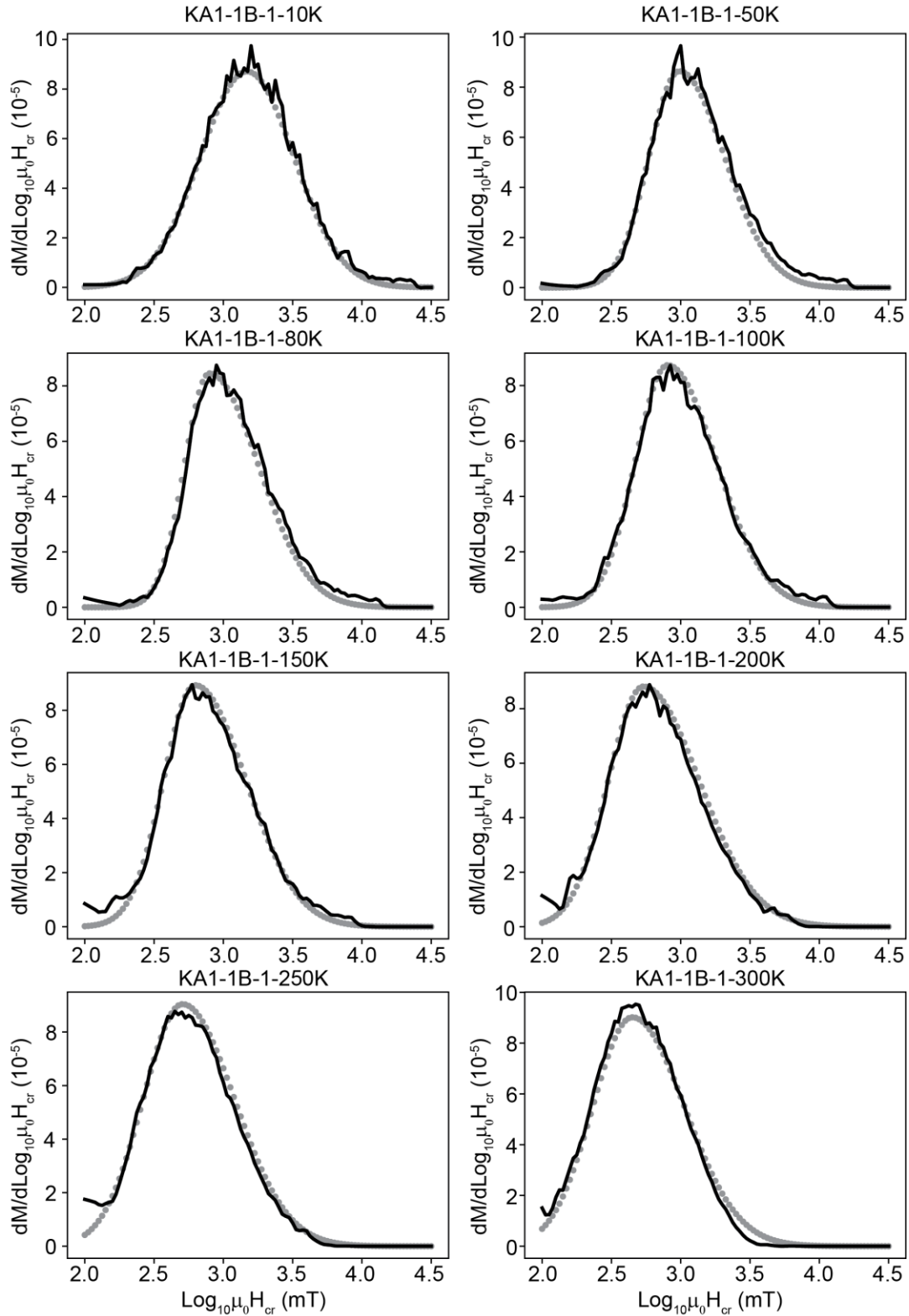
<sup>1</sup> hdi\_3% represents the lower bounds of the 97% high density interval of the corresponding posterior distribution.<sup>2</sup> hdi\_97% represents the upper bounds of the 97% high density interval of the corresponding posterior distribution<sup>3</sup> R\_hat is the Gelman-Rubin convergence statistic, which estimates the degree of convergence of a random Markov Chain. Values close to one indicate convergence to the underlying distribution.

733



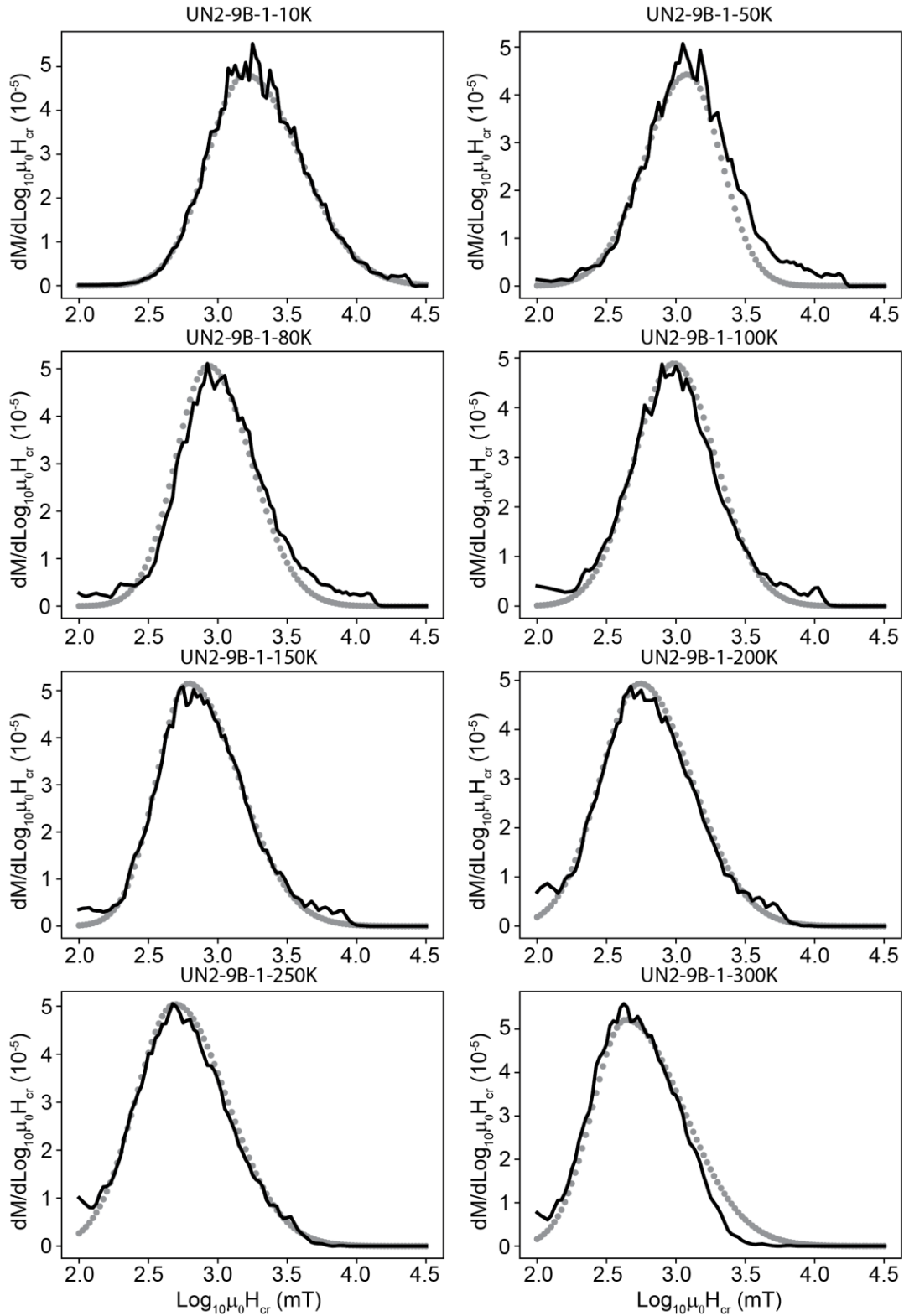
734

735 **Figure A1** The prior distribution (black lines) and posterior distribution (colored lines) of  
 736 parameters in the Bayesian model for (a-b) equation (3) and (c-e) equation (4). Blue, orange, green,  
 737 and red lines represent corresponding parameters for sample KA1-1B-1, UN2-9B-1, KA6-9B-1  
 738 and KA6-2L-B-1, respectively.



739

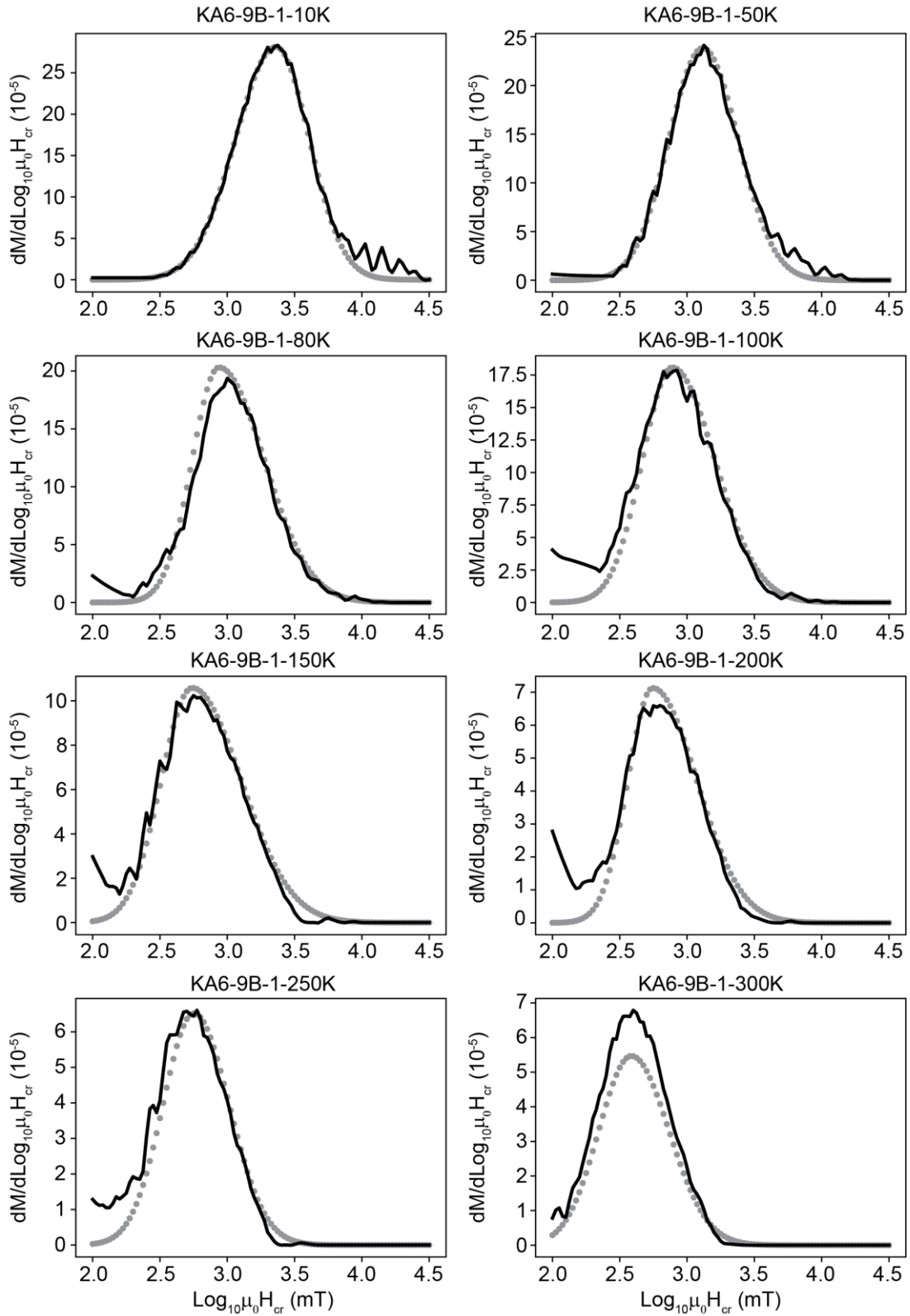
740 **Figure A2** Reconstructed (black solid lines) and measured backfield remanence curve derivatives  
 741 (gray dots) for Triassic sample KA1-1B-1.



742

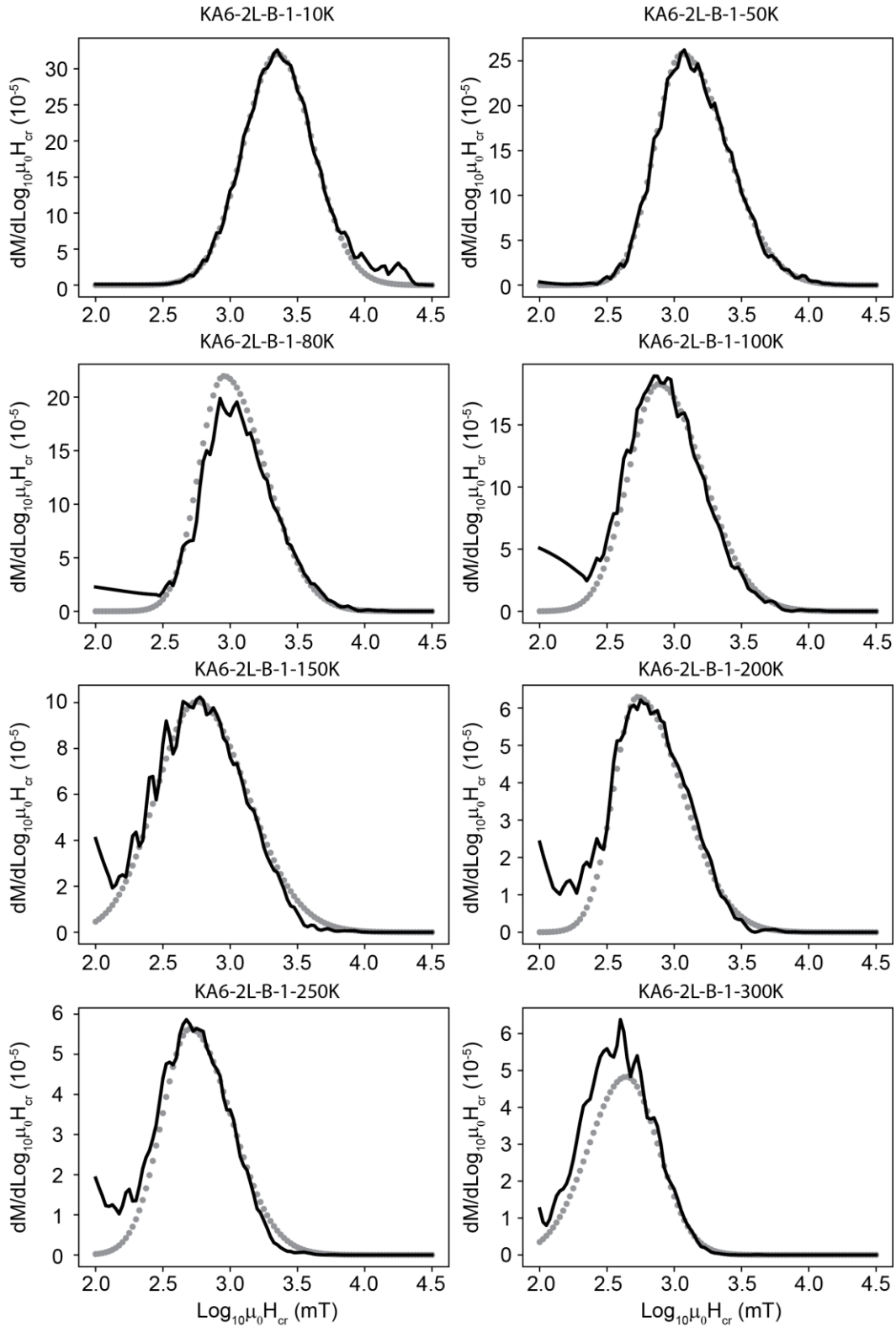
743 **Figure A3** Reconstructed (black solid lines) and measured backfield remanence curve derivatives

744 (gray dots) for Triassic sample UN2-9B-1.



745

746 **Figure A4** Reconstructed (black solid lines) and measured backfield remanence curve derivatives  
 747 (gray dots) for Jurassic sample KA6-9B-1.



748

749 **Figure A5** Reconstructed (black solid lines) and measured backfield remanence curve derivatives

750 (gray dots) for Jurassic sample KA6-2L-B-1.

751 **References**

- 752 Abrajvitch, A., R. S. Hori, & K. Kodama (2011), Magnetization carriers and remagnetization of bedded  
 753 chert, *Earth and Planetary Science Letters*, 305(1-2), 135-142.
- 754 Abrajvitch, A., R. S. Hori, & K. Kodama (2013), Rock magnetic record of the Triassic-Jurassic transition  
 755 in pelagic bedded chert of the Inuyama section, Japan, *Geology*, 41(7), 803-806.
- 756 Abrajvitch, A., B. J. Pillans, A. P. Roberts, & K. Kodama (2018), Magnetic properties and paleomagnetism  
 757 of zebra rock, western Australia: Chemical remanence acquisition in hematite pigment and ediacaran  
 758 geomagnetic field behavior, *Geochemistry Geophysics Geosystems*, 19(3), 732-748.
- 759 Banerjee, S. K. (1963), An attempt to observe basal plane anisotropy of hematite, *Philosophical Magazine*,  
 760 8(96), 2119-2120, doi:10.1080/14786436308209106.
- 761 Banerjee, S. K. (1971), New grain size limits for palaeomagnetic stability in haematite, *Nature-Physical  
 762 Science*, 232(27), 15-&, doi:10.1038/physci232015a0.
- 763 Beck, M. E., R. F. Burmester, & B. A. Housen (2003), The red bed controversy revisited: shape analysis of  
 764 Colorado Plateau units suggests long magnetization times, *Tectonophysics*, 362(1), 335-344,  
 765 doi:10.1016/S0040-1951(02)00644-3.
- 766 Bilardello, D., & K. P. Kodama (2010a), Palaeomagnetism and magnetic anisotropy of Carboniferous red  
 767 beds from the Maritime Provinces of Canada: evidence for shallow palaeomagnetic inclinations and  
 768 implications for North American apparent polar wander, *Geophysical Journal International*, 180(3),  
 769 1013-1029, doi:10.1111/j.1365-246X.2009.04457.x.
- 770 Bilardello, D., & K. P. Kodama (2010b), Rock magnetic evidence for inclination shallowing in the early  
 771 Carboniferous Deer Lake Group red beds of western Newfoundland, *Geophysical Journal International*,  
 772 181(1), 275-289, doi:10.1111/j.1365-246X.2010.04537.x.
- 773 Bloch, F. (1930), Zur Theorie des Ferromagnetismus, *Zeitschrift für Physik*, 61(3), 206-219,  
 774 doi:10.1007/BF01339661.
- 775 Bruzzone, C. L., & R. Ingalls (1983), Mossbauer-effect study of the morin transition and atomic positions  
 776 in hematite under pressure, *Physical Review B*, 28(5), 2430-2440, doi:10.1103/PhysRevB.28.2430.
- 777 Butler, R. (1992), *Paleomagnetism: Magnetic domains to geologic terranes*, Blackwell Scientific  
 778 Publications, Boston.
- 779 Collinson, D. W. (1969), Investigations into stable remanent magnetization of sediments, *Geophysical  
 780 Journal of the Royal Astronomical Society*, 18(2), 211-222, doi:10.1111/j.1365-246X.1969.tb03563.x.
- 781 Cornell, R. M., & U. Schwertmann (2004), *The Iron Oxides: Structure, Properties, Reactions, Occurrences  
 782 and Uses*, 664 pp., Wiley-VCH Verlag GmbH & Co. KGaA, doi:10.1002/3527602097.
- 783 Dekkers, M. J. (1990), Magnetic-properties of natural goethite. 3. Magnetic-behavior and properties of  
 784 minerals originating from goethite dehydration during thermal demagnetization, *Geophysical Journal  
 785 International*, 103(1), 233-250, doi:10.1111/j.1365-246X.1990.tb01765.x.
- 786 Dunlop, D. J. (1965), Grain distributions in rocks containing single domain grains, *Journal of  
 787 Geomagnetism and Geoelectricity*, 17(3-4), 459-&, doi:10.5636/jgg.17.459.
- 788 Dunlop, D. J., & Ö. Özdemir (2000), Effect of grain size and domain state on thermal demagnetization tails,  
 789 *Geophysical Research Letters*, 27(9), 1311-1314, doi: 10.1029/1999GL008461.
- 790 Dunlop, D. J., Ö. Özdemir, D. A. Clark, & P. W. Schmidt (2000), Time-temperature relations for the  
 791 remagnetization of pyrrhotite (Fe<sub>7</sub>S<sub>8</sub>) and their use in estimating paleotemperatures, *Earth and Planetary  
 792 Science Letters*, 176(1), 107-116, doi:10.1016/S0012-821X(99)00309-X.
- 793 Eglseder, M. S., A. R. Cruden, A. G. Tomkins, S. A. Wilson, & A. D. Langendam (2018), Colloidal origin  
 794 of microbands in banded iron formations, *Geochemical Perspectives Letters*, 6, 43-49,  
 795 doi:10.7185/geochemlet.1808.
- 796 Egli, R. (2021), Magnetic Characterization of Geologic Materials with First-Order Reversal Curves, in  
 797 *Magnetic Measurement Techniques for Materials Characterization*, edited by V. Franco and B. Dodrill,  
 798 pp. 455-604, Springer International Publishing, Cham, doi:10.1007/978-3-030-70443-8\_17.
- 799 Egli, R., A. P. Chen, M. Winklhofer, K. P. Kodama, & C.-S. Horng (2010), Detection of noninteracting  
 800 single domain particles using first-order reversal curve diagrams, *Geochemistry, Geophysics,  
 801 Geosystems*, 11(1), doi:10.1029/2009gc002916.

- 802 Frank, U., & N. R. Nowaczyk (2008), Mineral magnetic properties of artificial samples systematically  
 803 mixed from haematite and magnetite, *Geophysical Journal International*, *175*(2), 449-461.
- 804 Guyodo, Y., A. Mostrom, R. L. Penn, & S. K. Banerjee (2003), From nanodots to nanorods: oriented  
 805 aggregation and magnetic evolution of nanocrystalline goethite, *Geophysical Research Letters*, *30*(10),  
 806 doi:10.1029/2003gl017021.
- 807 Harrison, R. J., X. Zhao, P. Hu, T. Sato, D. Heslop, A. R. Muxworthy, H. Oda, V. S. C. Kuppili, & A. P.  
 808 Roberts (2019), Simulation of remanent, transient, and induced FORC diagrams for interacting particles  
 809 with uniaxial, cubic, and hexagonal anisotropy, *Journal of Geophysical Research: Solid Earth*, *124*(12),  
 810 12404-12429, doi:10.1029/2019JB018050.
- 811 Hendriksen, P. V., S. Linderoth, & P. A. Lindgard (1993), Finite-size modifications of the magnetic-  
 812 properties of clusters, *Physical Review B*, *48*(10), 7259-7273, doi:10.1103/PhysRevB.48.7259.
- 813 Hu, P. X., H. Oda, X. Zhao, R. J. Harrison, D. Heslop, T. Sato, A. R. Muxworthy, & A. P. Roberts (2021),  
 814 Assessment of magnetic techniques for understanding complex mixtures of magnetite and hematite: The  
 815 Inuyama red chert, *Journal of Geophysical Research-Solid Earth*, *126*(1), doi:10.1029/2020JB019518.
- 816 Huang, W., M. J. Jackson, M. J. Dekkers, P. Solheid, B. Zhang, Z. Guo, & L. Ding (2019), Nanogoethite  
 817 as a potential indicator of remagnetization in red beds, *Geophysical Research Letters*, *46*(22), 12841-  
 818 12850, doi:10.1029/2019GL084715.
- 819 Hyodo, M., T. Sano, M. Matsumoto, Y. Seto, B. Bradák, K. Suzuki, J.-i. Fukuda, M. Shi, & T. Yang (2020),  
 820 Nanosized authigenic magnetite and hematite particles in mature-paleosol phyllosilicates: New evidence  
 821 for a magnetic enhancement mechanism in loess sequences of China, *Journal of Geophysical Research:*  
 822 *Solid Earth*, *125*(3), e2019JB018705, doi:10.1029/2019JB018705.
- 823 Jackson, M., B. Carter-Stiglitz, R. Egli, & P. Solheid (2006), Characterizing the superparamagnetic grain  
 824 distribution  $f(V, H_k)$  by thermal fluctuation tomography, *Journal of Geophysical Research: Solid Earth*,  
 825 *111*(B12), doi:10.1029/2006jb004514.
- 826 Jacobsen, H. (2014), *Magnetic properties of nano-scale hematite: theory, experiments and simulations*,  
 827 University of Copenhagen.
- 828 Jiang, Z., Q. Liu, A. P. Roberts, M. J. Dekkers, V. Barrón, J. Torrent, & S. Li (2022), The magnetic and  
 829 color reflectance properties of hematite: from Earth to Mars, *Reviews of Geophysics*, *60*(1),  
 830 e2020RG000698, doi:10.1029/2020RG000698.
- 831 Jiang, Z. X., Q. S. Liu, M. J. Dekkers, V. Barron, J. Torrent, & A. P. Roberts (2016), Control of Earth-like  
 832 magnetic fields on the transformation of ferrihydrite to hematite and goethite, *Scientific Reports*, *6*,  
 833 doi:10.1038/srep30395.
- 834 Jiang, Z. X., Q. S. Liu, M. J. Dekkers, C. Colombo, Y. J. Yu, V. Barron, & J. Torrent (2014), Ferro and  
 835 antiferromagnetism of ultrafine-grained hematite, *Geochemistry Geophysics Geosystems*, *15*(6), 2699-  
 836 2712, doi:10.1002/2014gc005377.
- 837 Jiang, Z. X., Q. S. Liu, M. J. Dekkers, X. Zhao, A. P. Roberts, Z. Y. Yang, C. S. Jin, & J. X. Liu (2017),  
 838 Remagnetization mechanisms in Triassic red beds from South China, *Earth and Planetary Science*  
 839 *Letters*, *479*, 219-230.
- 840 Jones, D. L., & B. Murchey (1986), Geologic significance of paleozoic and mesozoic radiolarian chert,  
 841 *Annual Review of Earth and Planetary Sciences*, *14*, 455-492.
- 842 Kletetschka, G., & P. J. Wasilewski (2002), Grain size limit for SD hematite, *Physics of the Earth and*  
 843 *Planetary Interiors*, *129*(1), 173-179, doi: 10.1016/S0031-9201(01)00271-0.
- 844 Kneller, E. F., & F. E. Luborsky (1963), Particle size dependence of coercivity and remanence of single-  
 845 domain particles, *Journal of Applied Physics*, *34*(3), 656-658, doi:10.1063/1.1729324.
- 846 Lagroix, F., & Y. Guyodo (2017), A new tool for separating the magnetic mineralogy of complex mineral  
 847 assemblages from low temperature magnetic behavior, *Frontiers in Earth Science*, *5*(61),  
 848 doi:10.3389/feart.2017.00061.
- 849 Larrasoaña, J. C., A. P. Roberts, E. J. Rohling, M. Winklhofer, & R. Wehausen (2003), Three million years  
 850 of monsoon variability over the northern Sahara, *Climate Dynamics*, *21*(7), 689-698,  
 851 doi:10.1007/s00382-003-0355-z.

- 852 Lepre, C. J., & P. E. Olsen (2021), Hematite reconstruction of Late Triassic hydroclimate over the Colorado  
 853 Plateau, *Proceedings of the National Academy of Sciences*, 118(7), e2004343118,  
 854 doi:10.1073/pnas.2004343118.
- 855 Liu, Q., V. Barrón, J. Torrent, H. Qin, & Y. Yu (2010), The magnetism of micro-sized hematite explained,  
 856 *Physics of the Earth and Planetary Interiors*, 183(3), 387-397, doi:10.1016/j.pepi.2010.08.008.
- 857 Liu, Q. S., J. Bloemendal, J. Torrent, & C. L. Deng (2006), Contrasting behavior of hematite and goethite  
 858 within paleosol S5 of the Luochuan profile, Chinese Loess Plateau, *Geophysical Research Letters*,  
 859 33(20), doi:10.1029/2006gl027172.
- 860 Maaz, K., A. Mumtaz, S. K. Hasanain, & M. F. Bertino (2010), Temperature dependent coercivity and  
 861 magnetization of nickel ferrite nanoparticles, *Journal of Magnetism and Magnetic Materials*, 322(15),  
 862 2199-2202, doi:10.1016/j.jmmm.2010.02.010.
- 863 Martin-Hernandez, F., & S. Guerrero-Suárez (2012), Magnetic anisotropy of hematite natural crystals: high  
 864 field experiments, *International Journal of Earth Sciences*, 101(3), 637-647, doi:10.1007/s00531-011-  
 865 0665-z.
- 866 Martinez, B., A. Roig, X. Obradors, E. Molins, A. Rouanet, & C. Monty (1996), Magnetic properties of  
 867 gamma-Fe<sub>2</sub>O<sub>3</sub> nanoparticles obtained by vaporization condensation in a solar furnace, *Journal of*  
 868 *Applied Physics*, 79(5), 2580-2586, doi:10.1063/1.361125.
- 869 Matsuo, M., K. Kubo, & Y. Isozaki (2003), Moessbauer spectroscopic study on characterization of iron in  
 870 the Permian to Triassic deep-sea chert from Japan, *Hyperfine Interactions*, 5, 435-438.
- 871 Maxbauer, D. P., J. M. Feinberg, & D. L. Fox (2016), MAX UnMix: A web application for unmixing  
 872 magnetic coercivity distributions, *Computers & Geosciences*, 95, 140-145, doi:  
 873 10.1016/j.cageo.2016.07.009.
- 874 Menyeh, A., & W. O'Reilly (1995), The coercive force of fine particles of monoclinic pyrrhotite (Fe<sub>7</sub>S<sub>8</sub>)  
 875 studied at elevated temperature, *Physics of the Earth and Planetary Interiors*, 89(1), 51-62, doi:  
 876 10.1016/0031-9201(94)02999-R.
- 877 Muench, G. J., S. Aarj, & E. Matijevic (1985), The Morin transition in small Alpha-Fe<sub>2</sub>O<sub>3</sub> particles,  
 878 *Physica Status Solidi a-Applied Research*, 92(1), 187-192, doi:DOI 10.1002/pssa.2210920117.
- 879 Néel, L. (1949), Théorie du traînage magnétique des ferromagnétiques en grains fins avec application aux  
 880 terres cuites, *Annales de Geophysique*, 5, 99--136.
- 881 Oda, H., & H. Suzuki (2000), Paleomagnetism of Triassic and Jurassic red bedded chert of the Inuyama  
 882 area, central Japan, *Journal of Geophysical Research-Solid Earth*, 105(B11), 25743-25767.
- 883 Özdemir, O., & D. J. Dunlop (2014), Hysteresis and coercivity of hematite, *Journal of Geophysical*  
 884 *Research-Solid Earth*, 119(4), 2582-2594, doi:10.1002/2013jb010739.
- 885 Özdemir, Ö., & D. J. Dunlop (2002), Thermoremanence and stable memory of single-domain hematites,  
 886 *Geophysical Research Letters*, 29(18), 24-21-24-24, doi: 10.1029/2002GL015597.
- 887 Peters, C., & M. J. Dekkers (2003), Selected room temperature magnetic parameters as a function of  
 888 mineralogy, concentration and grain size, *Physics and Chemistry of the Earth, Parts A/B/C*, 28(16), 659-  
 889 667, doi:10.1016/S1474-7065(03)00120-7.
- 890 Roberts, A. P., X. Zhao, D. Heslop, A. Abrajevitch, Y.H. Chen, P. Hu, Z. Jiang, Q. Liu, & B. J. Pillans  
 891 (2020), Hematite ( $\alpha$ -Fe<sub>2</sub>O<sub>3</sub>) quantification in sedimentary magnetism: limitations of existing proxies  
 892 and ways forward, *Geoscience Letters*, 7(1), 8, doi:10.1186/s40562-020-00157-5.
- 893 Roberts, A. P., X. Zhao, P. Hu, A. Abrajevitch, Y. Chen, R. Harrison, D. Heslop, Z. Jiang, J. Li, Q. Liu, A.  
 894 R. Muxworthy, H. Oda, H. St. C. O'Neill, B. J. Pillans & T. Sato (2021), Magnetic domain state and  
 895 anisotropy in hematite ( $\alpha$ -Fe<sub>2</sub>O<sub>3</sub>) from first-order reversal curve diagrams, *Journal of Geophysical*  
 896 *Research: Solid Earth*, 126(12), e2021JB023027, doi:10.1029/2021JB023027.
- 897 Salvatier, J., T. V. Wiecki, & C. Fonnesbeck (2016), Probabilistic programming in Python using PyMC3,  
 898 *PeerJ Computer Science*, doi:ARTNe5510.7717/peerj-cs.55.
- 899 Satheesh, M., A. R. Paloly, C. K. Krishna Sagar, K. G. Suresh, & M. J. Bushiri (2018), Improved coercivity  
 900 of solvothermally grown hematite ( $\alpha$ -Fe<sub>2</sub>O<sub>3</sub>) and hematite/graphene oxide nanocomposites ( $\alpha$ -Fe<sub>2</sub>O<sub>3</sub>/GO)  
 901 at low temperature, *physica status solidi (a)*, 215(2), 1700705, doi:10.1002/pssa.201700705.

- 902 Schwertmann, U. (1991), Solubility and dissolution of iron-oxides, *Plant and Soil*, 130(1-2), 1-25, doi:  
903 10.1007/Bf00011851.
- 904 Shibuya, H., & S. Sasajima (1986), Paleomagnetism of red cherts - a case-study in the Inuyama area, central  
905 Japan, *Journal of Geophysical Research-Solid Earth and Planets*, 91(B14), 14105-14116.
- 906 Stoner, E. C., & E. P. Wohlfarth (1948), A mechanism of magnetic hysteresis in heterogeneous alloys,  
907 Philosophical Transactions of the Royal Society of London. Series A, *Mathematical and Physical*  
908 *Sciences*, 240(826), 599-642, doi:10.1098/rsta.1948.0007.
- 909 Sun, S., K. O. Konhauser, A. Kappler, & Y.L. Li (2015), Primary hematite in Neoproterozoic to  
910 Paleoproterozoic oceans, *GSA Bulletin*, 127(5-6), 850-861, doi:10.1130/b31122.1.
- 911 Sunagawa, I. (1960), Growth history of hematite, *American Mineralogist*, 45(5-6), 566-575.
- 912 Sunagawa, I., & P. J. Flanders (1965), Structural and magnetic studies in hematite single crystals,  
913 *Philosophical Magazine*, 11(112), 747-&, doi:10.1080/14786436508230080.
- 914 Swanson-Hysell, N. L., L. M. Fairchild, & S. P. Slotznick (2019), Primary and secondary red bed  
915 magnetization constrained by fluvial intraclasts, *Journal of Geophysical Research: Solid Earth*, 124(5),  
916 4276-4289, doi:10.1029/2018jb017067.
- 917 Swanson-Hysell, N. L., J. M. Feinberg, T. S. Berquo, & A. C. Maloof (2011), Self-reversed magnetization  
918 held by martite in basalt flows from the 1.1-billion-year-old Keweenawan rift, Canada, *Earth and*  
919 *Planetary Science Letters*, 305(1-2), 171-184.
- 920 Tauxe, L., D. V. Kent, & N. D. Opdyke (1980), Magnetic components contributing to the NRM of middle  
921 Siwalik red beds, *Earth and Planetary Science Letters*, 47(2), 279-284, doi:10.1016/0012-  
922 821x(80)90044-8.
- 923 Van Der Voo, R., & T. H. Torsvik (2012), The history of remagnetization of sedimentary rocks: Deceptions,  
924 developments and discoveries, *371(1)*, 23-53.
- 925 Zhang, D. J., K. J. Klabunde, C. M. Sorensen, & G. C. Hadjipanayis (1998), Magnetization temperature  
926 dependence in iron nanoparticles, *Physical Review B*, 58(21), 14167-14170,  
927 doi:10.1103/PhysRevB.58.14167.

928